Altering the properties of graphene on Cu(111) by alkali halides

Inauguraldissertation

zur

Erlangung der Würde eines Doktors der Philosophie

vorgelegt der

Philosophisch-Naturwissenschaftlichen Fakultät

der Universität Basel

von

Mathias Schulzendorf

aus Deutschland

Basel, 2019

Genehmigt von der Philosophisch-Naturwissenschaftlichen Fakultät
auf Antrag von:

Prof. Dr. Ernst Meyer
Prof. Dr. Martino Poggio

Basel, den 20.06.2017

Prof. Dr. Martin Spiess, Dekan

Abstract

Defect free, monocrystalline graphene can be obtained by catalytic growth on transition metal surfaces like Cu(111). [1] On the one hand this bottom-up approach provides a clean and controllable route. On the other hand, graphene's remarkable properties are deminished by the binding to the transition metal substrate. [2]
Intercalation opens new horizons to tailor the properties of absorbed graphene as desired. By engineering the graphene-metal interface, either free-standing or doped graphene can be obtained. [3] In addition, new properties like magnetism can be introduced by intercalation. [4] Understanding and controlling the process of intercalation is crucial.
Strain may plays an important role on the intercalation. On coalescence of graphene and alkali halide islands, grain boundaries were formed. The formation can be opposed by a compressive intrinsic strains that already existed in a thin-film prior the coalescence. [5] The Moire is a manifestation of the intrinsic compressive strain in graphene. [6] Alkali halides provide an ideal toolbox to test this hypothesis. For NaCl the strain is tensile, while in KBr it is compressive. In addition higher adatom mobility, induced by heating, can deepen compressive strains. [5]
The intrinsic properties of KBr and graphene opposed the formation of grain boundaries, promoting further epitaxial growth. In contrast NaCl should have favoured the formation of grain boundaries.
The effect of alkali halides on graphene investigated by Dynamic Force Microscopy (DFM) and Kelvin Probe Force Microscopy (KPFM) will be presented in chapter 3. Indeed, smooth interfaces were found for KBr co-adsorption. For NaCl the grain boundaries were grown over the graphene edges.
For the first time the work function of graphene on Cu(111) was measured by KPFM and in perfect agreement to the value predicted by theory. Both alkali halides were found to induce changes in work function of graphene. While only a negligible shift was found for NaCl, graphene's work-function became comparable to free-standing graphene in presence of KBr.
A simple plate capacitor model for the interface of graphene on copper [7] was applied to calculate the expected contact potential difference. Very good agreement between the model and the measured CPD was found in the cases of graphene on copper and KBr-intercalated graphene.
In cooperation with the group of Prof. Clelia Rhigi it was proven by means of DFT, that intercalation by KBr was favorable over the absorption of KBr on copper. The first results also revealed a cooperative effect between the surface

and the islands of KBr and graphene.
These observations were complemented by spectroscopic measurements on the Moire structures of graphene on Cu(111) and of graphene intercalated by a monolayer of KBr.

Contents

Abbreviations

Abbreviation	Meaning
AFM	Atomic force microscopy
CPD	Contact potential difference
CVD	Chemical vapor deposition
DFM	Dynamic force microscopy
DFS	Dynamic force spectroscopy
DFT	Density functional theory
FFM	Friction force microscopy
FM-AFM	Frequency modulated atomic force microscopy
LCPD	Local contact potential difference
KPFM	Kelvin Probe Force Microscopy
MD	Molecular dynamics
nc-AFM	Non contact atomic force microscopy
RT	room temperature
SPM	Scanning probe microscopy
STM	Scanning tunneling microscopy
UHV	Ultra-high vacuum
VdW	Van der Waals

Table 1: Abbreviations

Chapter 1

Introduction and theory

In an ideally flat 2D configuration, graphene has well defined phononic and electronic properties. The interaction with an underlying substrate will force graphene to extend into the third dimension, modifying these properties. On transition metals, this becomes observable as Moiré structures, that reflect the strength of the interaction with the substrate. But what will happen on modifying the substrate, like intercalating atoms? One would expect a change in graphene's interaction with the substrate, that is reflected in a different Moiré becoming observable.
In the first part of this chapter fundamental physical concepts used in the context of this work will be reviewed. Followed by a part giving an overview on the interplay of strain and electronic properties for graphene absorbed on transition metals and highlight its implications for the experiments presented in this work. Closing with a hypothesis on the intercalation of alkali halides for graphene on Cu(111).

1.1 Fundamental concepts

1.1.1 Electrostatic forces and the work function

The Coulomb force is one of the most fundamental physical forces. Based on fundamental electrostatic interactions, the concept of the work function will be presented in this section. It is not only important for understanding the graphene metal interface, but also for the measurement methods STM and nc-AFM, especially in KPFM.

Work function

The work function is a macroscopic concept describing the thermodynamic work necessary to remove an electron from within a metal into the vacuum. Within the concept of the work function the surface is considered as an infinite, homogeneous plane. The second implication -electronic changes on surface creation- is of utmost importance for the work function. Negative charge can leak out of the surface plane, leading to a reduction in energy. The resulting excess positive charge below the surface leads to the formation of a surface dipole. [8]
Now when an electron should be removed from the bulk to infinity it has to pass this surface dipole. This causes a change in the potential energy of the electron when it is traveling through the dipole, as the electrons energy is lower by $\Delta\phi$ for being in proximity of the positive plate. The thickness and thus the decay length for the dipole is short within the range of a few Å. In addition, upon removal of an electron an image charge is created in the crystal. The Coulomb interaction between the two charges results in an attractive potential, also referred to as the image potential. This local potential modulation can be detected by a sensing probe when it is within the decay length of the image charge potential close to the surface.

$$\Phi = E_V - E_F = \phi - \bar{\mu} = \Delta\phi(z) - \bar{\mu} \tag{1.1}$$

$E_V = \phi(z = \infty)$ and $\phi(z)$ being the change in electrostatic potential energy and $\bar{\mu}$ the chemical potential. However, this ideal concept is limited to ideal surface plane. Any modulations of this ideal structure, like terraces, dopants, chemical variations. adatoms or islands, lead to a modulation of the charge density in the surface plane (xy). To take these modulations into account, the concept of a local work function has been developed: [9]

$$\Phi_{local} = E_V - E_F = \Delta\phi(x, y, z) - \bar{\mu} \tag{1.2}$$

The local work function reflects the local variation of the potential energy, differing from the original concept as $z \neq \infty$. [9]

Plate capacitor model of the graphene-metal interface

In section 1.1.1 the importance of the workfunction on the absorbtion of graphene on a transition metal has been described. The work function difference of the two isolated materials is accomodated by a transfer of charge,

leading to the formation of an interface dipole. By applying a simple plate capictor model for this interface, the Fermi level shift in graphene can be calculated, based on the work funtions of the two isolated materials. [7]
By assuming a quasi infinite homogenous surface plane for graphene on copper, a classical plate capacitor model can be applied to calculate the interface dipole of Gr/Cu(111). [7, 10] The concept of the plate capacitor will become also important in KPFM, cf. to 2.1.3. The Energy of a plate capacitor is:

$$U_{el} = \frac{1}{2}CV^2 \tag{1.3}$$

An important term for the calculation of the Fermi level shift in the work of Khomyakov *et al.* is α, that has the units of an electrostatic force ($F = q * E$). Thus we will refer to it as α_F:

$$\alpha_F = \frac{e^2}{\epsilon_0 A}\left[\frac{eV}{\mathring{A}}\right] \tag{1.4}$$

This parameter is inverse proportional to the dielectric properties of the interface and employed to calculate the work function of the absorbed graphene:

$$\Delta E_F = \pm\frac{\sqrt{1 + 2\alpha D_0(d - d_0)|W_M - W_G - \Delta_c|} - 1}{\alpha D_0(d - d_0)} \tag{1.5}$$

In addition to the dependence on the materials work functions, the model requires parameters for an ab-initio calculated short range interaction $\Delta_c|$, the distance of the charge sheets of the dipole within the interface $(d - d_0)$ and the charge within graphene's unit cell (D_0).
The intercalation of an alkali halide then can be considered as the insertion of a dielectric into the plate capacitor. The change in the electric field of the interface is then expressed by modifying the α_F parameter from equation 1.4, taking the inserted dielectric into account by employing the relative permittivity:

$$\alpha_{F_r} = \frac{e^2}{\epsilon_0 \epsilon_\mathbf{r} A}\left[\frac{eV}{\mathring{A}}\right] \tag{1.6}$$

In case of graphene on copper, the interface is the vacuum, and ϵ_r is equal to unity satisfying equation 1.4. By inserting the modified parameter into equation 1.5, a change in the Fermi level of graphene can be expected.
The relative permittivity is normally referred to macroscopic bulk materials. In the case of approaching the ultimate limit of thin films, a decrease of the effective permitivity has been found and can be calculated by a summation over i dipole layers: [11]

$$\epsilon_{eff} = \left[1 - \frac{4\pi}{n}\sum_{i=1}^{n}\alpha(i)\tilde{E}_{loc}(i)\right]^{-1} \tag{1.7}$$

As the alkali halide is located in between graphene and copper we will assume that $\epsilon_r = \epsilon_{eff}$ and a monolayer of salt is intercalated. This simplifies equation

1.7 by i becoming one. $\tilde{E}_{loc}(i)$ is the local electric field of the dipole that can be derived from the electric of the graphene-copper capacitor. [11] An additional step has to be included to account for the local field of a graphene unit cell. Per unit cell graphene $A_{gr}/(2*a)^2$ dipole moments are found. The local field for the graphene-copper interface then can be defined as:

$$E_{loc} = E + \frac{\mu}{4\pi\epsilon_0 a^3 \alpha(i)} \tag{1.8}$$

With the dimensionless α being the atomic polarizability within this equation and the thin-film is considered as $i = 1$ layers within the capacitor. As a last step the local electric field $\tilde{E}_{loc}(i)$ at the dipole is defined as:

$$\tilde{E}_{loc}(i) = E_{loc}\frac{Q}{\epsilon_0} \tag{1.9}$$

In chapter 3 the model to treat the interface as a plate capacitor will be applied to calculate model values for the work function change upon the intercalation of alkali halides, by assuming a monolayer of the salt as a dielectric within the interface dipole field. These model value then can be compared against measured values from KPMF experiments and give an indication on a successful intercalation of the salt. While no intercaltion should leave the interface dipole unchanged, clear changes within the electric field of the interface dipole can be expected by the intercallant, effectively changing the work function. [11]

1.1.2 Dissipative processes - non-contact friction

Dissipative processes can arise by non-contact friction processes. The Van der Waals interaction between two resting bodies mediates radiative heat transfer. The thermal and quantum fluctuations in the current density of one body induce a current density in the other, giving rise to Van der Waals interaction. If these are in relative motion, the fluctuating electromagnetic field will give rise to Van der Waals friction. The relative motion induces a current, that lags behind motion, giving rise to Van der Waals friction. At small distances resonant photon tunneling between tip and sample may increase VdW friction by several orders of magnitude. In addition, a reduction in volume for dissipative processes like in 2D materials futrher increases friction. This is also depending on the dielectric properties of the substrate. [12] Intercalation may lead to a change in friction, as a change in the dielectric properties of the interface is expected, see section 1.1.1.
The oscillating stress by the oscillating tip deforming an elastic surface excites acoustic waves, resulting in non-contact friction by phonon interactions. [12] The perpendicular oscillation is exerting astress onto the surface, exciting acoustic phonon modes. [12] In graphene the predominant acoustic modes are flexural modes, [13] as described in section , leading to the expectation of observable non-contact friction processes.
Measuring this frictional processes requires a higher sensitivity than measuring parallel to the surface. The friction by an orthogonal oscillating tip can

be expressed as $\Gamma_\perp$: [12]

$$\Gamma_\perp = \frac{\xi_\perp K^2}{4\pi\rho c_t^3} \tag{1.10}$$

Where $K^2 = \frac{\partial F}{\partial d}$. For a spherical tip K yields:

$$K = \frac{R\hbar\omega_p}{16\sqrt{2}d^3} \tag{1.11}$$

The result is $\Gamma_\perp \propto d_{-6}$ in the case of phonic friction. For a standard silicium cantilever (PPP), oscillated at its 2nd resonance frequency of $f_0 = 986.056kHz$, with a force constant of $k = 5.779kN/m^2$ and a Q-factor of 14'517, the internal non-contact friction is:

$$\Gamma_0 = \frac{k}{2\pi f_0 Q} = 6.448 \times 10^{-8}\frac{kg}{s} \tag{1.12}$$

1.1.3 Surface strain

The physical origin of strain within a surface is directly related to the changes in the charge density and the binding character for the surface atoms. On creation of the surface the coordination of the atoms within the surface layer is changed and the charge density is redistributed. The atoms within the surface layer become either compressive or tensile strained. In case of tensile strain (negative sign) the surface tends to shrink, lowering the surface energy. For compressive strain (positve sign), the surface has the tendency to expand. This ultimately changes the nature of the chemical bonds and alters the inter atomic distances in response to the applied surface stress. [14]
The potential energy stored by the system upon deformation from its equilibrium configuration is also referred to as strain energy. In case of elastic deformations the deformation obeys Hooke's law. A relief, e.g. by rearrangement releases the stored energy, capable to perform mechanic work. [14]
A well studied example is the silicon surface. There the bond angles of the surface atoms are altered, and the sp^3-hybridised bonds are rehybridized to sp^2, resulting in a shortening of the bond length. This results in a compressive stress (negative sign), that becomes even more compressive when Si surface atoms are replaced with larger atoms. In contrast, the substitution by smaller atoms yields tensile (positive sign) stress. [14]
The following sections will give breadth overview on strain for Cu(111), absorbed graphene and the formation of islands on a surface.

Surface strain in transition metals

In transition and noble metals no directional bonding is present. [14] The force acting on the surface atoms decreases the interlayer spacing. Within the surface and second layer plane charge is slightly depleted compared to the bulk. While the charge density between the surface atoms is increased, these do not contribute to forces for symmetrical reasons. [15] In case of some metals, this first layer tends to contract to increase the atomic density, resulting in

surface reconstructions. [14, 15] The herringbone superstructure of Au(111) is a well-known example of reconstruction caused by surface stresses. [14, 16] If no reconstruction takes place, as is the case for Cu(111) [16] or Ir(111), [17] the unreconstructed surface is contracted and the surface stress becomes tensile. [14, 15]
DFT calculations confirmed tensile stress for (111) faceted metal surfaces. The atoms of the first layer preferred a denser packing owing to the potential of the second layer (reflecting the bulk periodicity). While this leads to a compressive reconstruction in many close-packed metals, Cu(111) is not reconstructed. The tensile stress is relatively small and relaxation is achieved by inward movement of the first three layers. [16]

1.1.4 Graphene growth by chemical vapor deposition

Epitaxial graphene can be prepared on Cu(111) by dosing ethylene as a precurser onto the surface while at repeated high temperature cycles.. [1] It was found that the binding of the edge to the catalyst is the dominating factor for the orientation upon growth, constraining small islands along specific directions. The adhesion energy of graphene becomes dominant over the edge binding energy for islands larger than a critical size of about $10'000$ atoms. With increasing island size, the number of edge atoms and the barrier to rotate the membrane becomes too large to be overcome the thermal activation. [18] This pinning of the island orientation is consistent with observation of the impingement of alkali halide islands. [5]
The limitation of the rotational degrees of freedom gives an explanation for the experimentally observable topograpies of graphene on Cu(111). [1, 18] Nascent islands grown on the same terraces show few equivalent orientations determined by the edge catalyst interaction. [18] The process of epitaxial graphene growth on Cu(111) is driven by continuous hydrocarbon adsorption. [19] The suppression of nucleation or the presence of seeds reduces the amount of islands and large domains will be formed, leading to a continuous epitaxial like growth. [18]

1.2 Free-standing graphene - fundamental properties

We will first highlight the basic properties of graphene in its ideal, flat configuration. Many of graphene's remarkable physical properties arise from the structural arrangement of the carbon atoms within it's two-dimensional framework, defined by the triangular basis of the hexagonal lattice with its two sub-lattices. [13]
By hybridization of an s- with two p-orbitals, sp^2 hybridized σ-bonds between nearest neighbored carbon atoms are formed, with an equilibrium distance of 0.142 nm. The formation of deep σ-valence bands, that are half filled in regards to the Pauli principle, make graphene a robust allotrope of carbon and

characterize the soft trigonal planar structure of graphene. [13]
Being orthogonal to this planar structure, the p-orbitals in flat graphene are unaffected by the σ-bonding. The overlap of neighboring p-orbitals leads to the formation of half filled π-bands giving rise to its electronic properties.
A common approach to describe graphene's electronic structure is the tight-binding model, where electrons can hop to nearest (different sub-lattice) and next-nearest neighbor (same sub-lattice) sites. The dispersion is symmetric around zero energy in case of next-nearest hoping being zero. [13]
The energy around the Dirac point is related to the electrons momentum relative to the conical point and the Fermi velocity. In contrast to an ordinary electron gas, the velocity is independent of the energy of the momentum. [13]
For low energy excitation's the dispersion of the electrons within these bands can be considered as linear. The cones formed by the dispersion are distinguishable by their origin from the different triangular sub-lattices and are referenced as K- and Ḱ-points. These are also referred to as Dirac cones or points, that are located at the corners of the 1st Brillouin zone. As long as these do not differ, their state is considered as valley degenerate. [20] Within the regime of low energy excitation's, the dispersed electrons behave as massless, chiral Dirac fermions with their chemical potential crossing the conical point. For free graphene, the Fermi level is aligned with these points, making it a gap-less semiconductor and giving rise to its remarkable physical properties. [13]

1.3 Absorbed graphene - effects of rippling and Moiré structures

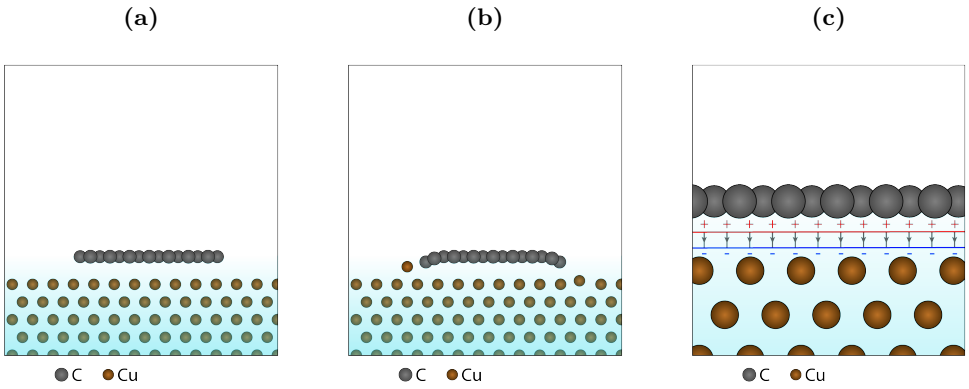

Figure 1.1: Sketch of graphene on the copper surface. The flake can be bound be edge atoms. Charge transfer leads to an interface dipole that can be considered as a plate capacitor.

1.3.1 Electronic changes upon absorption - neglecting strain

Two different classes for the binding of graphene to the substrate can be defined, determined by the binding energy and the equilibrium separation. [7, 21]
In case of weaker interactions, found for the metals Al, Cu, Ag, Au and Pt, the typical dispersion relation for graphene, especially at the conical point, can be clearly identified. The weak absorption for this class of metals is called physisorption. Graphene on Cu(111) is clearly identifiable as a weakly interacting system, with a distance between graphene and the Cu(111)-surface around 330 pm dependent on the orientation angle. [7, 18, 21]
Upon absorbtion, the different work functions of graphene and the absorbing metal have to be equilibrated. The result is a charge transfer, causing the formation of a dipole layer at the interface and a step in the electrostatic potential. The charge was found to be directly at the interface, having a simple dipolar distribution in all cases of physisorbed graphene, despite Alumina. [7]
The charge transfer causes a shift in the Fermi level of graphene. In case the donation of electrons (holes) from the metal to graphene the Fermi level is shifted upwards (downwards) in respect to graphene's conical point. Graphene becomes n-(p-)type doped in this process.[1]
For physisorbed graphene two different classes can be defined, p-type doped graphene in the cases of Al, Ag and Cu. n-type doped for Au and Pt. Pt charge transfer from the metal towards graphene was found, [22] shifting the Fermi level upwards in respect to conical point, the opposite than on copper. [7]
The density of states around the the Fermi level is much smaller for graphene when compared to the transition metal. To equilibrate the Fermi level upon charge transfer a shifts in graphene of the level is occurring on graphene's side. In case of physisorbed graphene this shift can be modeled by simply relating the difference of the work functions of the metal on which graphene absorbed and those of free-standing graphene. This simple model was found to be very accurate, deviating by around 80 meV to DFT result. [7]
The charge per carbon atom in relation to the dipole, was found to be relatively small. Despite the small amount of charge, the resulting shift in the work function can be quite strong.[2] The localization of the charge was found in the center of the interface, with the two "charge sheets" being less separated than the equilibrium separation of graphene and the metal. [7, 21]
By increasing the separation, the cross-over point for doping is as expected at the equality point of the work functions of metal and free-standing graphene. This is taken as a clear indicator, that at equilibrium separations, that not only a dipole layer is formed, but also a direct interaction between graphene and the metal must have taken place. It is supposed that this is due to repulsive interaction be a wave-function overlap between substrate and absorbent, like for molecules on metal surfaces. [7,21] This is another indication that Martinez *et al.* were right and there are pinning-points where orbitals are rehybridized. [22]

[1] The shift in the Fermi level is -170 meV for Cu(111) and 330 meV for Pt(111). [7]
[2] Transferred charge is 0.008 times the charge of an electron in case of Cu and 0.011 in case of Pt. [7]

A phenomenological model has been derived to treat the interface as a simple plate capacitor, that is discussed in detail in 1.1.1. It is valid where the DOS are linear meaning a Fermi level within $\pm 1eV$ from the conical point, also in case of a band gap opening. [7, 21]

1.3.2 Absorption and strain - formation of Moirè structures

Any disturbance of graphene's perfectly flat structure induces disorder, that has not been accounted for in the previous section. Disorder is induced by time-averaged fluctuations from thermal activation and becomes pinned under the influence of a scaffolding structure, when graphene is suspended on substrate. Then the structural fluctuations are not time dependent any more, and form a quenched disorder. [13]
In addition, any disorder in the substrate will induce further disorder in graphene. This can be considered as a minimization of elastic energy and a tendency for graphene to follow the sample's corrugation. [13, 23]
On Cu(111) a biaxial, compressive strain is present, [24] that is sufficient to overcome the Van der Waals interaction between graphene and the substrate, leading to an out of plane buckling making the strain nonuniform. [23, 24] The elastic strain energy, with contributions from in-plane compression and bending, is reduced. [23]
Structures with the lowest mismatch and consequently lowest strain, were observed more frequent. Positive (tensile) and negative (compressive) mismatches were found straining the layer to extend or to compress the carbon bond length, leading to out of plain configurations, that manifests as Moiré pattern. [23–25]
Molecular dynamics (MD) simulations showed that the compression is present over the whole sheet for graphene on Cu(111) by shortening of the bond lengths on hill and even stronger shortening on the valleys sites. This was also found to be visible as bright and dark areas in STM. Tensile and compressive strains are reflected by expansion and shortening of the bonds. The lattice mismatch and the resulting superstructures were found to be very sensitive to the variations in the bond length. [24]
Also by nc-AFM, a different strength in the stiffness between the carbon atoms at low and high sites of the Moiré structure of graphene has been measured, depending on the local interaction strength of the carbon atoms with the substrate. [26]
While an increased corrugation reduces in-plane compression, bending and Van der Waals interactions between graphene and substrate are increased. For nanoribbons it is expected that the effects of Van der Waals, elastic strain energy and edge effects would determine the equilibrium morphology. [23] We will expect the same to hold valid for Islands.
On a corrugated substrate, a flat morphology is favoured for small substrate corrugation wavelengths, in contrast to a conformal morphology for long wavelengths. The transition between the two extremes is abrupt. [23]
The morphology of graphene is always more flat than those of the substrate with longer corrugation wavelengths, where the adhesion energy is dependent on the substrates corrugation. Larger wavelengths of substrate corrugation

reduce adhesion, and lead to larger separations. [23]
The mean separation and the corrugation amplitude depend on the mismatch strain. Tensile strains flattens, while compressive strains increase corrugation amplitudes. Even on a perfectly flat substrate a critical mismatch strain results in a corrugation. The effect of strain is coupled to the effect of substrate surface corrugation, promoting the strain instability under compressive conditions. [23]
Graphene is accommodated by the system by favouring the smallest strain configuration. Main interaction comes from the coincident positions of both lattices, [22, 25], being consistent with the observation of an otherwise weak interaction. [7, 18, 27]
Low temperature annealing and the type of precursor gas may led to formation of other phases, not present from high temperature preparations. Tensile strained structures, measurable as Moirè should only be correlated to electronic effects. Nevertheless other processes may lead to topographic Moirè in tensile structures. [25] The compressive strain for graphene on Cu(111) leads to the expectation, that Moiré structures for should be observable as topographic and electronic structures.
Some structures were favoured by minimizing strain. The observation of less favourable structures with higher mismatches was attributed by release of the strain within the periodicity of the Moirè by the local interaction at the points defining the mismatch, analogue to chemisorbed graphene on Ru. Strain minimization mediates the stability of Moiré structures. [25]

How the Moirè affects the electronic properties

Corrugations generate an inhomogeneous electrochemical potential in graphene. The bending of graphene directly affects its morphology and electronic structure. Initially, the inter-atomic distances are decreased, leading to an increasing overlap of p_z-orbitals. This process is more energy costly (spring constant of graphene $57eV/\mathring{A}^2$) than the rotation of p_z-orbitals, inducing their rotation. The effect of this rotation is the coupling and rehybridization between graphene's π- and σ-orbitals. [13, 28]
As a consequence the charge neutrality point at the Fermi energy will be off-set with local electron (hole) doping in flatter (bumpier) regions. The spatially varied charge density enhances rippling by renormalizing the bending rigidity. This variation of the electrochemical potential in return enhances the rippling tendency by the increasing charge inhomogeneity. [28]
A local change in the single site energy, like the formation of point contacts described in 1.3.4, can act as a chemical potential shift at the Dirac point. The LDOS close to the impurity are affected by an electron-hole asymmetry generated by the Coulomb potential. This density decays fast from the site depending on $1/r^3$, in addition to fast oscillations in the order of the lattice spacing if the coupling constant reaches not a critical limit. [13]
This effect can be strongly suppressed by large effective dielectric constants, e.g. nanometer thin layers of absorbed water. Any changes in the distances or angles between the p_z-orbitals will modify the hopping energies. [13]

This gives an interesting take on local charge transfer at pinning-points of graphene Moiré physisorbed on a transition metal. [22] The Moiré induces a smooth and well ordered disorder in graphene an the pinning points can be considered as a charge impurity. First, the local changes will not be confined to the pinning-points. This is consistent with the self-doping mechanism. [13] Second, charge carriers will not directly be affected by the potential barrier generated by the interaction. [29]

Strain at the edges of graphene

By boundary conditions graphene has different electronic properties at its edges. [13, 30] Zigzag edges sustain surface states, while resonances are absent in armchair edges. By coupling to conducting leads, these boundary conditions strongly affect the conductance and the chiral nature of the Dirac fermions becomes accessible. [13]
The poor screening of Dirac fermions, the Coulomb interactions remain long ranged and an electrostatic potential is build at the edges. The surface states are shifted in their position and charge transfer for these states is reduced. Further transfer of charge at the defects is induced to compensate this effect and maintain charge neutrality. The mechanism persists until charging energy of the edges is compensated by the kinetic energy of the electrons. As a result extra charge and large density of states is found at the edges, resulting in larger optical phonon shifts. [31]
Simulations on free standing graphene sheets showed that the bond configuration of the terminating edge atoms determines intrinsic stress, for shorter (longer) bonds it will become compressive (tensile) stress. This will significantly influence the surface morphology of the (free-standing) graphene sheet. The sheet's deformation reduces the edge energy and the electronic structure is altered by strain and shape deformation. By compressive forces, the sheet can buckle out of the surface plain, lowering the energy. [6]
In case of compressive edge stress the total energy is minimized by stretching of the edges inducing the formation of wave-like pattern at its edge. The amplitudes found for armchair edges were found to be significantly smaller than those of the zigzag edges. These patterns will also propagate away from the edge at a certain penetration depth that scales linearly. [6]

1.3.3 Strain relieve by rotation of graphene

A possible route to relieve the strain is the rotation of graphene. Weakly adhered graphene was found to exist in multiple orientations of Moiré structures on diffent transition metal surfaces. [1, 27] [3]The coexistence of more than one rotational phase on the same surface has been observed on Pt, Ir and Cu. A combined study of STM, MD and DFT on the Moiré of gr/Cu(111) showed the existence of six different phases. [27]

[3]With rotational angle R defined between the zig-zag line of carbon and atoms of Cu(111) along (110).

While three phases within this study were found only by simulations, [27] three have also been confirmed by experiment, the rotational phases R0, R7 and R10. [1, 27] With increasing rotational angle, the corrugation of the super structure was reduced, flattening from 45 pm at R0 to 3 pm at R16 for graphene. In addition, simulations showed, that the corrugation within the surface layer of Cu(111) also has been reduced (10 to 2 pm). [27]
Same trend was found for the periodicity of the superstructure, that decreased with increasing rotational angle. The lattice constant in the graphene sheet was insensitive to the rotation, being compressively strained to 244 pm by a lattice mismatch of 3.56 % for the R0 phase. For the R7 orientation a reduced mismatch of 3.44 % was found. [27]
R0 was found to be energetically closest to flat graphene, followed by the R7 configuration. These phases where the most observed phases in STM experiments. [1, 27]. Other experimentally observable phases required an higher energy amount, while the lattice mismatch remained unchanged or even increased. For structures found only in simulations, energy differences in respect to a perfectly flat graphene sheet were below the thermal activation energy at room temperature, explaining that these have not been measureable at room temperature. [27]

1.3.4 Pinning points of Moirè structures - impacting electonic properties

The rotational configuration of graphene directly affects the interaction with the substrate. Different work functions were measured for the different orientations of graphene domains on Pd(111) of up to 150 mV. For work function values lower than those of free standing graphene it was concluded that the formation of a dipole layer at the interface pointing away from the surface. This depends also on the orientation dependent strain of the domain. The strength of the effective dipole and the work function is a function of the domain orientation. This is also expected for other transition metals. [32] In the case of the weak interaction between graphene and Cu(111) a modulation by 30-35 meV was found on rotation . [18]
In case of graphene on Pt(111), the domains with the largest average separation were the ones found to be most frequent in STM experiments. These distances scaled with a reduced charge transfer on increasing separation, despite the one structure with the largest rotational angle. [22]
While simulations showed the graphene's lattice corrugation to be unaffected by the rotation, corrugation of Pt-surface atoms increased on increasing rotational angle. Summing both corrugation amplitudes it can be found an increase with increasing angle. [22]. Fairly in agreement with the observed orientational dependency on Cu(111). [27] Graphene's corrugation followed the surface corrugation. [23, 27]
Contrast switching for graphene in STM, confirmed by theory, was explained by the shift of the Dirac cone in respect to free standing graphene, breaking the electronic symmetry close to the Fermi level. [13, 22] Tunneling with negative (positive) voltages to occupied (unoccupied) states, the atomic graphene lattice (hollow sites) overlaid by the Moiré super-periodicity can be imaged. [22]

Charge transfer was found to occur from Pt towards graphene, resulting in an n-doped character, [22] also confirmed by theory. [7] for all super-structures. The shift within graphene may be explained by the consideration that the DOS is shifted to lower energy levels to accommodate the excess charge from the Pt by empty states, compared to non-deformed graphene. [22]
In case of the two largest deformations found for Gr and Pt, an electronic state was induced around the Fermi level, accommodating the large charge-transfer, with the shift of the Dirac cone considerably smaller than in the other structures. This was explained in terms of the atomic configuration of the pinning-points. While in case of the surface state a plateau of three Pt atoms is found, only a single Pt atom is forming a cusp in the other configurations. [22] Here a parallel to metal induced gap states (MIGS) can be drawn, where an interface state arises from the interaction of alkali halides with the metal substrate. [33]
This general concept of pinning points can be extended to other transition metal surfaces. In case of Pt it has been attributed to the metals malleability on interaction with the carbon. Atomic vacancies have been proposed to exist for various other transition metal surfaces. As a consequence the authors speculate that softer surfaces in comparison to "carbon could be prone to form well-localized pinning-points." [22] This is what one could expect in the case of copper.
The increased interaction at the pinning-points is induced by a chemical overlap, caused by a migration of electronic charge within Pt from the s- to the d_{z^2}-orbital. The orientation of the latter orbital becomes more perpendicular, facilitating the hybridization with the graphene's p_z-orbitals. [22] The latter in fact are a result of the rupture of the sp^2 hybridization by the buckling of graphene. [13]

1.3.5 Phononic properties of absorbed graphene and elasticity

The formation of the Moirè structures is also impacting the elastic properties of graphene. Strictly two dimensional graphene would have two acoustic and optical modes by the in-plane translation and stretching of the lattice. The extension in the third dimension by out-of plane oscillations results in additional acoustic and optical modes, called flexural modes. The softness of graphene is directly related to this out-of-plane vibrational modes, only present in 2D materials. These are responsible for the bending properties of graphene. In the presence of the long range order from the substrate a certain degree of order is maintained and ripples are formed. These can be considered as frozen flexural modes. [13]
While the acoustic flexural mode represent the translation of the whole plane in the orthogonal direction, the optical flexural mode represents the out-of-phase, out-of-plane oscillations of the carbon atoms. [13]
In graphite, the coupling of the planes leads to the lifting of the flexural modes degeneracy and a suppression of the flexural modes energies depending on the strength of the interaction. As the coupling is mediated by weak Van der Waals interactions, the flexural modes are maintained. [13] Here an analogy

for the weakly interacting, physisorbed graphene on a transition metal like copper or platinum, [7] can be drawn.
Long-wavelength elastic distortions, like those of a Moirè pattern, can be described by the elastic Lagrangian density, relating the flexural phonon disperion to strain and bending rigidity of graphene. [20]
The in-plane phonons have a linear dispersion, while out-of-plane phonons (flexural) have a quadratic dispersion, from their rotational symmetry. [20]
By the quadratic dispersion, the flexural phonons are dominating the behavior of structural fluctuations for low energies (low temperatures) and long wavelengths. [13]
In flat (free-standing) graphene all normal vectotrs, in term of elasticity, are aligned. An out-of-plane buckling leads to their misalignment, costing elastic energy depending on the bending stiffness of graphene. This is valid in the case of smooth distortions and absence of surface tension or any symmetry breaking. [13]
In case of tension, an additional energy term has to be added to the elastic energy to account for solid rotations of the sheet and depending on the interfacial stiffness. On a substrate, the graphene sheet is pinned by Van der Waals or other electrostatic potentials and tries to follow the substrates configuration. [13, 22, 23] Deviations from this configuration cost extra elastic energy, described by a harmonic potential and depending on the strength of the interaction. [13]
In free floating graphene the height oscillates harmonically with a given frequency, the long-wavelength dispersion of the flexural modes. From the dispersion it is also possible to relate the bending energy to the Young modulus of graphite, under the assumption to be valid at the single plane level. [13]

$$\kappa = Y * t^3 \tag{1.13}$$

Where κ is the bending stiffness, Y the Young's modulus, t the distance between the planes, and $\kappa = 1eV$ for $Y = 1GPa$ and $t = 0.34nm$. [13]
In the presence of tension the dispersion of the flexural modes is modified and becomes linear for momenta approaching zero. For example the inter-layer interaction in graphite breaks the rotational symmetry. [13]
The number of flexural modes per unit area is divergent in the thermodynamic limit $T \neq 0$, indicating that the system cannot be structurally ordered in free graphene at finite temperatures, known as the crumpling instability of soft membranes from thermal out-of-plane fluctuations. [13, 20, 23]
Non-linear effects like bending deformations within a Moirè structure, the presence of defects or phonon-phonon interactions or the coupling between flexural and in-plane modes, lead to the renormalization of the bending rigidity. [13]
Under tension or in the presence of a substrate, the dispersion becomes linear, with a finite number of flexural phonons. The free sheet can be flat in the case of tension, by time-averaging of the dynamic thermal fluctuations. When the sheet is suspended, these fluctuations become quenched resulting in static structures like ripples. [13]
In presence of a metallic gate, electron-electron interactions lead to coupling

of the phonon modes with the electronic excitations in the gate. This effect is responsible for the damping of the phonon modes by dissipative effects in graphene resonators. [13]

1.3.6 Electron-phonon interaction - linking electronic and elastic properties

Electron-phonon coupling in graphene directly relates graphene's electronic and elastic properties. The excitation's can arise from interband (ordinary electron gas) and intraband (semiconductor) contributions. [31] Large (low) doping, a shift of the fermi levels energy in respect to the dirac cone, [7] results into a hardening (softening) of the phonon modes, directly related to the disorder, like a Moirè, within the system. A change in the dopant concentration leads to a shift of the phonons wavenumbers, with larger (lower) concentrations softening (hardening) the phonon modes. The intraband contributions may dominate over interband transitions, depending on the amount of disorder. [31] For graphene on Cu(111) the Fermi level is shifted to lower energies, [7] leading to the expectation that graphene is softer than free graphene.
The excitation's are mediated by the distortion of the bond-lengths, that modifies the amplitudes of the nearest neighbor hopping energies. [13, 20] Phonons with energies comparable or larger than the Fermi level are shifted, determined by a dynamic electronic response. [31] The electron-hole asymmetry, induced by doping from localized states like point contacts formed within a Moirè super-structure, [22] will lead to a transfer of charge to unaffected regions within graphene, an effect called self-doping. [13]
The coupling can also be expressed in terms of a strain tensor, with a quadratic (linear) coupling term for the flexural (in-plane) phonons. While in-plane phonons are strongly coupled to the electrons, the linear dispersion results in a linear vanishing density of states for small energies. In contrast flexural phonons are weakly coupled, but have a constant density of states. [20]
Scattering of Dirac fermions by flexural phonons requires absorption or emission of two phonons, dominating the phonon contribution to graphene's thermal resistivity at low temperatures. [20]
The logarithmical divergence of the scattering rate from the quadratic phonon dispersion in flexural modes leads to a long-wavelength correction of the elastic constants and the phonon dispersion. This renormalization is responsible for the stability of the flat phase at low temperatures. In presence of disorder, the elastic properties of graphene are renormalized even at zero temperature. [20]

1.4 Cosorption of alkali halides on graphene-Cu(111) - edge-effect or intercalation?

This chapter will conclude with the hypothesis that graphene should be intercalated by KBr, in contrast to NaCl, mediated by a mechanism that reduces the overall strain within the system. Therefor, a brief tract on the interca-

lation of graphene and the strain mechanism for thin-film island coalescence will be given.

1.4.1 Intercalation of graphene

This section gives a brief overview on the intercalation of graphene. Succesfully intercalation was observerd for graphene on silicon carbide by hydrogen [34,35] and germanium. [36] Intercalation by gold has been observed for graphene on Ni(111). [37] And Ru(0001) was intercalated by oxygen. [38]
Different findings for a mechanism of the intercalation exist in the literature. For SiC, the intercalation process of germanium was observed to occurr directly through the graphene layer. [39]
In contrast the intercalation for graphene on Ir(111) by Cs was observed to takes place at wrinkle crossings and cracks. The strength of the interaction of Graphene on Iridium interaction is comparable to those of graphene on copper. [3] On increasing Cs-adatom density Coulomb repulsion become more dominant and a surface pressure builds up in the adlayer, that is relieved by intercalation of Cs. Initially intercalation is hindered by an effective energy barrier of 50 meV/C-atom (Thermal energy 3/2kBT is 38.78 meV), the necessary amount to delaminate graphene from the substrate. Intercalation is only favourable on formation of a dense Cs-layer formation when energy cost of delamination can be shared by many Cs atoms, with a partial delocalization of Cs s-electrons on intercalation. Van der Waals interaction was found to be an important factor for the intercalation, as a threshold concentration of adatoms was necessary to overcome VdW binding energy of graphene to Ir(111). [40]

1.4.2 Strain and the coalescence of islands

For thin film islands, internal strain arises as thickness and diameter are constrained on absorbtion on the substrate. The surface strain for many alkali halides is compressive. The overall surface stress on an growing island consists of two contributions for its thickness and its diameter. [5]

$$\sigma_t(t) = \frac{(f+g)}{\left(\frac{1}{t} - \frac{1}{t_0}\right)} \tag{1.14}$$

$$\sigma_d(d) = \frac{2\beta h}{\left(\frac{1}{d} - \frac{1}{d_0}\right)} \tag{1.15}$$

$$\beta = 1 + \frac{2S'_{13}}{\left(S'_{11} + S'_{12}\right)} \tag{1.16}$$

$$\sigma = \sigma_t + \sigma_s \tag{1.17}$$

S are elastic compliance's referring to the Cartesian coordinate system. f and g are stress of the island surface and the island\ metal interface respectively. In case of the sum of f and g being positive the thickness dependent contribution, dominating for the first binding of the nascent island crystallites to the metal surface, is predictive to become compressive. This also would explain the early stage of poly crystalline metallic film growth. Diameter depending intrinsic stress contribution depends on parameter beta. This value depends on the crystallographic orientation of the island and the elastic compliances. In case of an isotropic material beta can be rewritten as Poisson ratio: [5]

$$\beta = \frac{(1-3\nu)}{(1-\nu)} \tag{1.18}$$

Intrinsic stress depending on the island diameter has positive sign for β, in a compressive case and a negative sign of β in case of tensile strain. KBr has a negative β on surfaces with a (111) facet, showing compressive strain. In contrast NaCl has a positive sign for β and thus inherits tensile strain. [5]
When two islands come close grain boundaries are created anc the surface energy at this boundaries is reduced. At the cost of elastic deformation these islands can coalesce, reducing the surface energy. This mechanisms can induce large tensile (positive contribution) stresses. In cases where compressive stress is found before coalescence this mechanism can have an significant contribution, that will oppose the effect of grain boundary formation. [5]
For continuous growth after coalescence, the stress will remain tensile for metals with low adatom mobility. On the other hand the tensile intrinsic stress can be significantly decreased and in some case even become compressive when the mobility of the adatoms is high, e.g. for metal deposition at elevated temperatures, giving an implication on a temperature dependent relaxation mechanism. Compressive stress found for many metallic and dielectric surfaces may have its origins prior coalescence. Adatom diffusion from the grain surface to the boundary and incorporation can relieve surface energy tensile stress. When the diameter is much larger than the thickness, a compressive contribution can be continued by epitaxial growth at the boundaries and relaxation effect at the boundaries will be diminished. [5]

1.4.3 Hypothesis

If we think further from the findings of Petrović et al. we have to ask what kind of role does surface stress play, as a the adatom phase excerted a pressure on the grain boundaries of graphene. Analogue to Cu(111), there is no surface reconstruction for Ir(111) and the surface is tensile strained. [17] Metalic thin films known to maintain tensile stress on metal substrate. [5] Ir(111)/Gr comparable interactions as in Cu(111)/Gr. [3]
Surface stress may yield an explaination for a different behaviour of NaCl and KBr on the intercalation of graphene. While NaCl is tensile strained, its growth towards graphene's grain boundary lets expect a promotion of grain boundary effects, [5] effectively hindering the intercalation In contrast the

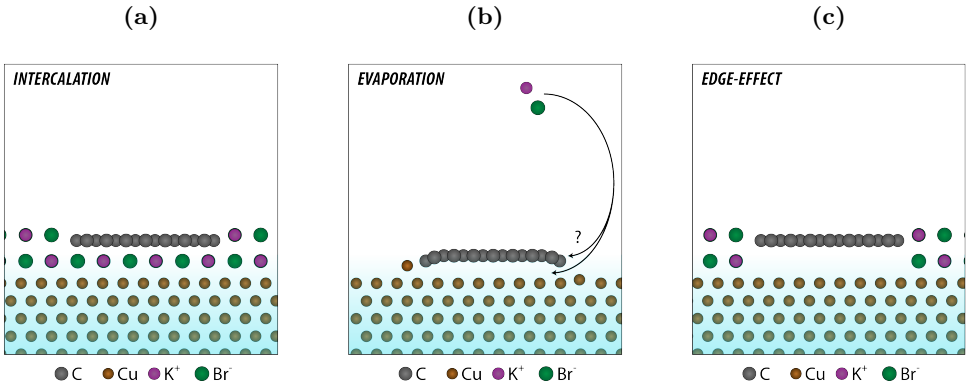

Figure 1.2: Two possible effects on evaporation of an alkali halide on the Gr/Cu(111) surface, either intercalation or edge-effect (growth over the flake also possible - add).

compressive KBr preferes a smooth growth, opposing the grain boundary formation. In addition, NaCl would deepen the tensile stress within the copper substrate, while KBr owing to compressive stress behaviour would release the tensile surface stress on the metal. [5]
As the main barrier for graphene island intercalation can be expected at the edges of graphene, this leads to the hypothesis, that an KBr will intercalate graphene in order to reduce the total strain in the system. In contrast for NaCl an edge-effect is expected, with island growth effectivly being stoped at the edges of graphene, leading to the formation of grain boundaries, as shown in figure 1.2.

Chapter 2

Methods

2.1 Scanning Probe Microscopy

2.1.1 Non-contact Atomic Force Microscopy

In this chapter an introduction to non-contact Atomic Force Microscopy will be given, as experiments throughout this work have been caried out with an AFM under UHV conditions operating at room temperature. In nc-AFM a cantilever is excited at its resonance with a constant amplitude. As the tip senses a force the shift in the frequency will be detected. Hence the mode is also called frequency modulated atomic force microscopy (FM-AFM). In this section only the first mode will be considered as the operation will be described as a damped driven harmonic oscillator. In xyz will discuss the use of higher modes in multimodal nc-AFM. The advantage of the AFM in regard to the STM is the capability of real space imaging of the atomic structure of a surface, disregarding if it is conductive or not. By means of FM-AFM comparable resolution to STM can be achieved, [41, 42] with true atomic resolution. [43]
The fundamental equation for an oscillating cantilever is based on Hooke's law, the force acting on a mass on a spring:

$$F = -kz \tag{2.1}$$

In frequency modulation (FM) AFM a cantilever is driven at a resonance frequency (f_0)with a set amplitude (A_0). [44] The angular frequency:

$$w_0 = \sqrt{\frac{k_{eff}}{m*}} = \frac{2\pi}{T} = 2\pi f_0 \tag{2.2}$$

The effective stiffness is defined as $k_{eff} = k_t + \frac{\partial F}{\partial z}$, where k_t is the stiffness coefficient of the cantilever. [44] When then cantilever is infinitely far away from a surface its motion can be treated those of a driven harmonic oscillator and the force gradient $\frac{\partial F}{\partial z} = 0$. Approaching the oscillating tip towards a surface gives rise to an interacting force and $\frac{\partial F}{\partial z} \neq 0$ resulting in a shift of the resonance frequency (Δf). The harmonic oscillation is weakly perturbed by the interaction and the cantilever can be considered as a weakly damped driven harmonic oscillator. [44, 45] [1]

[1] also referred to [46]

Driven damped harmonic oscillator equation of motion:

$$m_{eff}\frac{d^2z}{d^2t} + \Gamma\frac{dz}{dt} = -k(z - z_{drive}) \tag{2.3}$$

With $z = z_0 + cos(\omega t + \phi)$ and $z_{drive} = A_0 cos(\omega_{drive} t)$ the driving force of the cantilever. ϕ is the phase shift between the excitation and the cantilever oscillation, in case of $-\frac{\pi}{2}$ they are in resonance. $-\Gamma\frac{dz}{dt} = F$ is the friction force. With the Γ-coefficient:

$$\Gamma = \frac{m_{eff}\omega}{Q} \tag{2.4}$$

Friction has been discussed in 1.1.2 In case of conservative forces no change on approach occurs and the excitation of the driving force remains constant. In case of frictional processes at the tip sample junction an increasing excitation is necessary to maintain a constant amplitude.
Indirect measure of the tip sample interaction by frequency shift. The force has to be deconvoluted from the frequency shift.
Giessibl and coworkers [45] described the dependence of the frequency shift on the tip-sample force by the Hamilton-Jacobi approach, a first order perturbation theory. The cantilever motion then is considered as a weakly disturbed harmonic oscillator due to the tip-sample interaction over one cycle.

$$k\frac{\Delta f}{f_0} = \frac{1}{2\pi A}\int_0^{2\pi} F(z + A\cos\theta)\cos\theta d\theta \tag{2.5}$$

With $\theta = 2\omega t$ and $\omega = 2\pi f$
Also a normalized frequency shift for large amplitudes has been introduced by: [45]

$$\gamma = \frac{kA^{1.5}\Delta f}{f_0} \tag{2.6}$$

It could be shown that in the case of small amplitudes like by: [44]

$$\Delta f = \frac{1}{2\pi}\sqrt{\frac{k_{eff}}{m*}} \tag{2.7}$$

We now layed the foundation of nc-AFM discussing the monomodal bahviour of a cantilever. When considering nc-AFM normally the cantilever is driven at the first resonance. It it possible to use the second [47] or higher modes. Even the first torsional mode can be used. [48] The usage of these modes allow for measurements with higher resolution. However when used monomodal the stability is an issue that has to be considered to avoid jump into contact. This draw back can be circumvented by application of a bimodal setup. A technique introduced in 2.1.2.

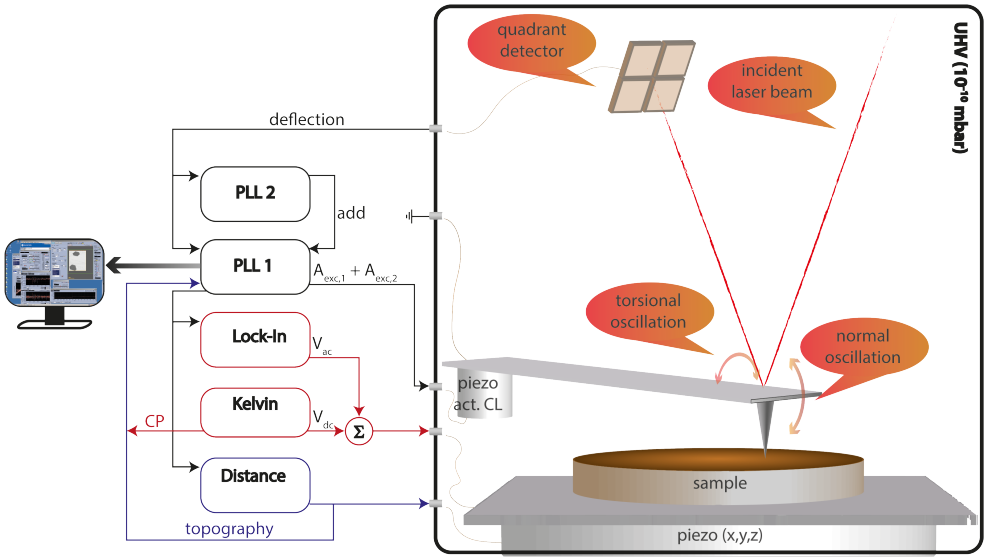

Figure 2.1: Setup scheme for a multimodal measurement at the RT Atomic Force Microscope, two independent PLL are employed for mechanical oscillation at different eigenmodes of the cantilever (CL). Via a lock-in and a Kelvin controller FM-KPFM is controlled.

Second flexural mode

The second mode is stiffer with higher spring contants and a Q-factor that is lower compared to the first mode, which is of advantage when considering very small amplitudes. As the force gradient is changing more rapid than the force, the second mode is more sensitive to short range forces. [49] With smaller amplitudes the equilibrium position of the tip is closer to the surface, but the closest approach is further away. The force gradient has to be smaller than the force constant to avoid instabilities or jump into contact. [47]

First torsional mode

The torsional mode showes a narrow potential well by the short-range forces from covalent bonding. The effect of long-range Van der Waals and electrostatic forces are minimized by the lateral tip movement,. A sample tilt could contribute to the signal by inducing a distance modulation. The mode is very sensitive to image dissipation on cuting covalent bonds or friction as Van der Waals friction. [48]

2.1.2 Multimodal nc-AFM

Kawai *et al.* showed that the resolution in nc-AFM can be increased drastically while maintaing stable measurement conditions in a bimodal setup.

This means that simultaneously two eigenmodes are driven by two independent phase locked loops (PLL). Originally the first flexural mode is driven at large amplitudes by a first PLL, ensuring stable measurement conditions. In addition, a second PLL is employed, actuating the cantilever at the second normal [49] or first torsional [50] mode. [2] The modulation at or close to a resonance by an AC-bias in Kelvin Probe Force Microscopy (KPFM) can also be considered as a bimodal technique.

bimodal-second mode

While challenging to operate the second mode in a monomodal setup, as tip or sample atom jumps may induce instabilities for amplitudes below 400 pm, a bimodal setup uses the full advantage of this mode. Kawai *et al.* showed that equation 2.5 can not only be applied for the second flexural mode but is also applicable in bimodal DFM, where the first PLL was driven in the first and the second PLL in the 2nd mode. [49] A generalized formula has been proposed, that accounts for n oscillation cycles, that can also be apllied to the case of electrostatic force in case of KPFM: [52]

$$k_i \frac{\Delta f_i}{f_i} = \frac{1}{2\pi A_i n_i} \int_0^{2\pi n_i} F\left[z(t)\right] \cos\theta_i d\theta_i \tag{2.8}$$

Where $z(t) = z_0 + A_1 \cos\theta_1 + A_2 \cos\theta_2$ when using the 1st and 2nd resonance. The formula is valid as long as $\Delta f_i / f_i \ll 1$. For the first mode, when $A_{1st} \gg \lambda$ with λ the short range decay length (100 pm [49]). In this case most of the contribution within the integral is assumed to come from the turning point where $\cos\theta_1 = -1$: [50]

$$k_{1st} \frac{\Delta f_{1st}}{f_{2nd}} = -\frac{1}{4\pi} \int_0^{2\pi} F'(z_0 + A_{1st} \cos\theta_1) d\theta_1 \tag{2.9}$$

In case of the 1st mode, a high amplitude is required to avoid jump into contact. In case of the 2nd mode jump into contact is avoided even for small amplitudes when the spring constant is large enough. [47, 49] As 1st and 2nd mode are incommensurate only the force component oscillated with f_i contributing to the ith integral. In case $A_2 \ll A_1$ the contribution of the second mode is averaged to zero over time and the first mode can be considered as independent as in conventional DFM and the general formula 2.8 is equal to those of 2.5 by Giessibl. [45] Under the assumption that the second mode is densely sampled over a single cycle of the first mode following equation:

$$k_{2nd} \frac{\Delta f_{2nd}}{f_{2nd}} = -\frac{1}{4\pi} \int_0^{2\pi} F'(z_0 + A_{1st} \cos\theta_1) d\theta_1 \tag{2.10}$$

[2] Ultimately up to ten eigenmodes of a cantilever can be exited by a multiple lock-in technique. [51]

bimodal-torsional mode

The general formalism in equation 2.8 could also be applied to the torsional mode in bimodal DFM. [50] The generalized equation from [49] was slightly modified to:

$$k_i \frac{\Delta f_i}{f_i} = \frac{1}{2\pi A_i n_i} \int_0^{2\pi n_i} F_j \left[tip(X,Y) \right] \cos\theta_i d\theta_i \tag{2.11}$$

Where F_j is the dependence of the force on the direction of tip motion, in either X or Z and $tip(X,Y) = A_{tr}\cos\theta_{tr}, z_0 + A_1\cos\theta_1$the tip-position in the x,y-plane. For the torsional driven on the second PLL this becomes analogue to the 2nd mode, but dependent on the force gradient along X:

$$k_{tr} \frac{\Delta f_{tr}}{f_{tr}} = -\frac{1}{4\pi} \int_0^{2\pi} F'_X(z_0 + A_{1st}\cos\theta_1) d\theta_1 \tag{2.12}$$

From the independence to long range forces, except at step edges, arises a strong sensitivity to short range forces in the attractive regime. By using small torsional amplitudes in relation to atomic distances averaging effects are avoided and a time averaged lateral force gradient in quasi constant height mode can be recorded for large first amplitudes. The features have an angle dependent offset and amplitude dependence in respect to the dithering direction. [3]

We now had the assumption that the first PLL was driven with a large amplitude on the first mode, $A_{1st} \gg \lambda$. In this regime the amplitude is much larger than the length of interaction. What happens if we drive the 2nd mode on the first PLL with a rather small amplitude of 600 pm and the torsional on the second PLL? Then $A_{2nd} > \lambda > A_{tr}$.

Contrast formation on graphene in nc-AFM

We will now focus on a study that is related to AFM. Atomic contrast in nc-AFM on graphene on Pt(111), and for suspended graphene in general, is related to the short-range tip-sample interactions. [26]

Dissipation in nc-AFM by the global (few nanometer) deformations of the graphene layer by the tip. [26]

Differences in the atom-by-atom stiffness depending on the coupling strength with the substrate are taken responsible for the Moiré contrast. [26]

Hysteresis in the dissipation signal on approach and retract by non-conservative tip-sample interactions. An aprupt increase to a plateau in dissipation on approach has been found. [26]

First atom sites more attractive, at closer distance hole sites more attractive, resulting in a change in contrast at the minimum of the interaction potential.

[3] The paper describes measurement on graphite. Strongest attraction along vertical axis on hollow site due to short range decay length close to carbon bond (further info in ref [50]). These become visible as maxima in normal mode. in torsional these should be maxima in the frequency shift having the strongest negative lateral force gradient, bridge sites the most negative tr shift, altered by the orientation of the site in respect to the dithering x-direction

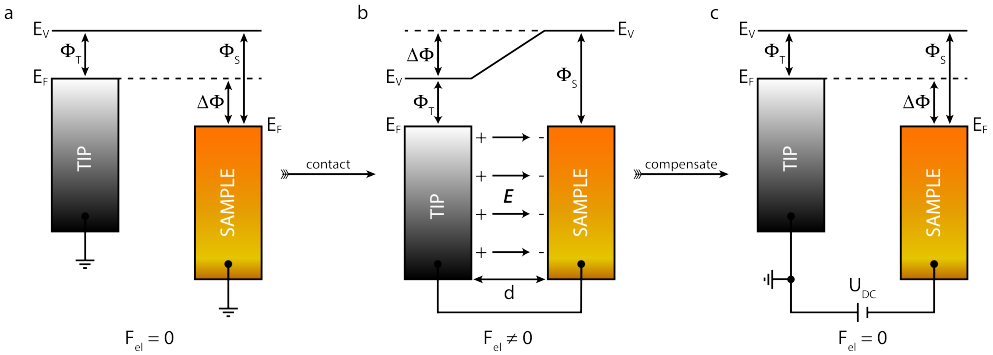

Figure 2.2: Principle of Kelvin Probe Force Microscopy. In a) sample and tip are separated from each other. The vacuum level is aligned. When a connection is made, e.g. by a wire, the Fermi level of tip and sample align. By difference in the work function the vacuum energy level becomes misaligned. The generated electric field causes an electrostatic force. When a DC-bias equal to the work function difference is applied c) the electrostatic force is compensated and the vacuum level are realigned.

The process is dominated by Pauli repulsion. [26]
Graphene was found to adhere in the upper attractive regime and force curves become distinguishable on approach and retract. [26]
Moiré contrast not direct by the tip-Pt interaction, but the effect of the binding between graphene and the substrate on indentation of the tip. Fixed carbon atoms in simulations showed no Moirè contrast as well. [26]
While tip-graphene distance is only slightly varying in the repulsive regime, the interface distance is changed, changing and measuring the local stiffness of the carbon atoms, measured as a Moiré. [26]
Tip induced detaching of graphene could explain the dissipation in the attractive regime. On approach graphene is attached to the substrate, when retracting the tip, graphene locally adheres to the tip for a short period of time, inducing large scale deformations. [26]
On adherence of graphene, when the tip is retracted, a large attractive force results, keeping the distance between graphene and the foremost tip atom almost constant and increasing the distance between carbon and platinum. [26]
The Moiré contrast in the attractive regime comes from the different local potential of the Pt-G interaction on high and low sites of the superstructure, that can be sensed by the large deformation on the retraction, mapping the local stiffness of graphene. [26]
Tip induced deformation should also appear in STM experiments. [26]

2.1.3 Kelvin Probe Force Microscopy

The working principle in KPFM is based on the Kelvin principle to measure the surface potentials. In the original setup two parallel aligned plate capacitors, whose concept was introduced in 1.1.1. By vibrating one capacitor plate, an alternating current by the periodic change of the distance in between the

two plates is induced. This current can be nullified by applying a proportional dc-bias to one of the plates. The applied voltage becomes the contact potential difference (CPD) between the two materials. If the work function of one plate is known, the work function of the other plate can be derived by the measured CPD. UHV condition is of utmost importance, as the sample has to be clean. [53]
The Kelvin principle can be applied to conventional nc-AFM, a technique called Kelvin Probe Force Microscopy (KPFM). By applying the dc-bias between the tip and the sample the electrostatic force is compensated, see figure 2.2 c. While in the original method the ac-bias is controlled, in KPFM the electrostatic interaction becomes the controlled parameter. The tip is modulated with an applied ac-bias inducing an electrostatic force. With the Capacitor energy 1.3 the electrostatic force between tip and sample along z is:

$$F_{el} = \frac{1}{2}\frac{\partial C}{\partial z}V^2 \tag{2.13}$$

As a dc-bias and an ac-bias are applied this becomes:

$$F_{el} = -\frac{1}{2}\frac{\partial C}{\partial z}\left[V_{dc} - V_{CPD} + V_{ac}\sin\left(\omega_{ac}t\right)\right]^2 \tag{2.14}$$

With V_{CPD} being the the work function difference between the tip and the sample:

$$V_{CPD} = \frac{\Delta\Phi}{e} = \frac{\left(\Phi_{sample} - \Phi_{tip}\right)}{e} \tag{2.15}$$

This notion of V_{CPD} is such that a change directly corresponds to the work function change, allowing for an easier interpretation of images. In the experiment this is achieved by applying the bias to the sample, while the tip is grounded. The electrostatic force can further be described by three components:

$$F_{dc} = -\frac{\partial C}{\partial z}\left(\frac{1}{2}\left(V_{dc} - V_{CPD}\right)^2 + \frac{V_{ac}^2}{4}\right) \tag{2.16a}$$

$$F_{\omega_{ac}} = -\frac{\partial C}{\partial z}\left(V_{dc} - V_{CPD}\right)V_{ac}\sin\left(\omega_{ac}t\right) \tag{2.16b}$$

$$F_{2\omega_{ac}} = \frac{\partial C}{\partial z}\frac{V_{ac}^2}{4}\cos\left(2\omega_{ac}t\right) \tag{2.16c}$$

Clearly visible is the gradient dependence and the cancellation of the electrostatic forces when a dc-bias equal to the CPD is applied. While 2.16a contributes to the topography, the CPD is measured with 2.16b. By 2.16c the capacitance can be measured. The employment of KPFM is also mandatory to measure the correct topography in case of complex surfaces with more than two different materials. [53] Two different modes in KPFM can be applied, amplitude modulation (AM-KPFM) and frequency modulation (FM-KPFM).

Local contact potential difference

Sadewaser *et al.* found that with the onset of the short range forces a strong modulation of the contact potential can be detected, visible as atomic contrast in the CPD. This contrast was explained by variations within the surface dipole and the local chemical potential. [54]
While the CPD is based on the work function of equation 1.1 it is per definition referred to $z = \infty$. As the tip approaches towards the sample in the short range region this defininition is not valid any more and the gradient of the electrostatic potential is measured, in agreement with the concept of the local work function by Wandelt *et al.* introduced in 1.1.1. [8]
The resulting distance dependent change of the contact potential and an increasing sensitivity towards the short ranged modulations of the potential in the xy-plane is in agreement with the results of Sadewasser *et al.* This distance dependence of the local contact potential difference (LCPD) has also been observed for in other experiments. [52, 54, 55] In addition, for NaCl an amplification of the local contrast by the tip induced movement of the ions has been observed. [55]
Effects that are also expected to be detectable for adsorbed graphene, by its charge modulation from graphene's Moirè structure [13] and from the local movement of graphene by a sensing probe, potentialy amplifying those modulations. [26] An investigation on this hypothesis by KPFM measurements on absorbed graphene is presented in chapter

Bias sweep spectroscopy

In a bias spectroscopy the contribution of the electrostatic force to the tip sample forces is modulated by sweeping the bias at fixed tip sample distance. The expected frequency shift response is a parabola. By fitting the response according to formula for the electrostatic contribution according to Guggisberg *et al.*, the maximum of the curve can be derived. The contribution of the electrostatic force is minimized close to zero at this point, representing the contact potential difference.
By repeating bias spectroscopies and reducing the relative tip sample distance in between each recorded curve, a bias-distance spectroscopy is acquired. In a typical experiment the first curve is recorded only a few nm away from the surface in the range of short range forces. To account for an offset by long range electrostatic forces, a separate long range spectroscopy has to be recorded. It is also possible to account for these contributions by fitting the tail of a single spectroscopy the long range contribution. Parabolic dependence of the frequency shift on the bias voltage. Fitting to obtain the evolution of the compensated electrostatic force. Distance dependent curves extracted along this profile will be marked by a star.
The distance scale timresponse corrected for time-averaged cantileved deflection. [56] From the difference of the shifted and the original curves the frequency shift by the deflection was extracted. The raw data has been interpolated with bi-cubic spline along the distance axis on a fine grid, allowing for the extrapolation of the frequency response of the time averaged deflection.

Data belonging to the time-averaged deflection will be referred to as deflection (defl.).
To compensate for drift inherent to room temperature measurements, the atom tracking function, implemented in the Nanonis interface, was employed, y taking the slope of a Moiré hill as a reference within the torsional frequency shift. The advantage of tracking the torsional frequency shift lay in the higher resolution, facilitating the tracking, refer to figure 5.1. In the following sections the description of the site will be referred to the topography.

2.1.4 Convolution of force and force gradient

Fitting frequency shift

Guggisberg *et al.* [57] related 2.5 to force components, $F_z \cong F_{chem} + F_{VdW} + F_{elec}$ leading to $\Delta f_z \cong \Delta f_{chem} + \Delta f_{VdW} + \Delta f_{elec}$. Where F_{chem} includes all short-range interactions, like ionic, metallic and covalent bonding.

$$\frac{\Delta f_{elec}}{f_0} kA = -\frac{\pi R (U_V - U_{CPD})^2}{\sqrt{2\bar{s}A}} \tag{2.17}$$

$$\frac{\Delta f_{VdW}}{f_0} kA = -\frac{A_H R}{12\bar{s}\sqrt{2\bar{s}A}} \tag{2.18}$$

truncated Morse, as assumed only attractive interaction regime for measurement, this is per definition the regime of nc-AFM:

$$\frac{\Delta f_{chem}}{f_0} kA = -\frac{U_0}{\sqrt{\pi A\lambda}} \sqrt{2} \exp\left(-\frac{s - s_0}{\lambda}\right) \tag{2.19}$$

The individual contributions are proportional to the half-integral of their respective force. As it will be shown shortly this is in agreement with the derivation of bimodal frequency shifts by Herruzo *et al.* [58]
In the following sections these equations will be applied by fitting the data from a bias sweep spectroscopy. In 2.1.4 the common fitting will be demonstrated. In 5.2 a new approach to fit a bias sweep spectroscopy will be presented.

1D Electrostatic fitting

A common way to obtain the data along the compensated electrostatic force is the fitting of a bias sweep spectroscopy along the axis of the swept bias with parabola.

The spectroscopy presented in figure 2.3 a) was measured over a hill site on $Gr/Cu(111)$. A full presentation of the data will be presented in chapter 4. This data was fitted along the bias axis by means of equation 2.17, linewise for each relative distance. A map recalculated from the fit results is shown in figure 2.3 b). Despite the oscillations, visible at lower distances in a), the shape of the data was well reproduced by the fitting. At each distance the maximum of the parabola $U_{CPD}(d)$ was obtained, where the electrostatic force was compensated. Along this cross-section the data will be presented.

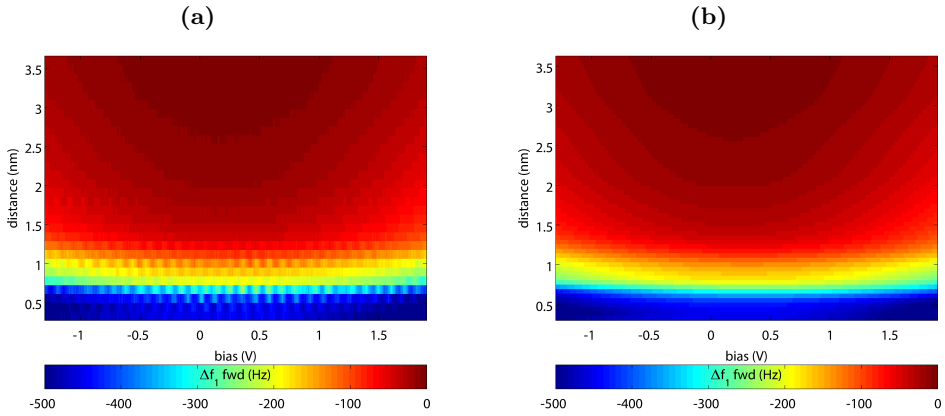

Figure 2.3: Comparison of raw data and map reconstructed from fitting the electrostatic contribution. hill site on $Gr/Cu(111)$.

By definition data along the cross-section of the compensated electrostatic force will be marked by a star.

In figure 2.4 a),the data was compared with the fit along the compensated electrostatic force. In the range of long-range forces, above 1.2 nm very good agreement between fit and data.
The fit model no longer represented the data as the dependence on the voltage by the power of two no longer agreed. The goodness of fit complemented the observation that the observed frequency shift became more flat as a reduced validity of the model was found in the more flat regions. Indicated by adjusted root square fitting shown in d). Good validity found till 1.1 nm, visible as yellow ribbon in the map, coinciding with the first maximum in the bias. The distance dependent contact potential, shown in figure 2.4 d), was found to be constant until the relative distance of 1.5 nm. For this region, the constant electrostatic force gradient was considered as the contact potential, as referred to $z = \infty$, as discussed for the LCPD in 2.1.3. A Gaussian distribution yielded a CPD of $0.19 \pm 0.04V$ ($0.17 \pm 0.05V$.). Broad distribution for the radius. The radius was found to increase in correlation with the bias, exhibiting peaks at the same position. Good agreement in the long range, while not at short distances, logic as electrostatics a long range force and contact potential defined as z being infinite. Radius and bias appear to be interfering. The radius can be considered as a factor that determined the curvature of the frequency shift in equation as the dependence of the voltage on the power of two was fixed.

2D fitting of all contributions

An alternative approach is the fitting of the whole data-set for electrostatic, Van der Waals and Morse contributions at once.

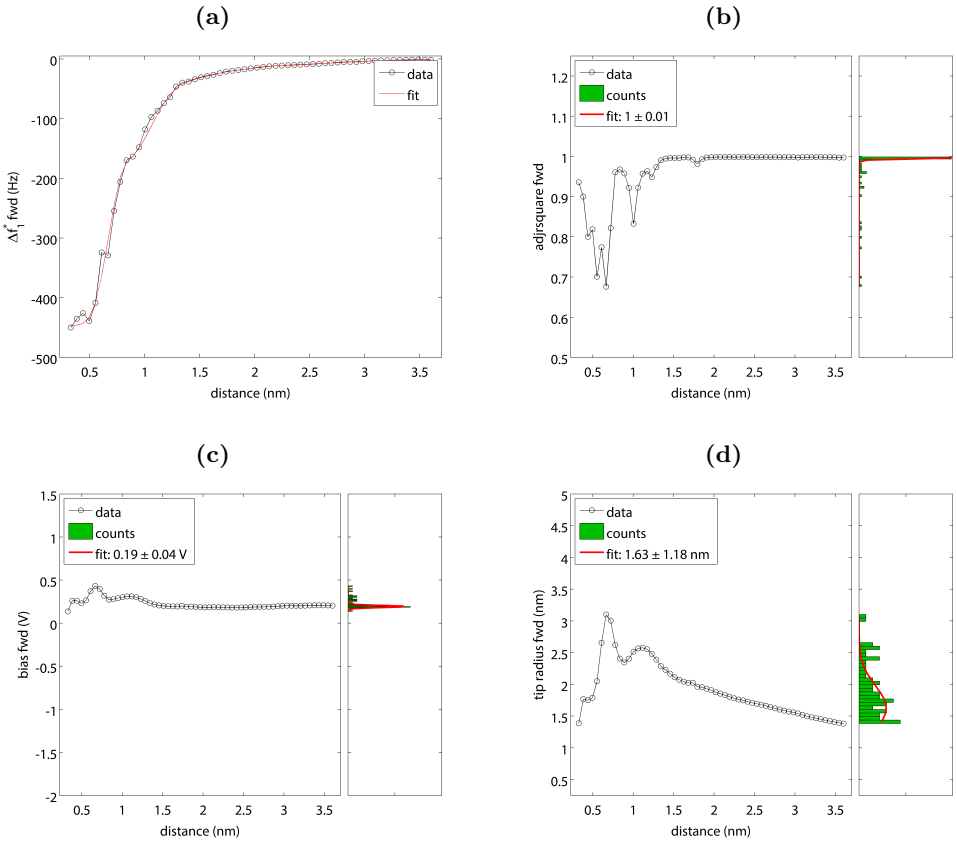

Figure 2.4: Along the compensated electrostatic force. Comparison of fit and data. a). Goodness of fit represented by the adjusted mean-root square error in b), Change in contact potential c). Tip radius obtained by the fit model d). Right panel in b)-d) normalized histogram of data, fitted by a Gaussian distribution.

Calculation of forces

Several methods have been proposed to derive the tip-sample forces from DFM data. [46, 58, 59] All methods have equation 2.5 in common as starting point. This equation is convoluted with a semicircular weight function of the amplitude. [45]

$$k\frac{\Delta f}{f_0} = -\frac{1}{\pi A^2}\int_{-} A^A F(z_0 + A + u)\frac{u}{\sqrt{A^2 - u^2}}du \tag{2.20}$$

The methods by Sader and Jarvis [59] and by Herruzo and Garcia [58] have the same Ansatz by interpreting the frequency shift as a fractional differential operator of the tip-sample interaction force. The peculiarity of the approach by Herruzo and Garcia is the dedication to bimodal DFM. In both Ansatz equation 2.20 is Laplace transformed. The transform includes a modified Bessel function. While the Sader-Jarvis method continues with an Pade approximant to facilitate numerical treatment of the Bessel function, the Herruzo-Garcia

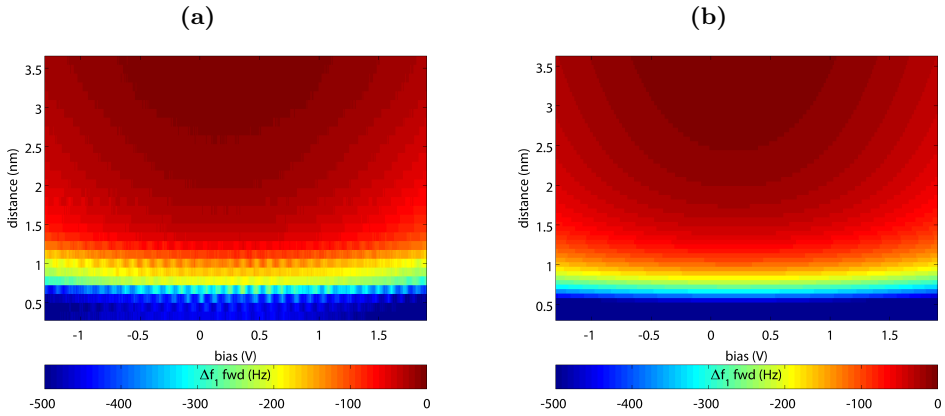

Figure 2.5: Comparison of raw data and map recalculated from the fitting.Results for the fitting of the frequency shift for a hill site on $Gr/Cu(111)$

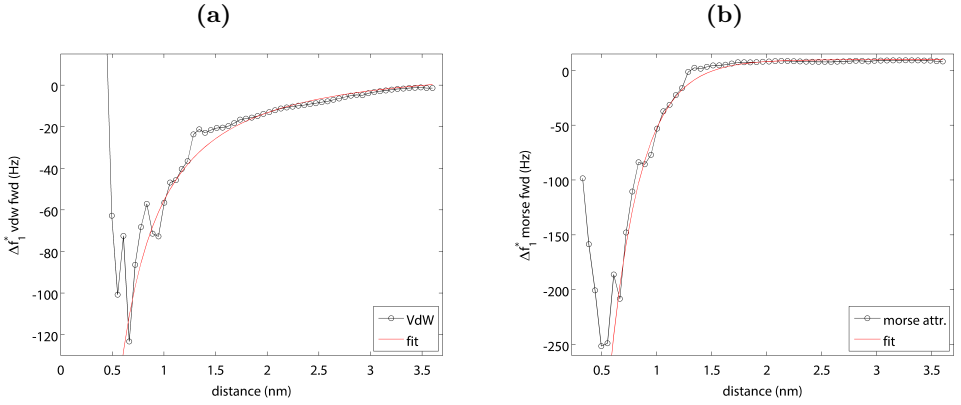

Figure 2.6: Residual frequency shift compared to the fit contribution for Van der Waals a) and Morse b).

method does not use any assumption.

Sader-Jarvis

Force deconvolution by Sader and Jarvis:

$$F(z) = 2k \int_z^\infty \left(1 + \frac{A^{1/2}}{8\sqrt{\pi(t-z)}}\right)\Omega(t) - \frac{A^{3/2}}{\sqrt{2(t-z)}}\frac{d\Omega(t)}{dt}dt \tag{2.21}$$

t-z is the covered tip-sample distance. $\Omega(t) = \Delta f / f_{res}$. By integration the potential is written as:

$$U(z) = 2k \int_z^\infty \Omega(t)\left((t-z) + \frac{A^{1/2}}{4} + \sqrt{\frac{t-z}{\pi}} + \frac{A^{3/2}}{\sqrt{2(t-z)}}\right)dt \tag{2.22}$$

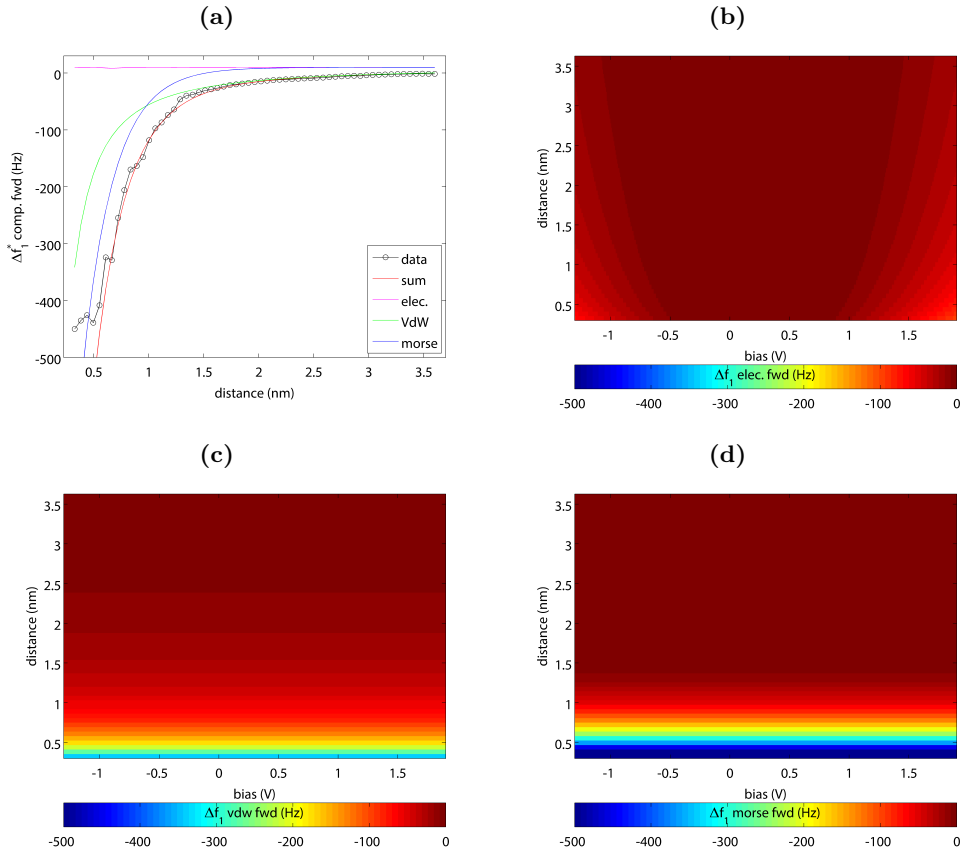

Figure 2.7: Individual contributions recalculated from fit results. Comparison data to contributions and total a). Recalculated maps for electrostatic b), Van der Waals c) and attractive Morse d).

While equation 2.21 can only be used in case of conservative forces, independent of the nature of the force. This formalism in [59] later has been extended, by decomposing the total tip-sample in conservative (even) - where the equation above remains valid - and dissipative (odd) forces $F_{int} = F_{even} + F_{odd}$. By applying the same Ansatz the odd force becomes accessible by multiplying the tip velocity with the generalized damping coefficient that is expressed as follows: [60]

$$\Delta\Gamma(z) = -b\frac{\partial}{\partial z}\int_{z}^{\infty}\left(1+\frac{A^{1/2}}{8\sqrt{\pi(t-z)}}\right)\Theta(t) - \frac{A^{3/2}}{\sqrt{2(t-z)}}\frac{d\Theta(t)}{dt}dt \quad (2.23)$$

With $\Theta(t) = \Delta F_0(z)\ \bar{F}_0 - \Delta f/f_{res}$, $\bar{F}_0$ is the driving force in absence of any force and $b = \Gamma - \Delta\Gamma$.
As shown prior, the first and second flexural modes are dependent on a semi-circular weight function for a large amplitude in the first PLL. Further mathematical treatment showed the dependence on half-derivative and half-integral of this modes.
As the deconvolution by the Sader-Jarvis method of the tip-sample force is

irrespective of the nature of this forces it is applicable to the extract the z-dependent evolution of the lateral force.

2.2 Sample preparation

2.2.1 Copper single crystal

The copper surface was prepared by several cycles of sputtering and annealing. For the sputtering, Ar was used. Applied energies ranged between 800 and 1000 eV, under an current of 10 mA. Sputtering times of 10 to 20 min were used. After sputtering the sample was annealed at 500 °C for 15 to 20 min.

2.2.2 Graphene growth by chemical vapor deposition

Graphene has been prepared according to Gao *et al* be repeated high temperature flashes in UHV. [1] The sample first was heated to 300 °C. The ethylene precursor gas then was dosed through a nozzle on the sample. The nozzle was separated by 10 mm and tilted by an angle of 45 ° in respect to the surface normal. The dosing increasing the pressure in the preparation chamber to from e-10 mbar to 1.8 e-6 mbar, with higher local pressures on the sample. The pressure was allowed to stabilize within 5 min. For one flash the temperature was increased by 5 °C/s to 950 °C. The dwell time at the elevated temperature was one minute. Afterwards the heating was switched of and the sample cooled down to 300 °C. The temperature flash was repeated three more times. At the end of the fourth dwell, the gas flow was stopped. After the manipulator has been cleaned, the sample was annealed at 600 °C for ten minutes.

Chapter 3

Overview by nc-AFM and KPFM

Within this chapter measurements of graphene on Cu(111) by nc-AFM and FM-KPFM are presented within the first section. By KPFM the work function of graphene on copper was measured for the first time. In the following sections the effect of the co-adsorption of NaCl in 3.2 and KBr in 3.3 will be presented.

3.1 Graphene on Cu(111)

Hexagonal flakes were grown on larger terraces of the stepped copper surface, refer to the topography in figure 3.1 a). These were identified as graphene by the hexagonal Moire structure, shown by the inset imaged taken from the center of the central flake. The hexagonal shape of this flake was irregular, as it appeared extended over the step edge (right red arrow). From the topography it was uncertain if graphene had grown continuous over the step. The appearance of the step edges within graphene areas (red arrows) appeared identical to the steps on the bare copper substrate (blue arrow). Measured between the corners marked by an X, the circumradius of the hexagon was approximately 75 nm.

Visible by the red line, a cross-section over the topography of the flake has been taken, shown in the upper part of figure 3.1 b). On the left side, the copper surface was rougher, with a step height equal to three monolayer (ML) (green double arrow). With a height of 340 pm, graphene (further referred to as Gr_i for initial graphene, meaning graphene on a clean copper surface) appeared more elevated (red double arrow) compared to the right side (orange double arrow) with 274 pm. A copper step (black double arrow) underneath the flake was consistent with the height of the copper terrace on the right side. In addition this step explained the elevation found on the left edge of graphene but was inconsistent on the right edge . However such a step was not visible in the topography.

In 3.1 c), the image of the CPD is shown. A strong contrast between copper (Cu) and graphene (Gr_i) was found. Copper steps, were visible by a lower work function on the substrate. Steps were also visible within graphene (red arrows), with lower contact potential compared to the flake. This clarified, that graphene was grown continuous over the step edge and followed directly the copper steps. However only higher steps were resolved (red arrow and upper end of red double arrow), lower steps were not resolved in the CPD (lower end of red double arrow). With increasing height of the step, the contrast in the CPD became stronger. Steps of one atom layer height were not resolved. This applied also for copper. The CPD could not clarify the height difference on the graphene edges, found in the topography.

The cross-section of the CPD, shown in the lower graph of figure 3.1 c), revealed a difference of -938 mV for the work function of graphene (red double arrow).[1] For the high copper step a reduction of 237 mV in respect to the contact potential of copper was found.

To obtain a more accurate measure of the CPD between graphene and copper a histogram of the CPD is presented in figure 3.1 d). Two peaks were clearly visible. For copper an asymmetric peak shape was found on the left peak side. The asymmetry could be attributed to the CPD reduction by the steps. Both peaks were connected by a small number of counts by the transition at the graphene-copper edge. To obtain the contact potential difference, both peaks were fitted by a Gaussian distribution. A difference of 828.9 mV was found,

[1] Note that the voltage was applied to the tip. The lower contact potential then equals to a lower work function. Refer to chapter **??** for further details.

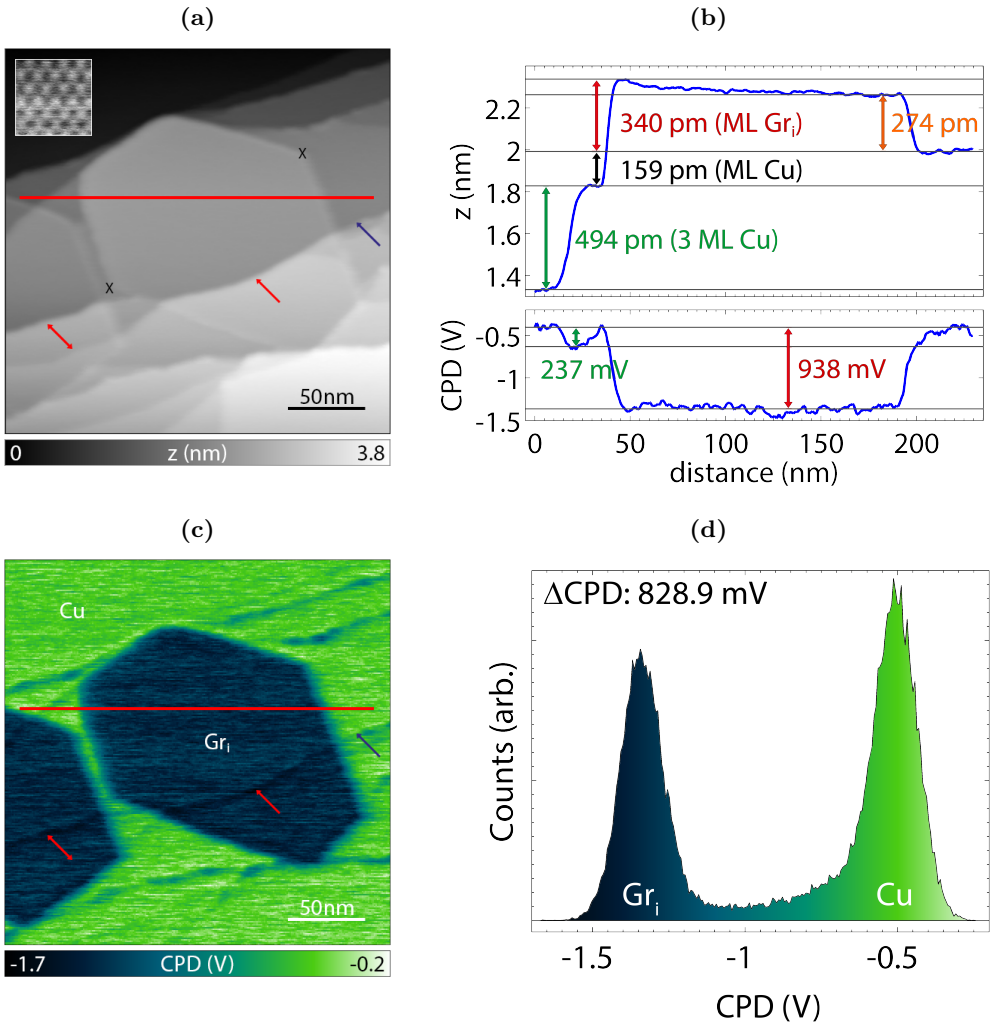

Figure 3.1: Graphene islands on Cu(111) measured by nc-AFM and FM-KPFM. Topography showing hexagonal flakes grown on terraces in a). 30x30 nm inset in a) showing Moire structure imaged at flake center. The CPD showed a clear difference between graphene and copper, refer to c). Cross-sections (red lines in a) and c)) are presented in b). Histogram of the CPD visible in d). Preparation parameter: 4 thermal flashes, $T = 950\,°\mathrm{C}, T_{dw} = 1min$. Gr_i denoting initial graphene. Imaging parameter: second mode, $\Delta f = -8\,Hz, f = 982.399\,kHz, A = 600\,pm, Q = 10'520$; FM-KPFM, $\Delta f = 210\,Hz, A = 1\,V$; inset parameter: $\Delta f = -31\,Hz, V_{dc} = -1.38\,V$; growth parameter: 4 flashes, $t_{dw} = 1min, T_{dw} = 950\,°C, p = 1.8e-6mbar$

more than 100 mV lower compared to the value obtained from the cross section.
In this section the structural and the electronic properties of graphene flakes on Cu(111) have been presented by nc-AFM and FM-KPFM. A separation of 340 pm between graphene and copper was found, well in agreement with For Height of graphene on the left agreed well with literature. Discrepancy to the height on the right side and not visible copper step may explained by partially grown into copper. Step bunching [] and high mobilty of copper during growth. [24]. Mono steps may were not resolved.
The measured CPD DFT calculations by Khomyakov *et al.* predicted a work function difference between graphene and Cu(111) of 820 mV. According to the plate capacitor model, discussed in 1.1.1, a CPD of 837.7 mV was calculated and a shift in the Fermi level of 257.7 meV in respect to free standing graphene. between these distributions was in very good agreement with the calculated CPD. A detailed study of electronic and elastic properties of graphene's Moire super structures on Cu(111) will be presented in chapter 4. The following section will continue with effects of the of sodium chloride co-adsorption to graphene on Cu(111).

3.2 Evaporation of NaCl to graphene on Cu(111)

The topography for the co-adsorption of graphene and NaCl on Cu(111) is presented if figure 3.2 a). Free graphene islands were found, visible at the bottom. The edges were decorated by clusters of the alkali halide (orange arrows). The graphene flake, visible in the upper region of the image was directly interfaced by a large NaCl island. This flake was grown into the copper step at its lower edge (blue arrow). On the NaCl carpet smaller islands were found, refer to the top of the topography.
Along the red line a cross-section was taken, shown for the topography in the upper half of figure 3.2 b). The separation between graphene and copper was 450 pm (red double arrow). As the flake has been grown into the large copper terrace, the deduction of the effective separation was impeded. Reducing the found separation by a layer copper underneath, the reduced separation yielded 290 pm. Note that the flake in the lower right corner of the images was separated by 330 pm. The height of NaCl on the left side of graphene was composed of several layers. A monolayer had a measured height of 154 pm (orange double arrow).
In figure 3.2 c) the image of the CPD is shown. Graphene was clearly distinguishable from copper and NaCl, by about 700 mV and 200 mV respectively. The small islands on the NaCl carpet were visible by lower contact potential referred to the carpet.
The cross-section of the CPD is shown in the lower part of figure 3.2 c). A contact potential difference of 892 mV was found for graphene in respect to copper and of 258 mV in respect to the alkali halide. The difference between two NaCl layer was found as 58 mV.
A histogram for the CPD is presented in figure 3.2 d). By means of Gaussian distributions the peak positions were determined. The CPD for graphene in

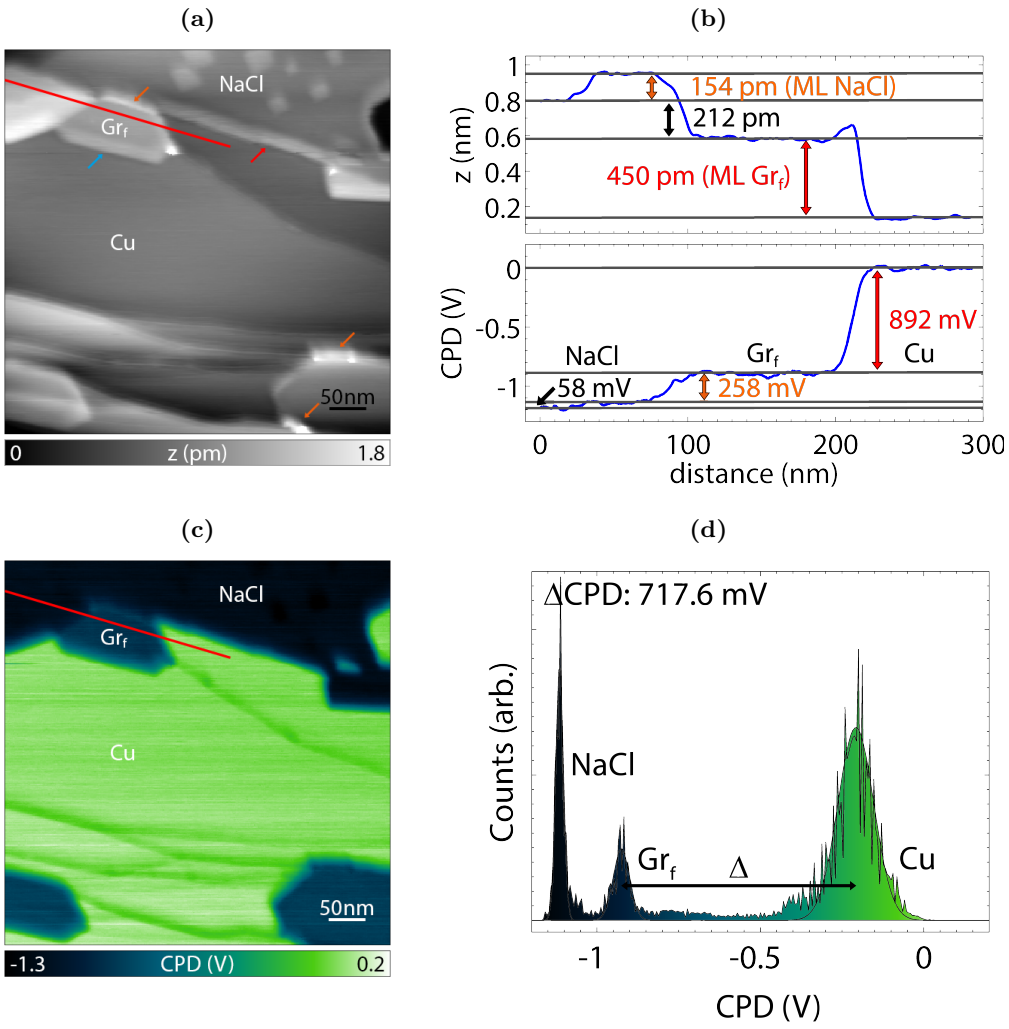

Figure 3.2: Hexagonal graphene flakes on Cu(111) in presence of NaCl. Minor changes in the work function of graphene. KBr partially grown over the edges. Preparation parameter: 460 C, 0.23 Ang/min, 12 min, Te 100 C, P 2.5 e-10 mbar; imaging parameter: first mode, $\Delta f = -21\,Hz, f = 164.524\,kHz, A = 6\,nm, Q = 31'064$; FM-KPFM: $\Delta f = 210\,Hz, A = 1\,V$.

reference to copper was measured as 717.6 mV. In respect to NaCl the CPD was 188.5 mV. For the alkali halide and copper a contact potential difference 906.1 mV was found.
The results for the co-adsorption of sodium chloride to graphene on copper showed only minor changes. Despite the difficulties to measure the correct separation of copper and graphene, a value more comparable to graphene on clean copper was found. By FM-KPFM a shift in the work function of graphene by 111.3 mV in respect to graphene on copper has been found.

3.3 Evaporation of KBr to graphene on Cu(111)

Graphene (referred to as Gr_f, as final graphene after the co-sorption of an alkali halide), visible in the lower part of figure 3.3 a), was grown over three larger terraces forming a well defined hexagon. Shadows, visible at the bottom of the terrace edges, were artifacts by the data-leveling. A circumradius of 100 nm was measured between the corners marked by an X. Shown by the inset is the hexagonal Moire structure obtained at the center of the flake. Note that the structure was resolved on the large scale image. However by the large scale, it was not viewable. Located above graphene, large KBr carpets were found. The alkali halide directly interfaced the edges of graphene. These interfaces were smooth. In contrast edges to copper appeared elevated (red arrows).
Two cross-sections for the topography are shown in 3.3 b). In the upper graph the interface of copper and graphene is presented (red cross-section). Directly visible by the corrugation was the Moire structure. The height, referenced to the center of the corrugation, was found to be homogeneous with a value of 455 pm. Within the lower graph the KBr copper interface is shown (orange cross-section). For the large carpets of KBr a height of 160 pm was found, equal to a monolayer. For the KBr edge to the left a height comparable to a second layer was found. In case of the right edge the height was lower. These domains were small and KBr may was more clustered than grown epitaxial. The regions were graphene and KBr interfaced were found to be rough by the presence of many steps. This impeded the measurement of the height of graphene in respect to copper. In addition it was not clear if the KBr carpet continued beyond the interface.
Graphene, KBr and copper were clearly distinguishable in the CPD, presented in figure 3.3 c). The contact potential in respect to copper was about 600 mV for graphene and 1 V for KBr. No gap was visible at the interface of graphene and KBr. Steps were visible in the contact potential of graphene as a reduced contrast. In contrast no steps were resolved in the case of KBr. In addtion the CPD clarified the assignment of the copper regions in the cross-section.
For the determination of the CPD a histogram of the image is shown in figure 3.3 d). The peaks were fitted by Gaussian distributions. In case of graphene a contact potential difference of 579.5 mV in respect to copper and 403 mV in respect to KBr were found. The contact potential difference between KBr and copper was 982.5 mV.
The observation of the Moire super structure was a clear evidence that graphene

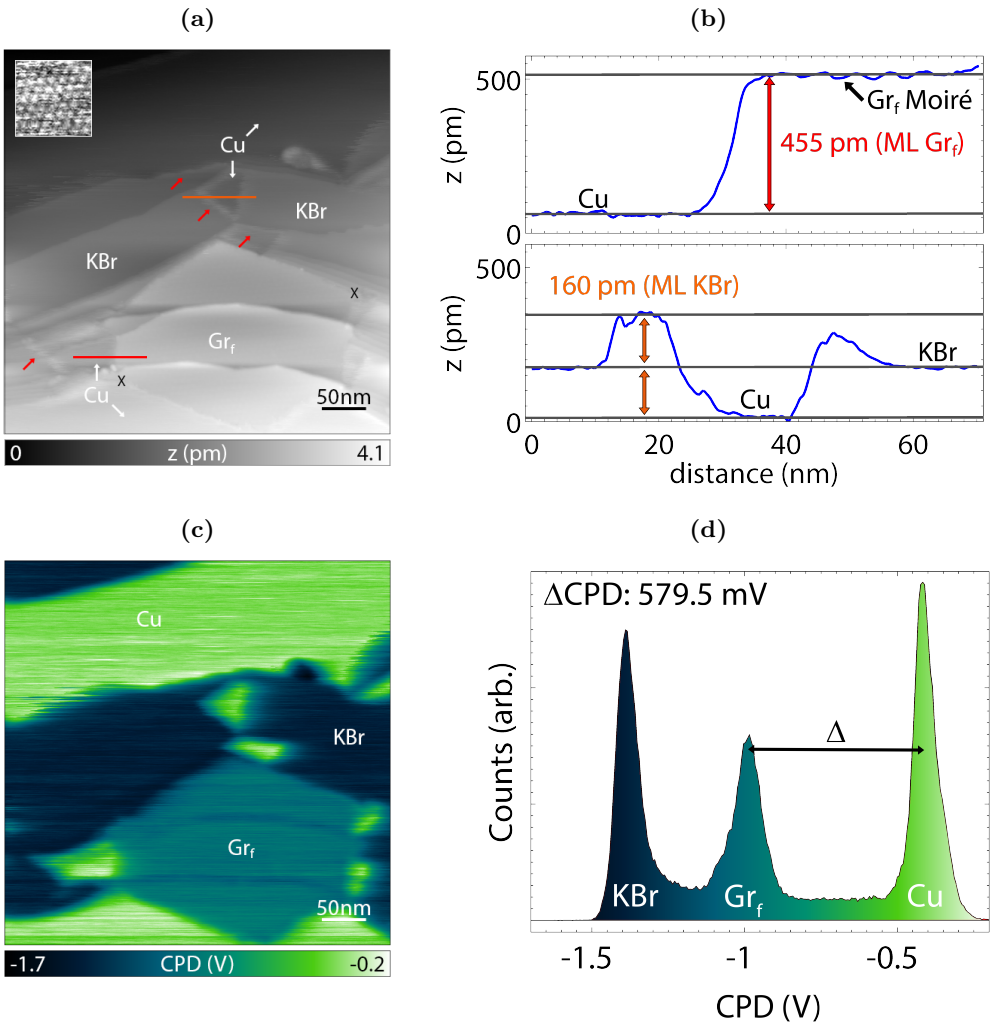

Figure 3.3: Hexagonal graphene flakes on Cu(111) in presence of KBr. Graphene is surrounded by KBr. The work function changed to work function values comparable to graphite. inset 37.4x37.4 nm imaging parameter: 8 nm, k = 30.11 N/m, 170.75 kHz, -8 Hz, 30419; KBr evaporation parameter: 405 C, 0.23 Ang/min, 20min, T 150 C, 5.3e-10 mbar

was not covered by KBr. Further a higher work function would have been expected for a flake covered by the alkali halide. Instead, the work function of graphene was found to be lower in respect to graphene on copper, after the absorption of KBr. By the plate capacitor model, refer to section **??**, the CPD for graphene intercalated by a monolayer of KBr was calculated as 541.0 mV. The calculated Fermi level shift in respect to free standing graphene was calculated as 39.0 meV, the difference between calculated and measured CPD. The perfect agreement between the simple model and the measured CPD were a strong indication that graphene was intercalated by a monolayer of KBr. In addition the interface between graphene and KBr was found to have been smooth in topography and CPD, while it was rough between KBr and copper. This indicated the continuation of KBr underneath the flake, further proving intercalation.
Concluding this section the results for the co-adsorption of KBr were related to those of graphene on copper. Graphene was found to be separated by 455 pm from copper in presence of KBr. The increase of the separation by 115 pm was larger compared to graphene on Cu(111). However, this increase was smaller than the separation of a monolayer of KBr of 160 pm. This pointed to strong changes in the interfaces of graphene and KBr in case of an intercalation. Indeed, a strong shift in the contact potential (work function) of graphene in respect to graphene on copper of 249.4 mV was observed. This value was found to be very similar to the Fermi level shift of graphene on copper of 257.7 mV. In conclusion graphene has been decoupled from copper. The work function was comparable to those of free standing graphene.

3.4 Outcomes

Graphene work function measured by FM-KPFM in very good agreement with calculated values.
Co-adsorption of sodium chloride led to a minor shift in the work function of graphene. Could be attributed to effects at the edge. Expected shift by the calculations for an intercalated layer of sodium chloride instead led to stronger expected shift.
For low coverage potassium bromide stronger change. May not yet intercalated by edge effect as for NaCl. In the case of a larger coverage of potassium bromide the shift was as expected from a calculated layer. The work function was almost as for a free standing layer of graphite. Strong indication for an intercalation. Simple model quite accurate, despite it was referred to the graphene-copper interface.

Island were resolved for NaCl on graphene, in case of KBr no islands observed but moire, if there and moved should be visible by change in CPD and instabilities in topo. Cooperation higher stability of intercalated graphene than free ML of KBr or graphene. bromine to copper underneath.

In cooperation with the group of Prof. Clelia Righi, the stability of KBr intercalated graphene has been investigated by DFT. First preliminary results should be presented here. They found a work of separation for a single layer

of KBr on copper of $0.38\,J/m^2$. The work of separation for graphene was $0.21\,J/m^2$ at an equilibrium distance of 320 pm. The adsorption of KBr was much stronger than of graphene, by $0.17\,J/m^2$. This underlines also the weak binding of graphene to the substrate. A strong interaction for the bromine with the copper substrate was found, inducing a small buckling. They then compared the stability of graphene intercalated by a layer of KBr to graphene on copper with a layer of KBr on top. The intercalated structure was the most stable configuration. The difference between these two configuration was found as $0.29\,J/m^2$, even higher than the difference for the adsorption of graphene or KBr. In conclusion the intercalation was not only by the adsorption of KBr but by a cooperative effect between all three materials.

Chapter 4

Moire structure of graphene on Cu(111)

4.1 High resolution nc-AFM and FM-KPFM measurements

Different Moire pattern were observed throughout this work. The Moire with 2 nm periodicity, one of the most abundant structures observed by STM in the literature, [1] was measured by bi-modal nc-AFM and simultaneous FM-KPFM in high resolution.

4.1.1 2nm Moire

The Moire super structure was clearly visible in the topography shown in figure 5.1 a). Faint atomic resolution was also present, superimposed by noise especially in the valleys. Simultaneous measurement of atomic and Moire contrast was difficult to achieve in the topgraphy. As in the case of Pt(111), graphene on Cu(111) was expected to be bound weakly to the substrate. [7] In the platinum case graphene was elastically deformed by the interaction with the tip. [26] A deformation could explain the difficulty to measure both structures in the topography.
Strong dissipation was found, visible in figure 5.1 b), supporting the deformation hypothesis. The contrast was inverted in respect to the topography with stronger dissipation in the valley. The origin of the dissipation was the adhesion between graphene and the tip, locally detaching graphene from the substrate. [26] The stronger adhesion in the valley implied a stronger binding between graphene and the metal substrate within this areas.
A weak Moire contrast became also visible in the LCPD, following the contrast of the topography. The valleys were found to have a lower contact potential. As discussed in chapter 2.1.3 the origin of a local contact potential is difficult to deduce. In the case of graphene two effects could explain the observed local contact potential difference. First the moire reflected the deviations in the local chemical potential between graphene and the substrate. [26] These differences can be measured by FM-KPFM. [54] Second a deformation can

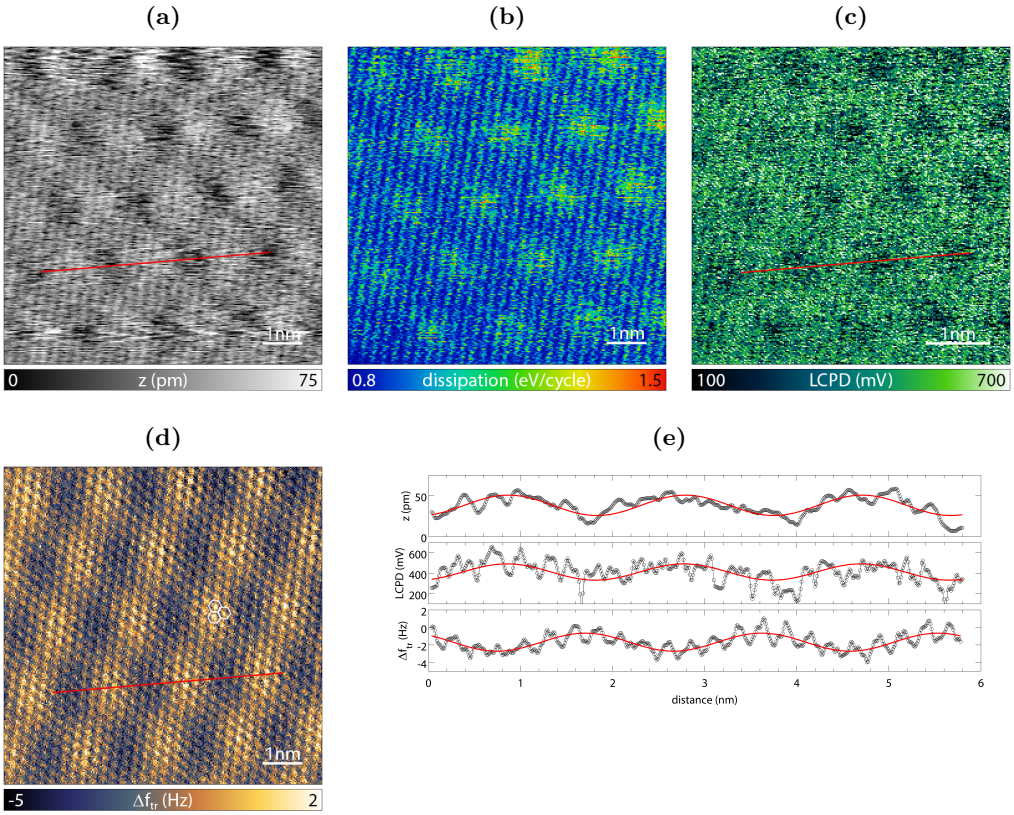

Figure 4.1: Moiré structure and atomic resolution of the most abundant Moiré structure of graphene on Cu(111). Topography a) Large dissipation by adhesion in b), stronger on the valley. Moire resolved in the LCPD in c) Torsional frequency shift inverted d). Cross sections along the red line shown in e). White hexagons in d) marked the atomic lattice with the atoms positioned at the intersections. Periodicity for all 1.91 nm. Imaging parameter: $\Delta f_{2nd} = -360Hz, A_{2nd} = 400pm, k_{2nd} = 6.94kN/m, Q_{2nd} = 12'982, A_{tr} = 55pm, k_{tr} =, Q_{tr} = 74'055$.

amplify the LCPD-contrast in FM-KPFM, even for small ionic displacements in alkali halides. [55].
Best resolution was obtained for the torsional frequency shift, shown in figure 5.1 d). The contrast for the Moire in respect to the topography was inverted, comparable to the dissipation for the 2nd flexural mode. A hill (valley) in topgraphy was observed as a valley (hill) in the torsional signal. In addition the shift appeared not perfectly inverted, but shifted. As a consequence the torsional frequency shift was not directly related to the observed dissipation. However, the torsional frequency shift was time-averaged over many oscillations cycles of the first PLL, and directly sensed the deformed topography. No dissipation was present for the torsional mode (not shown here). The atomic scale contrast in the torsional frequency shift could be directly inferred from highly oriented pyrolitic graphite. [50]
Cross section were taken for a more detailed analysis, infer to the red line. To

obtain the periodicity and height a Fourier analysis was carried out, visible as red curves in 5.1 e). All super structures had a periodicity of 1.92 nm, comparable to the 2 nm by Gao *et al.* The height of the Moire was 24.9 pm and the local contact potential modulated by 159.1 mV. Partially the atomic scale resolution in topography and LCPD was visible.// The LCPD was shifted by -22.29 pm in respect to the topography, or phase shifted by -2.1 degree.
For the torsional frequency shift it became clearly visible that the cross sections followed the moire despite the atomic structure. However, atomic periodicity was clearly visible. The modulation for the Moire was 2.1 Hz within the torsional shift, comparable to the modulation for the atomic contrast. The super structure was shifted by 834.1 pm or 78.6 degree. The profile clarified the shift for the inversion.
The tip used to measure the 2 nm Moire pattern was crashed inbetween the measurments on the 2 nm Moire, refer to 4.1.1 . The CPD differed by 800 mV after the crash, the contact potential difference between graphene and copper. However, stable imaging was possible and the scanning site was changed to a different flake with a periodicity of the super structure of 3 nm. The spectroscopic experiments in the following sections were carried out on this flake, presented in the following sections.

4.1.2 3 nm Moire and setup of spectroscopies

Figure 4.2 gave an overview of the bias sweep spectroscopy experiments. The torsional frequency shift for the site before and after four consecutive spectroscopic can be seen in a) and c) respectively. The positions for the tracking and the spectroscopy sites can be taken by the circle and the markers respectively. To account for the drift the markers in a) have been rotated by 15 degrees in c). The topography is shown in b), related to the lower half of the torsional images. In both images faint atomic contrast was visible in the lower part, despite strong noise. While in the torsional frequency shift strong changes were observable after the experiments, these were not visible in the topography, refer to lower image of b). The tracking position and of the experiment shifted slightly by increasing drift. After the spectroscopic experiments, between experiment and tracking site a sudden large negative shift was found, accompanied by noise features.
In the following sections the properties of the Moiré properties were investigated by bias distance spectroscopy experiments on hill and valley site respectively. The spectroscopy raw-data has been treated and analyzed as laid out in detail in chapter 2.1.4.

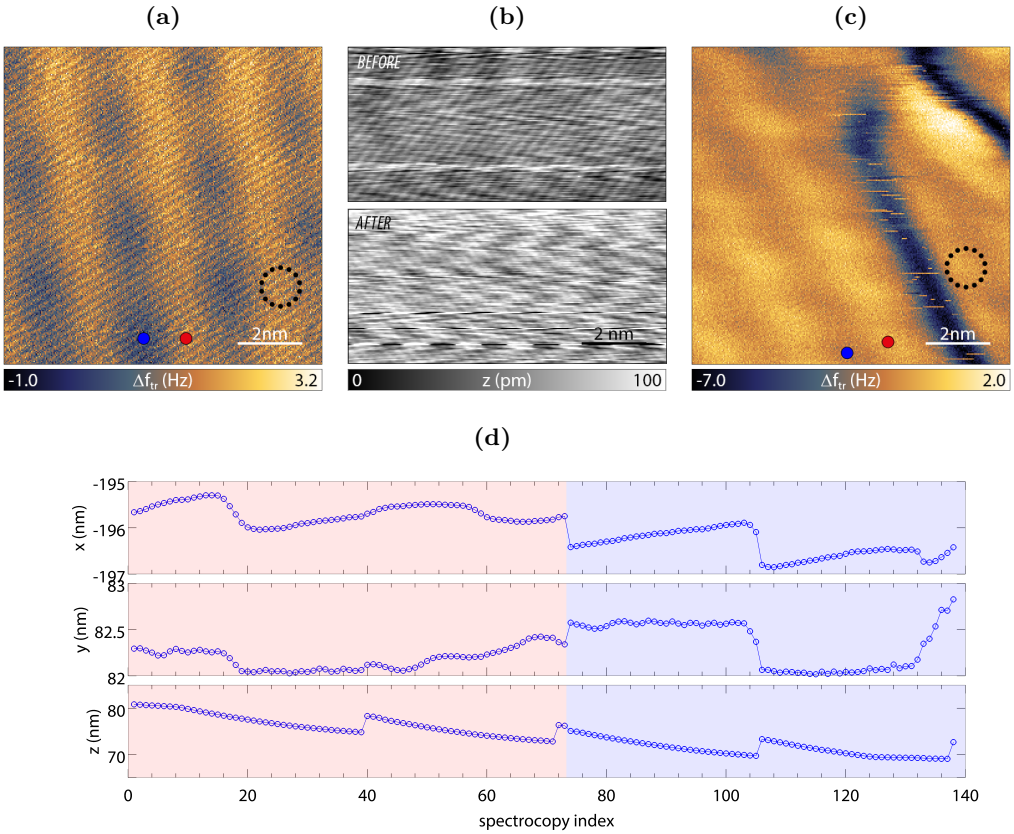

Figure 4.2: Measurement conditions for the spectroscopic experiments on the 3 nm Moiré. Atom tracking has been employed on the torsional frequency shift, shown before a) and after the experiment c). Position of the tip shown for all spectroscopy data in d). Two subsequent measurements on each site on a valley (red) and hill (blue), marked by dots. Tracking position visible by circle. A: 400 pm, k 6.94kN/m, Q 12'982. $V_{bias} = 205mV, \Delta f_{2nd} = -375Hz$

4.2 bias sweep spectroscopy on a hill

Fitting applied to all conservative contributions

The goodness of the fit by the adjusted root-mean squared error was 0.9993 for both forward and backward direction respectively. The frequency shift was subtracted by the fit curve for the Morse (Van der Waals) contribution. The residual curve then was compared to the fit curve of the Van der Waals (Morse) contribution. The tail with a positive slope below 0.55 nm had no influence as this part was excluded by the fitting. For the residual Van der Waals frequency shift in figure 4.7 c) the slope of the fit followed the data. However already at long-range distances a slight offset was found. The characteristics observed for the data were replicated, with the jump being -12.8 Hz. A Hamaker constant of 6.53 eV (6.59 eV) was found.
A comparable outcome was found for the the Morse contribution, shown in c). For the short range forces an interaction length of 0.28 (0.27) nm was found

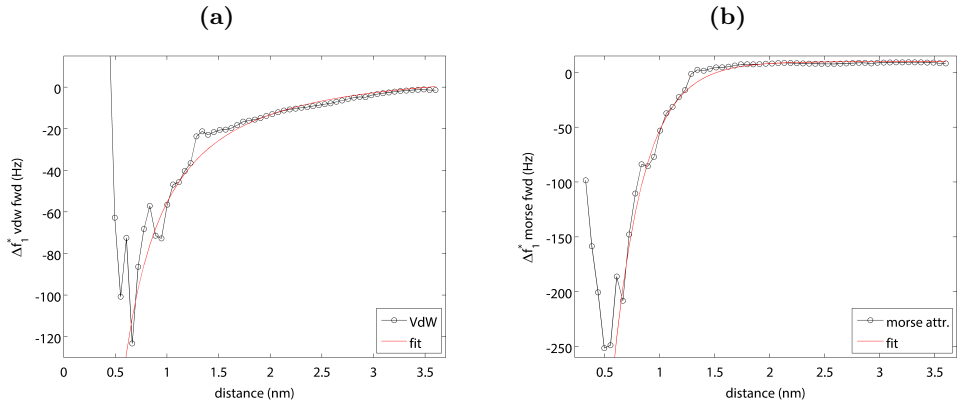

Figure 4.3: Results for the fitting of the frequency shift for a hill site on $Gr/Cu(111)$ along relative distance and applied bias, note that the recalculated map in a) appeared different by the offset that has not been subtracted. Overview of the data and individual contributions along the compensated electrostatic force in b). Residual frequency shift compared to the fit contribution for Van der Waals c) and Morse d) contribution showing strong non-conservative interactions.

with the interaction minimum at 0.60 (0.59) nm. The drop at the onset of the short range interaction was slightly lower by -14.7 Hz. The sum of the frequency drop for both residuals was -9.9 Hz larger than those in the total fit, the value for the offset, that had to be taken into account for the residual of the Morse contribution. An interaction energy of 1.81 eV (1.86 eV) was found.
The contact potential difference by the fit model was 190 mV (172 mV).[1] As a comparison the Hamaker constant for an oxide terminated tip and graphite in UHV has been calculated as 12e-20 J, [61] that is around 0.75 eV. This carbon nano tube arrays on glass. 6e-20 J or 0.37 eV respectivly. [62] In perspective to these values the measured Van der Waals interaction presumably was by strong adhesion. The small tip radius calculated by the model of 1.78 nm (1.76 nm) supported this, as a sharp and more flexible tip causes stronger adhesion. [63] In addition, the deviations of the data from the conservative model and the differences in forward and backward frequency shift supposed the presence of non-conservative interactions that can be related to adhesion. The deviations of the residual frequency shift curves from the conservative force model in ? can be attributed to the dissipation by Van der Waals interaction.

4.2.1 Dissipation and non-contact friction

In figure 4.4 the dissipation and the related non-contact friction are shown, revealing large dissipative processes in the tip-sample junction. Analogue to the frequency shift different regions of dissipation were identified. Above a relative distance of 1.46 nm, visible by the dark blue color, dissipation was governed

[1] The values in parentheses are related to results from the fitting of the backward sweep.

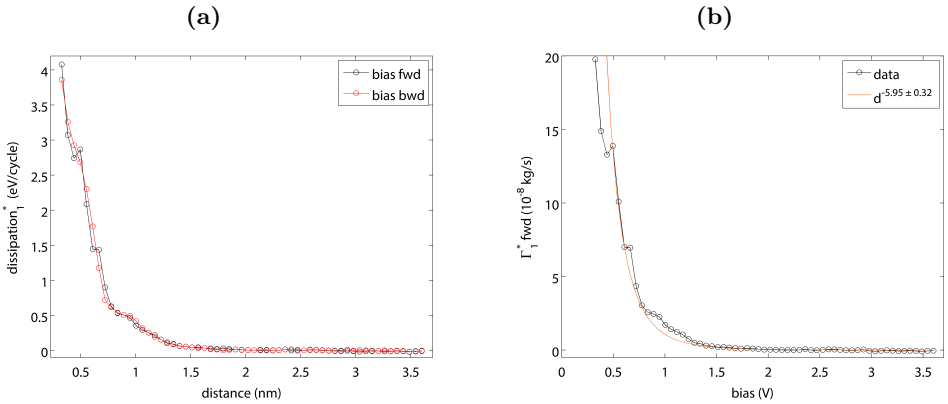

Figure 4.4: Energy dissipated per oscillation cycle an non-contact friction coefficient Γ for a hill site on $Gr/Cu(111)$.

by joule dissipation. Along the compensated electrostatic force, shown in b), no apparent dissipation was found in this region. A noticeable change in dissipation became visible at 1.46 nm relative distance with a slow increase in the dissipated energy by 0.5 eV per oscillation cycle at 0.83 nm. Hysteresis became also apparent in the dissipation. The hysteresis found within the dissipation that coincided with those observed in the frequency shift, could be attributed to adhesion.

Then strong increase set in at 0.78 nm with a change in slope at 0.44 nm with a dissipation of 2.93 eV per cylcle. From the onset to change a hysteresis like feature. Till 0.61 nm untypical as backward lower than forward, distance where the minimum in the Morse potential was found.

The dissipation was converted to non-contact friction coefficient. A distance dependence proportional to the power of minus six was found. Phononic friction by the Van der Waals interaction between the tip and the sample.

Joule-type dissipation by moving mirror charges through the tip oscillation. Wiggles by deformation of tip and sample in the force curve. Enhanced detection sensitivity for dissipation energy by smaller amplitude . Sharp tip less electrostatic background, smaller force

Atomic-scale processes dominate dissipation. [64] Hysteresis by deformation of tip and sample in proximity.Aat very close approach onset of instabilities inherent to DFM, dynamic force affected by dissipative tip-sample interaction. NaCl-tip on NaCL, adhesion of chains responsible for dissipation, longer chains result in more dissipation,. Chain most probably from tip cluster. [2] Tip approached the surface close to or into soft contact. On retract adhesion resulted in local deformation of graphene visible as deflection in the cantilever. The closer the approach, the less soft contact was engaged. Ultimately disturbing the self-oscillation, visible as oscillations in amplitude and phase. Increasing strength and low amplitude impeded stabilization, resulting

[2] Do we see higher dissipation in case of larger deformation radius?

in an increasing magnitude of disturbances. Alkali halides 0.5 eV per oscillation cycle, [64] we measured 4 eV. Contrary to alkali halides the movement of single atoms is far more constraint in graphene. The strength of adhesion should reflect the environment of the atoms attracted towards the tip, its bond length and bonding strength. The magnitude of corrugation by the lattice mismatch will influence the resistance to deformation, like the Young modulus, and pretension of structure.

The amount of dissipation by the deformation is directly proportional to the relaxation time. [65] In addition larger displacements of surface atoms yield larger dissipation. [64]. Thus the maximum magnitude of the averaged dissipation by the deformation was determined by the relaxation time varied by the phase lag.
Dissipation channel on graphite governed by friction processes. [66] A sharper and more flexible tip causes stronger adhesion. [63] Below In the case of NaCl investigated with a NaCl tip, a strong increase in dissipation, as observed at 0.83 nm, coincided with the formation of contact. [64]

4.2.2 Along compensated electrostatic forces

For the frequency shift, shown in figure 4.5, three regions with hysteresis were found, that were attributed to adhesion. Adhesion hysteresis 1.12 to 0.89 nm, 0.78 to 0.55 nm and with different slope continued to 0.35

backward potential always lower 20 mV compared to forward, both declined till the onset of the short-range forces. Within the range of error. However at the second peak and in decline equal slope between 0.84 and 0.50 nm while value of backward was always slightly lower. Direct relation of the features of the electrostatic potential to the dissipation regimes. Linear increase from 0.83 nm with 271.8 mV to 415.9 mV at 0.66 nm The first, broad maximum was found at a relative distance of 1.12 nm for a bias of 0.31 V , then 0.66 nm with 0.432 V, dark blue upper rim, down to 0.38 nm. 134.1 (152.8) mV at 0.33 nm

Hysteresis between -100 and -200 Hz

The time averaged deflection followed the slope of the frequency shift. The maximum deflection of 0.17 pm was 0.04 % in respect to the amplitude of 400 pm. The frequency shift for the time-averaged deflection, further referred to as deflected frequency shift, was obtain by subtraction of the raw-data by the data that was shifted in respect to the time-averaged deflection. Both had to be interpolated to allow for the direct subtraction on the same scale. 1.29 nm to 0.83 nm hysteresis Hysteresis in deflected frequency shift reflected those of the frequency shift and dissipation. Also were the amplitude started to change.
Correlation of changes in the dissipation and the frequency shift and hence the time averaged deflection. Also the deflected frequency shift related to the dissipation branch between 0.89 and 0.44 nm. Step at 0.61 nm at the node in the dissipation. Within this region strongest change in the deflection and the step the minimum in the shift. The interaction observed in the deflection

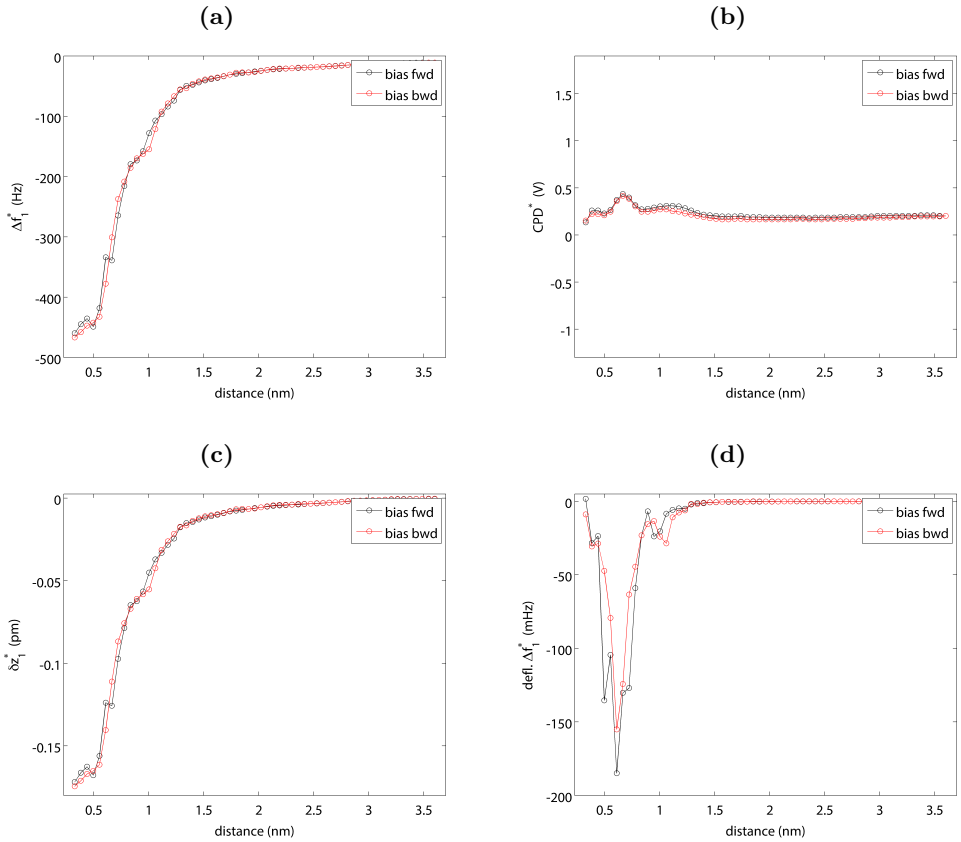

Figure 4.5: Frequency shift response for a hill site on $Gr/Cu(111)$. Raw data of forward swept curves (from positive to negative voltages) in a). Time averaged deflection along the CPD b). Data shifted by time averaged deflection. Points taken from interpolation with one additional point in between the data points.

appeared to be directly related to the processes. Forward features between -100 and 150 mHz above and below the minimum. Not seen on backward, forward also wider than backward. Change in dissipation slope at 0.44 nm also vissible as a step like feature.

For the conservative part of the forces. Hysteresis around 1 nm, wiggle, the minimum detected normal force of-6.5 nN. For the time-averaged force -2.5 pN. Calculated by the force constant of the first mode, may had to be related to the contact stiffness.

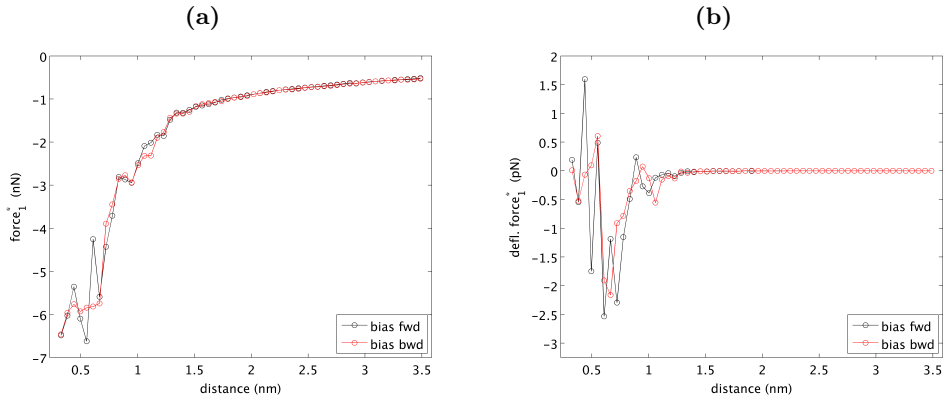

Figure 4.6: Conservative forces for a hill site on $Gr/Cu(111)$, derived by the Sader-Jarvis method for the frequency shift a) and the deflected frequency shift b).

4.3 bias sweep spectroscopy on valley

4.3.1 Fitting applied to all conservative contributions

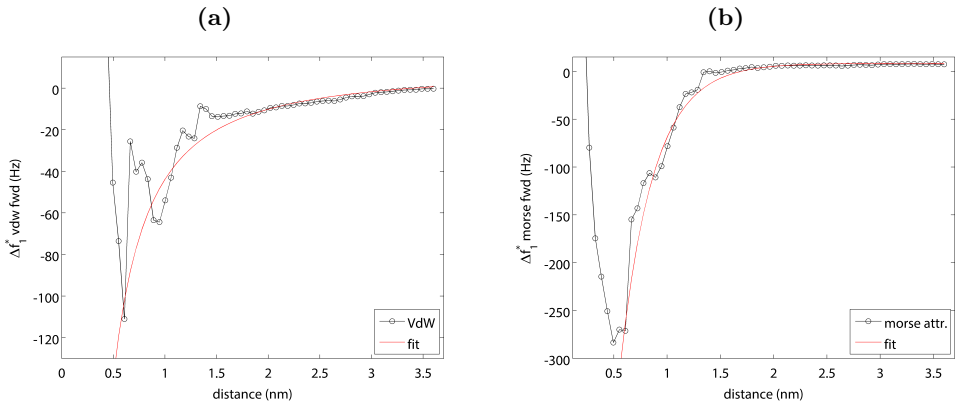

Figure 4.7: Fitting of the frequency shift response for a valley site on $Gr/Cu(111)$ along both dimensions, note that the map appears different by the offset that has not been subtracted.

In the fitting to all conservative contributions, the change of the tip position became not visible in the recalculated frequency shift map, shown in The goodness of the fit did not differ from those of the hill with values of 0.9989 (0.9988).
For the curves along the compensated electrostatic force, shown in figure 4.7.b), a comparable characteristic to the hill was found with strong deviations from the conservative model by non-conservative contributions. As for the hill a drop in the frequency was observed. In case of the valley it was found at closer distance of 1.34 nm.

The minimum frequency shift of the Van der Waals residual was found at higher slightly, -5 Hz, higher frequency shifts. This was in line with a Hamaker constant of 5.30 (5.09) eV, lower by 1.23 (1.5) eV compared to the hill. As expected the Van der Waals interaction, and as a consequence the adhesion was lower on the valley. The atoms of the valley were closer to the surface and a stronger interaction to the substrate was expected, that should have been reflected by a weaker interaction with the tip.
For the residual frequency shift of the Morse interaction a stronger interaction was found in the valley by 2.22 (2.17) eV. The interaction length 0.31 (0.31) nm was also slightly larger, while the minimum was at a comparable distance of 0.58 (0.58) nm. This was contrary to the finding from the Van der Waals interaction. It also clearly showed that the interaction was dominated by the adhesion in the Van der Waals interaction.
The contact potential difference with a value of 228.9 (210.2) mV. It was still larger than the value found for the hill.

4.3.2 Dissipation and non-contact friction

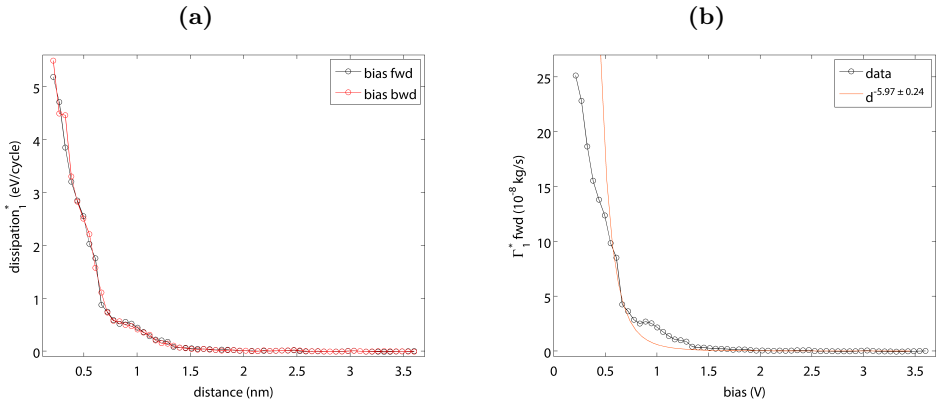

Figure 4.8: Energy dissipated per oscillation cycle an non-contact friction Γ for a valley site on $Gr/Cu(111)$.

For the valley the three dissipation regimes were also found within the same range. Shown in figure 4.8, at larger distance Joule type dissipation was found. As on the hill between 1.46 and 0.78 nm a slow increas in dissipation by 0.5 eV per cylce was present. The strong dissipation that set in was different compared to the hill. A hysteresis was very weak, down to a relative distance of 0.38 nm. Analogue to the hill a node 0.61 nm, close to the minimum of the Morse interaction, was found. A larger hysteresis was visible from 0.38 to 0.27 nm. At 0.33 nm, the closest analyzed distance for the hill, the value for the dissipation was found as 3.85 (4.46) eV per cycle. In case of the forward sweep the found value was lower than on those found for the hill. In addition the slope exhibited no clear linearity below distance of the Morse minimum below 0.55 nm.
In case of the non-contact friction, only between 0.78 and 0.61 nm a reasonable

fitting for a phononic contribution was possible.

4.3.3 Along compensated electrostatic forces

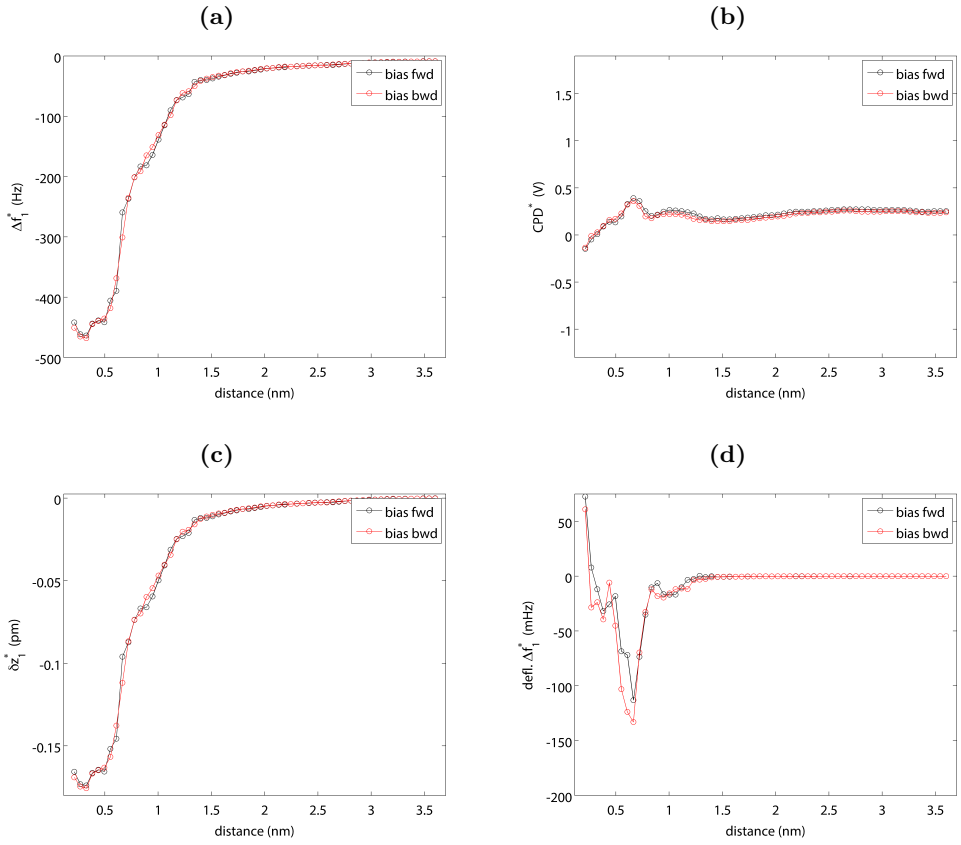

Figure 4.9: Along compensated electrostatic forces for a valley site on $Gr/Cu(111)$.

Forward and backward differed by 20 mV. Change in tip position linear decrease from 269.7 (259.3) to 245.8 (240.5) mV. Close to the noise limit. More significant change in the following when the position appeared stable again. Reduction to 165.4 (146.6) mV at 1.57 nm. Increased to a first maximum at 1 nm t o 265.5 (221.7) mV, comparable in forward to the CPD value. Position almost as for a hill site. 0.78 nm sharp increase from 253 (196.7) mV to 390.8 (359.5) mV at 0.66 nm, same position as on the hill.137.8 (162.8) Direct decrease afterwards with hysteresis between 0.55 and 0.44 nm. 8.8 (27.6) mV at 0.33 nm, about 125 mV lower than on the hill. Same distance to the peak.

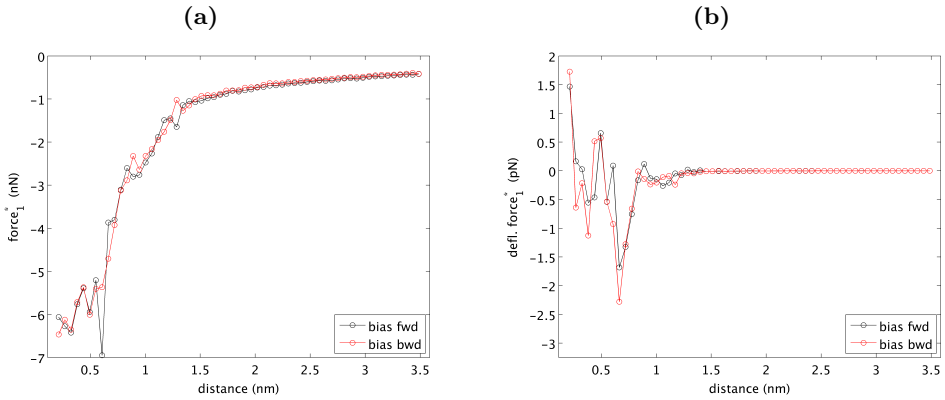

Figure 4.10: Forces by Sader-Jarvis conversion for a valley site on $Gr/Cu(111)$. From frequency shift a), and from deflected shift b).

4.4 Outcomes

The mechanic and electronic properties of the Moiré pattern of graphene on Cu(111) have been investigated throughout this chapter. Graphene was elastically deformed by adhesion to the tip, visible by a strong dissipation. The measured dissipation in the valley was larger than hill for the 2 nm Moire. The same behavior was found in the spectroscopic measurements for the 3 nm Moire. Part of the dissipation could be attributed to non-contact friction by excitation of phonons in the sample. Within this regime the time-averaged deflection was found. Stronger dissipation occurred when local contact formation was present. While the overall interaction was still attractive, short-range forces were already repulsive. Contact resonance as the deformation followed the tip oscillation. These manifested in oscillations in the amplitude, followed by phase, frequency shift and dissipation. These strong non-conservative interactions were also visible as hysteresis like features in frequency shift and dissipation. Strong deviation from the conservative forces law were unraveled by fitting.

Acquired data was fitted in the range of attractive force along the distance and the swept bias. Direct access to quantities as the CPD, an offset for the whole data and the estimated tip radius. Better prediction of the experiment as validity was proven along both dimensions of the experiment. The tip was most probably modified by small graphitic molecules. However, measurement conditions were stable and a comparison of the found tip-sample interaction with the literature values for interaction silicon and copper to a small flake, indicated a stronger binding to the tip. As the z-position was stable until the last of four spectroscopic experiments, the change visible in the torsional frequency shift map after the experiments most probably occurred not before this disturbance.

For the spectroscopies, at long-range distances, the CPD for the valley was surprisingly higher by 50 mV, but also close to the detection limit in FM-KPFM. At closer distance however, the LCPD for a hill of the 3 nm Moire

was 125 mV higher compared to those of the valley. This finding gave a strong indication that the measured LCPD of 159.1 mV for the 2 nm Moire was a real property.
It was found that the atomic scale contrast formation in the torsional frequency shift was different for graphene compared to graphite. Different binding and the deformation by the Moire were identified as the main difference. For the super structure an inversion in respect to the topography was found. A detailed description of the contrast formation was given in section **??**. The contrast formation was found to be sensitive to the size of the super structure. Further measurements on small and larger Moire are necessary to clarify this sensitivity.
The found CPD value indicated that the tip had a comparable work function by the presence of graphitic material at the tip.[3]
The functionalization of the tip by graphitic compounds was supported by interaction energy . The value was found inbetween those of the cohesive energies between polyaromatic hydrocarbons that were of the size of seven to ten fused benzene rings and graphite. [67] The interaction energy and the found CPD gave a strong implication that a small graphene flake was picked up by the tip. This became even more reasonable as the tip has been crashed earlier on another graphene flake changing the cpd by the magnitude of the contact potential difference between graphene and copper. The pick up of carbonaceous material raised the question on the stability of the measurements.
The imaging conditions prior the spectroscopic experiment appeared stable, as no further tip crashes occurred and reproducible atomic resolution was achieved. The stability of the measurement conditions was further supported by the overall stability of the tracking position over more than 100 subsequent spectroscopies, refer to figure 4.2. From the now known distance dependence, the discontinuities in the tracking during the experiments can be reevaluated. For the hill site these occurred not earlier than in the strong attractive region below 0.73 nm for the second data set. For the data discussed in this section even at distances below the interaction minimum. In addition stable measurement conditions were still achieved in the second data set, carried out after the measurement discussed herein. Even if the tip was functionalized by carbon material the instabilities were only observed at the limit of the non-contact regime and presumably related to the tip-sample interaction.
A careful estimation on the strength of the attachment of a small flake to the tip was made by considereing the interaction of carbon and silicon in silicon carbide. The cohesive energy in silicon carbide was calculated as 6.3 eV. [68] Indeed one would expect a different interaction for the sp2 hybridized carbon atoms in graphene. However in case of small, molecular aromatic carbons of comparable size as in the work of Zacharia *et al.*, either dangling or hydrogen terminated bonds can be expected, that readily can form chemical bonds. Thus the attachment of a flake was assumed to be stronger than the found short range interaction of the tip-sample junction. To complete the discurs on

[3] In experiments for a Cu(111)-surface measured by a fresh prepared silicon tip the contact potential of copper was found around zero Volt. Graphene flakes than had a contact potential difference of about -830 mV in respect to copper, for details see **??**

the stability of the tip the attachment of the graphitic material to a copper tip was considered, even if unlikely by the found contact potential difference. A silicon tip can also be modified by a copper cluster, effectively becoming a copper tip. The interaction bewteen a copper tip and a graphitic flake still would have been twice as strong as the interaction energy at the tip-sample junction, as copper is bound to graphite by 4 eV. [**?**]

Chapter 5

Moire structure of graphene on Cu(111) after evaporation of KBr

In 3.3 it was found that a Moire structures were present when graphene was intercalated by KBr.
First the structure of the Moire will be presented. Bias distance spectroscopies were measured on this Moire structure. In the following sections the properties of hill and valley will be presented. First the frequency shift will be discussed, a detailed look at the components of the Van der Waals and the Morse contribution. From the frequency shift the force was derived. Also from analysis the contact potential. Then the dissipation will be discussed and finally the time-averaged deflection.

5.1 Moire on KBr-intercalated grapene

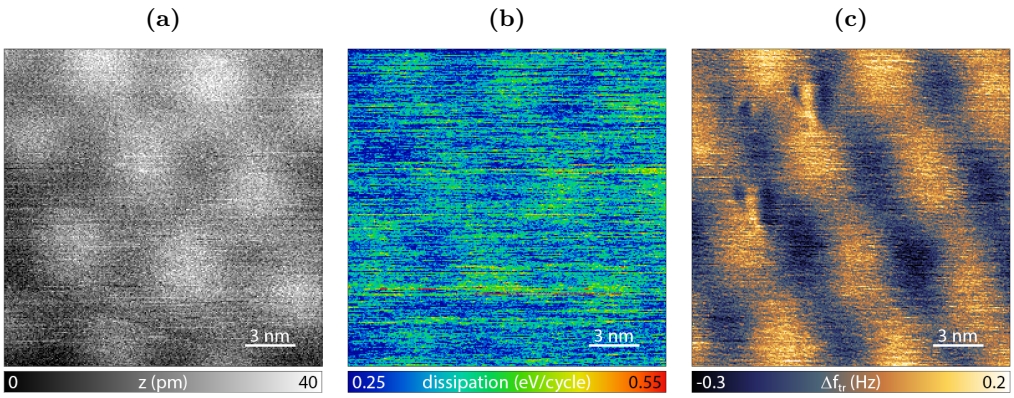

Figure 5.1: Moiré structure and atomic resolution of the Moiré structure, observed for graphene on Cu(111) with KBr. $\Delta f_{1st} = -114Hz, f_{1st} = 170.775kHz, A_{1st} = 8nm, k_{1st} = 30.13N/m, Q_{1st} = 30855, A_{tr} = 200pm, Q_{tr} = 56'537$.

Larger Moire pattern. Elastic deformation, visible as dissipation. Valley stronger dissipation. Torsional shifted but not inverted, in contrast to graphene on copper. Appeared rotated, force gradient along x and not y. Weak contrast, no atomic resolution, more difficult to achieve by the larger amplitude of 200 pm in the torsional. Deformation visible in upper left area of the torsional frequency shift. Not visible in the topography. High sensitivity of the torsional mode.
In the following the results from the spectroscopy will be discussed.

5.2 Conservative contributions

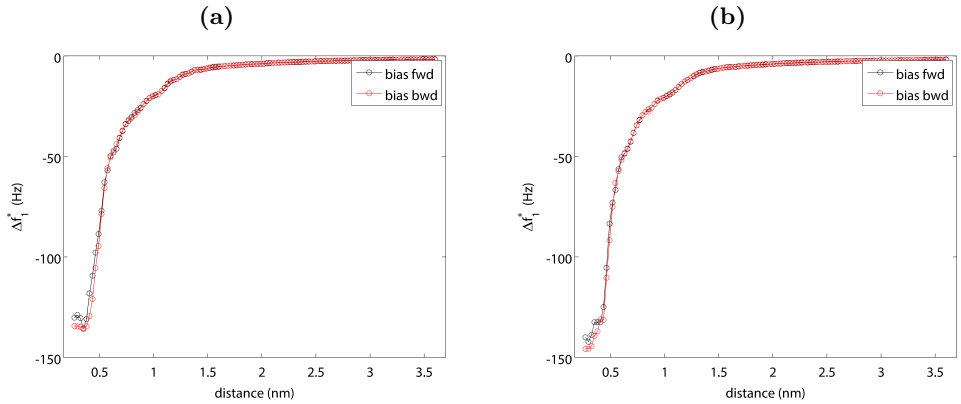

Figure 5.2: Frequency shift response for $Gr/KBrCu(111)$. Hill a), valley b).

The frequency shift for the Moire super structure of the KBr-intercalated graphene is shown in figure 5.2. With the onset of the short-range interaction, close to 1.5 nm for the hill and 1.4 nm for the valley, disturbances became apparent. Wiggles were visible around 1.1 and 1 nm relative distance for hill and valley respectively. Another wiggle in the frequency shift for hill and valley was found at 0.6 and 0.5 nm close to -50 Hz.
This wiggle was directly followed by a change in the gradient with a strong slope. While forward and backward were identical for the valley within the region of the slope a hysteresis was found for the hill, starting at 0.5 nm. On the hill the minimum was reached at 0.4 nm with a minimum frequency shift of -135 Hz and a plateau with a second, stronger hysteresis was found. A change was also found for the valley at -135 Hz, that were measured at a relative distance of 0.45 nm. The slope became weaker and a hysteresis became apparent. The minimum detected frequency shift on the valley was reached at 0.3 nm close to -150 Hz. The wiggles and the hysteresis were first indications of non-conservative interactions.
To obtain a more detailed insight into these interactions, the frequency shift from the Van der Waals interaction was extracted as described in .

Strong deviations were found in the Van der Waals interaction from the conservative model, refer to figure 5.3. Between the position of the two wiggles described for the frequency shift, a plateau was found. Below 0.5 nm a better agreement of data and fit was found for the hill. Note, that the strong increase below the minimum was due to the neglect of repulsive contributions by the Morse potential. With -48.5 Hz the interaction was found to be stronger on the valley, compared to the minimum shift of -40 Hz found for the hill. In agreement with this finding a larger Hamaker constant of 7.43 eV was obtained for the valley, as compared to 6.75 eV for the hill.
Analogue to the Van der Waals contribution the Morse contribution was derived according to 5.2.

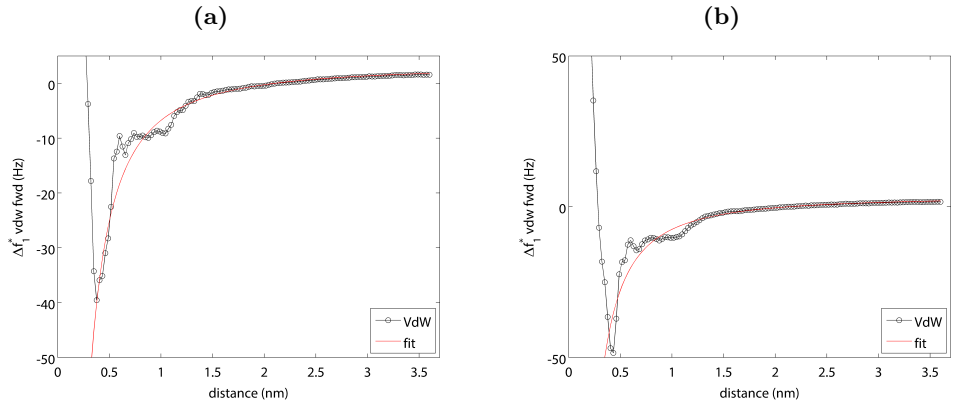

Figure 5.3: Van der Waals residual on graphene on Cu(111) with co-adsorbed KBr. Hill a), valley b).

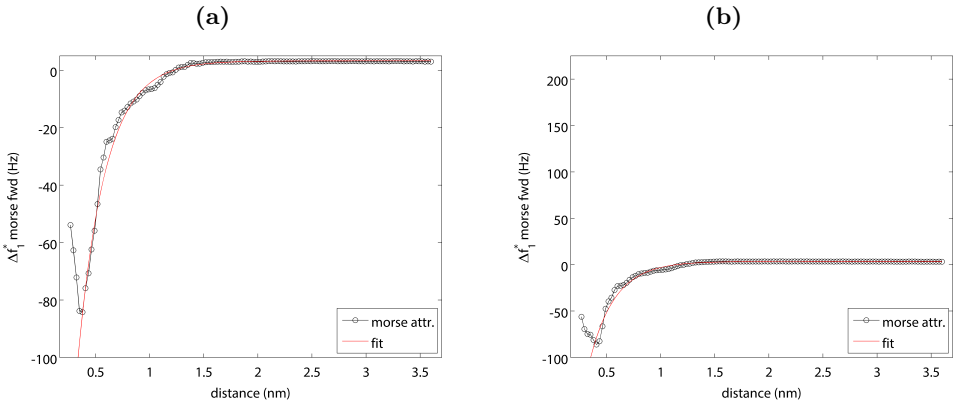

Figure 5.4: Morse residual on graphene on Cu(111) with co-adsorbed KBr. Hill a), valley b).

In figure 5.4 the Morse residual is presented. The agreement between fit and model was better than for the Van der Waals residual. The wiggles were also present for the attractive Morse interaction. However the deviations from the model were weaker and no plateau was found. A better agreement of the frequency shift with the model was found for the hill. The interaction potential of both sites was identical by 1.84 eV for hill and 1.85 eV for valley respectively. Also the minimum of the Morse contribution was identical with 0.31 nm. In case of the valley a small error may caused the deviation at lower distances, as the non conservative contributions complicated the fitting. Both sites were distinguishable by the interaction length of the short-range potential by 0.256 nm on the hill and 0.23 nm on the valley. The value from the hill was comparable to the unit cell length in graphene.
From the analysis as described in 5.2, the tip radius and the CPD were obtained. Both quantities were indistinguishable for hill and valley. The radius of the tip was found to be 0.63 nm and the CPD -1.220 V.

The analysis of the frequency shift will be continued with the conversion of the conservative force by means of the Sader-Jarvis method, refer to 2.1.4.

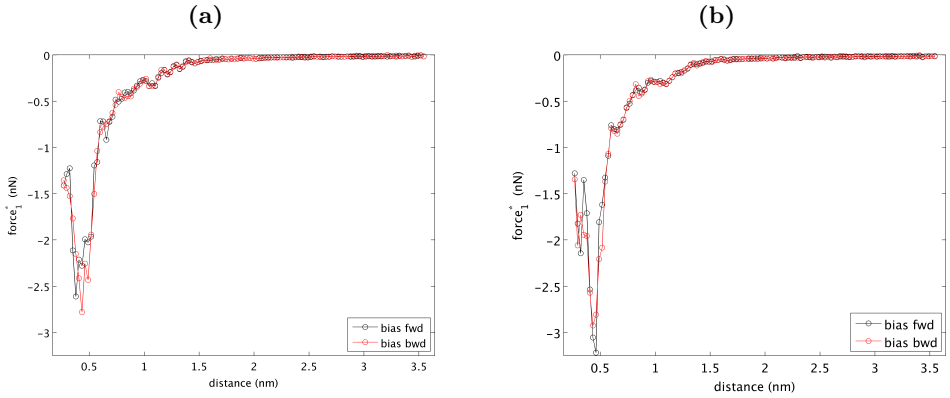

Figure 5.5: Sader-Jarvis of frequency shift for Gr/KBr/Cu. Hill a), valley b).

Saw-tooth like pattern were visible in the region were the wiggles in the frequency shift and the plateau in the Van der Waals shift were found, as visible from figure 5.5. These were more prominent for the hill. Analogue to the frequency shift regions of hysteresis were found. For the valley these were in the region of the strong gradient between 0.7 and 0.5 nm relative distance and in the repulsive regime. On the hill the hysteresis was found in the minimum of the force. For the hill the width around the minimum was broader and the minimum force was - 2.75 nN. The sharper minimum of the valley had a minimum force of -3.25 nN and was more attractive by 0.5 nN. The last quantity described in this section will be the electrostatic potential along the compensated electrostatic force.

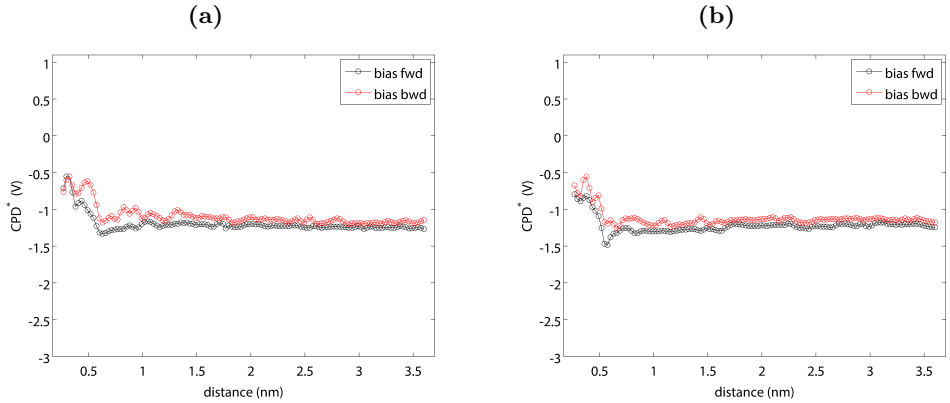

Figure 5.6: CPD on $Gr/KBrCu(111)$. Hill a), valley b).

The potentials, shown in figure 5.6, were equal at long-range distances. At 1.1 nm on the hill and 0.75 nm on the valley a bump was visible, followed by a decrease in the potential. For the hill a minimum of -1.4 V was found

at a distance of 65 nm. The minimum of -1.5 for the valley was found at 0.6 nm. The decrease and the magnitude of the minimum values were stronger for the valley. Directly at the minimum the second wiggle was observed in the frequency shift and the strong decrease set in, in the following the potential started to increase. Backward compensated electrostatic potentials were found to be always higher than those of the forward sweep.
As closing remarks, the highlights of this section shall be discussed. On the Moire of KBr-interacalated graphene strong ,non-conservative processes were found. These were dominantly present in the Van der Waals interaction. In addition, this interaction was very strong, as indicated by the found Hamaker constants. In general the interaction on the valley was stronger than on the hill.
In 5.1 dissipation was found to be present when the Moire structure was resolved. This was a strong evidence of a deformation by adhesion of graphene. [26] The herein found hysteresis in frequency shift and derived force then can be attributed to adhesion. The role of dissipation in the spectroscopic experiments will be discussed in detail in the following section.

5.3 Dissipation and non-contact friction

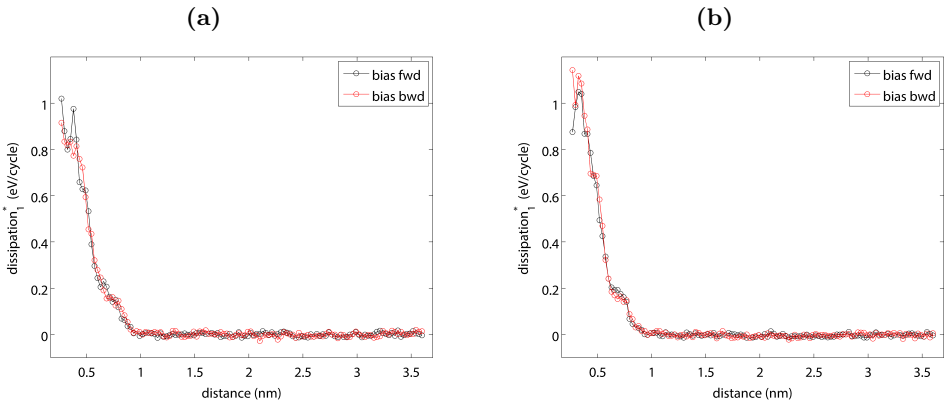

Figure 5.7: Energy dissipated per oscillation cycle on Gr/KBr/Cu. Hill a), valley b).

For the Moire of the KBr-intercalated graphene, strong dissipation was found, as shown in figure 5.7. At relative distances above 0.9 nm on the hill and 0.8 nm on the valley, the dissipation was constant, as Joule-type dissipation was present. On closer approach a slow increase to about 0.2 eV per cycle was found at 0.65 nm and 0.6 nm on the hill and on the valley respectively. In the following the strength of the dissipation changed and a strong increase was observed. It was interrupted by a step at 0.5 nm relative distance. The magnitude of dissipation at this point was 0.6 eV per cycle on the hill 0.7 eV per cycle on valley. Further approaching the surface the dissipation further increased to 0.4 nm. There the maximum dissipation was found close to 1 eV per cycle. With slightly higher dissipation on the valley. Hysteresis features

were small but visible in the strong dissipation regime.
Observations for the dissipation were closely related to the findings for the frequency shift and its related quantities, refer to 5.2. The observed slow increase in dissipation lay in the region between the two wiggles in the frequency shift, coinciding with the plateau in the Van der Waals interaction. With the onset of the strong dissipation a strong slope in frequency shift was found. Further, the maximum dissipation was located where the minimum in the force was found. The hysteresis in the dissipation was directly related to the frequency shift, as it was found at the same positions.
To further study the strong the dissipation regime, it was converted to the non-contact friction coefficient according to 1.1.2. Even though contact was formed, the approach of non-contact friction should hold valid.As the amplitude was large, only in a small fraction of the oscillation cycle contact has been formed. Thus, the main contribution was considered as non-contact friction.

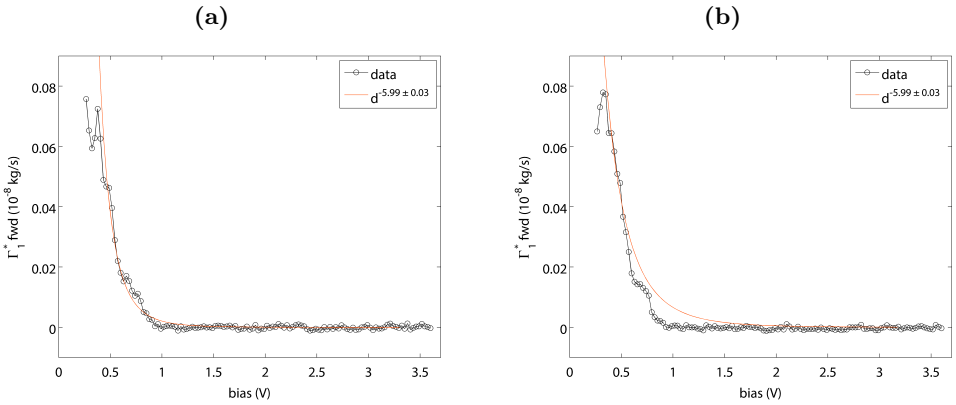

Figure 5.8: Non-contact friction (Γ) for Gr/KBr/Cu. Hill a), valley b).

On hill and valley a proportionality of the non-contact friction to the distance to the power of six ($\Gamma \propto d^{-6}$) was found. The strong Van der Waals interaction with the oscillating tip exited acoustic phonons within graphene increasing the dissipation. [12]
Within this section the dissipation was analyzed and related to the the non-conservative features in the frequency shift. The intimate linkage between these quantities was a strong evidence, that the observed features came from adhesion. In addition the stong increase in the dissipation was attributed to contact formation. [64] The result of the non-contact friction further clarified, that the strong dissipation was by Van der Waals interaction, the driving force for adhesion.
In the last section of this chapter the frequency shift from time-averaged deflection (deflected frequency shift) shall be discussed.

5.4 Time-averaged deflection

Shown in figure 5.9, the deflected frequency shift was directly related to the dissipation. Within the regime of the weaker dissipation only a small decrease,

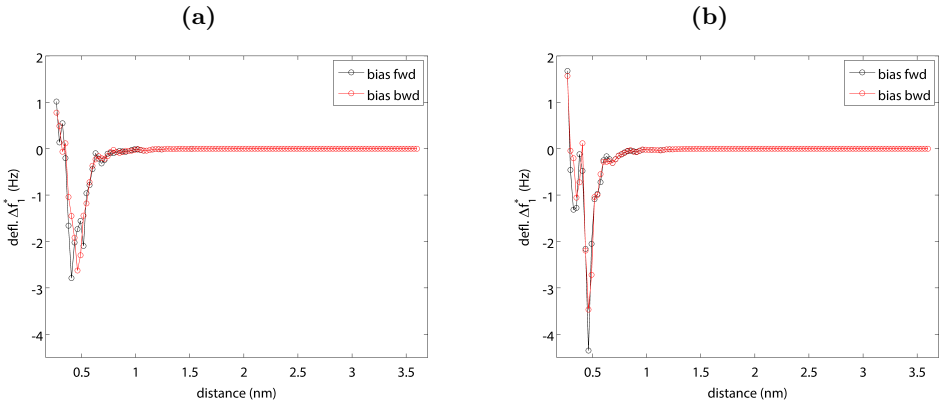

Figure 5.9: Deflected frequency shift on $Gr/KBrCu(111)$. Hill a), valley b).

down to -0.1 Hz, was visible in the deflected frequency shift. With the onset of the strong dissipation a stronger response of the deflected shift set in. Between 0.45 nm and 0.4 nm the minimum was reached with -2.8 Hz on the hill and -4.2 Hz in the valley. On closer approach, the deflected shift was increased again ans became repulsive. It became zero where the maximum dissipation was found. The minimum of the Morse interaction was also found at this point. In respect to the distance between the zero-crossing and the onset of the strong deflection the response was found to be broader on the hill, while it was sharp in the valley. Differences between forward and backward sweep became apparent for both sites in the minimum.
The deflected frequency shift was directly related to the adhesive processes, which will be further discussed in depth in chapter 6.

5.5 Outcomes

In this chapter the a Moire structure for KBr-intercalated graphene has been presented in section 5.1. Comparable to graphene on transition metals, dissipation was present when the Moire structure was resolved, pointing to strong adhesive processes between the sample and the tip. In the valley the dissipation was stronger, indicating a stronger binding to the substrate at these sites. In contrast to the Moire structure presented in chapter 5, the torsional contrast was not inverted.

Dissipation elastic process, in regime were time-averaged deflection is observed.

As strongest response in the frequency shift identified within Van der Waals component agrees well. Spikes in dissipation coincided with features in the normal force and time-averaged channel. The latter complete within the strong dissipation regime.

By the spectroscopy it was found that the set point of the measurement for the tracking -50 Hz, shown in figure **??**, close to 0.6 nm, was found in a non-conservative regime. Also on graphene/KBr/Cu resolution of the Moire structure required the deformation by adhesion. It underlined the imaging mechanism for Moire structures in nc-AFM. [26]

Chapter 6

Elasticity measurements by time-averaged deflection

Within this chapter a new approach will be presented to derive the elastic quantities, namely the Young's modulus and the pretension, by means of nc-AFM. A model for the deformation of thin membranes by Raegan *et al.* [69] will be applied to the measured frequency shift of the time-averaged deflection. The first section 6.1 will introduce the model and explain why its application to nc-AFM is justified. In section 6.1.1 the model of Raegan *et al.* will be applied to nc-AFM and calculations for an expected frequency shift will be discussed. We then will apply the new model to fit the deflected frequency shift data obtained from spectroscopy measurements. In 6.2 for the deflected frequency shift of graphene on copper, that has been presented in chapter 4.

6.1 Model of Deformation

In the model by Raegen *et al.* a suspended, clamped membrane was brought into contact with a flat surface, forming a contact patch. The flat surface then was moved away from the surface. As the membrane adhered to contact patch it was detached from its support, resulting in an elastic stretching. The force for this deformation was from the change in the stress by the deformation and the pre-stress inherent to the membrane and is written as: [69]

$$F = \frac{\pi E' h}{(R^2 - a^2)\ln(R/a)^2}\delta^3 + \frac{2\pi T_0}{\ln(R/a)}\delta \tag{6.1}$$

Where δ is the deflection of the membrane. The term $E' = E/(1-\nu)$ is the Young's modulus of the bulk (E) related to the Poisson ratio (ν). T_0 is the pretension in the thin film. R and a are the radii of the membrane deformation and the contact patch area respectively.
A comparable situation was found when measuring graphene by nc-AFM. The observations made in chapter 4 for graphene on Cu(111) and chapter 5 $KBr/Cu(111)$ showed a large deformation by adhesion within the dissipation and the non-conservative behavior of the frequency shift. This was in agreement with the strong adhesion between found for graphene on Pt(111) by nc-AFM. [26] When the tip was retracted, graphene was detached locally from the surface and adhered to the tip. The adhesion was site dependent with stronger adhesion on the valley.
The contact area of tip and graphene upon adhesion can be considered as the contact patch, defined by the radius of the tip. As the deformation by the adhesion was in the range of a few nanometer, [26] it was small compared to the size of the graphene island. In case of small tip radii (up to 10 nm) and by the logarithmic decay of the deformation, a small local deformation of a few picometer in amplitude and a decay radius of a few nanometer can be expected. Thus the deformation of graphene by the tip can be considered as the deformation of a clamped membrane.
The main difference between the model of Raegen *et al.* and an nc-AFM experiment lay in the formation of contact. In the first case the contact was static, once it was formed, contact remained until the distance was far enough to release the membrane from the contact patch.

In contrast in nc-AFM contact formation was dynamic, depending on the distance and the oscillation of the cantilever. In spectroscopy experiments, as presented in chapters 4 and 5, the relative distance was constant for a given bias sweep. With the backward swing of an oscillation cycle of the cantilever the membrane was adhered. In the following it was pulled from the surface until it was released again. This adhesion led to an anharmonic disturbance of the harmonically driven cantilever that induced a small deflection. The contact formation became a quantity that was time-averaged over the oscillation cycles of the cantilever. It can be considered as quasi-static, as the time-averaged deflection captured a time-averaged value of the deflection of the membrane.
Depending on the distance and the amplitude of the cantilever oscillation the release occured within the backward swing. However, in the limit of small amplitudes, considerable as contact mode, [63] the cantilever was in contact for a full swing of an oscillation cycle at close distances.
At the onset of deformation where adhesion was first observable, the tip was close enough for adhesion, but contact was instantly ruptured again. When the tip was approached closer, the membrane was adhered for a longer time period of the backward swing. The time-averaged deflection became stronger. This behavior was also visible in dissipation. In chapters 4 and 5 we saw an intimate linkage of the deflected frequency shift and the dissipation. With increasing time of contact, an increasing amount of dissipation has been accumulated. At the minimum of the deflected shift, that was found at the minimum of the Morse interaction, the tip approached to the equilibrium position of the membrane. Further approach indented the membrane and contact was also present at the forward swing of the oscillation cycle. This was reflected by an increased deflected frequency shift.
In the following section the model represented by equation 6.1 should be applied to the deflected frequency shift.

6.1.1 Modeled frequency shift response

With the relation of a normalized frequency shift to a force containing a power law [70] 6.1 became:

$$\Delta\gamma = \frac{\pi E' h}{(R^2 - a^2)\ln(R/a)^2}\delta^{3.5}\frac{\Gamma(4)}{\Gamma(4.5)\sqrt{2\pi}} + \frac{2\pi T_0}{\ln(R/a)}\delta^{1.5}\frac{\Gamma(2)}{\Gamma(2.5)\sqrt{2\pi}} \quad (6.2)$$

With the relation for the normalized frequency shift $\Delta f = \Delta\gamma\frac{f_0}{kA^{3/2}}$, [70] the elastic frequency shift yields:

$$\Delta f = A\frac{\pi E' h}{(R^2 - a^2)\ln(R/a)^2}(m(\delta - \delta_0))^{3.5} - B\frac{2\pi T_0}{\ln(R/a)}(n(\delta - \delta_0))^{1.5} \quad (6.3)$$

With the pre-factors A and B being:

$$A = \frac{f_0\Gamma(4)}{kA^{3/2}\sqrt{2\pi}\Gamma(4.5)} \quad (6.4a)$$

$$B = \frac{f_0 \Gamma(2)}{k A^{3/2} \sqrt{2\pi} \Gamma(2.5)} \tag{6.4b}$$

The following modifications have been introduced in equation 6.3. δ_0, an onset of the deformation has been introduced, as the tip had to be approached to a certain distance to adhere graphene.
A rate of deformation for the slope from the onset to the minimum (n) and from the minimum to the repulsion at zero (n). As the deflection of the film by the tip was an unknown quantity, these were introduced to relate the deflection of the membrane to the deflection of the cantilever. The rates had the magnitude of pm/nm. To account for the equilibrium position, the sign in 6.3 had to be switched.
In the following the dependence of the frequency shift on the Young's modulus, pretension and deformation rate will be discussed. Literature values of 1 TPa for the Young' s modulus, 0.4 N/m and the Poisson ratio of 0.165 for a free-standing graphene membrane were taken from Lee *et al.* [71], to calculate the deflected frequency shift according to equation 6.3.

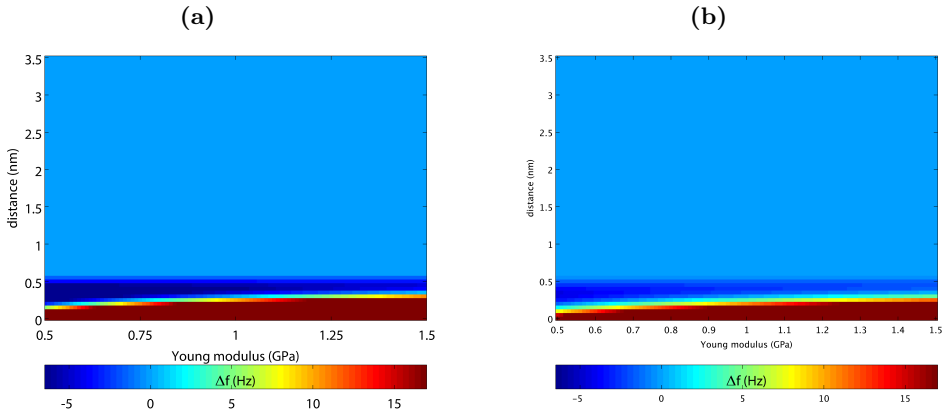

Figure 6.1: Modeled frequency shift response Young modulus with pretension of 0.4 N/m and deformation rate of 300 pm/nm, left first mode, right second mode.

In figure 6.1 a), the frequency shift response in respect to the change of the Young's modulus was calculated. No frequency shift response was found before the onset of the deformation. The frequency shift was reduced to a minimum followed by a strong increase. For smaller Young's module the minimum appeared broader and deeper. It was shifted towards the surface. For a higher module the minimum became weaker and sharper. The same response was found for the second mode, shown in 6.1 b). It overall appearance was weaker than those of the first mode.

The dependence of the frequency shift on the pretension in the sample, presented in figure 6.2. Stronger and broader minima were found for a larger pretension. At low pretension the minimum almost vanished.

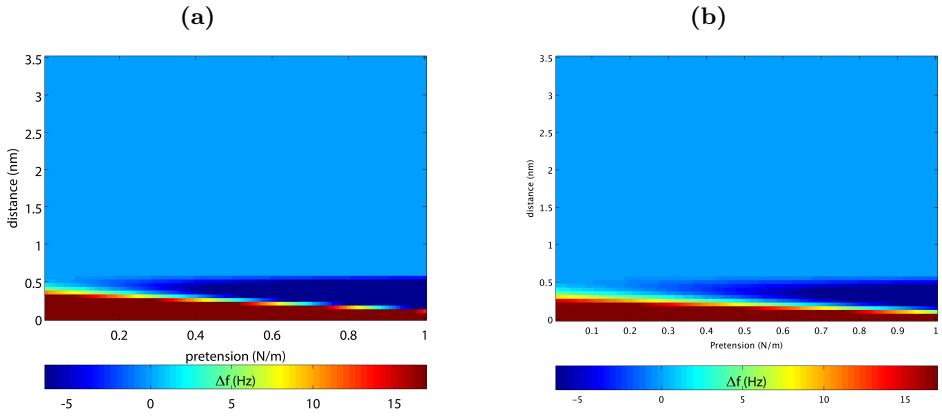

Figure 6.2: Modeled frequency shift response pretension with Young modulus of 1 TPa and deformation rate of 300 pm/nm, left first mode, right second mode.

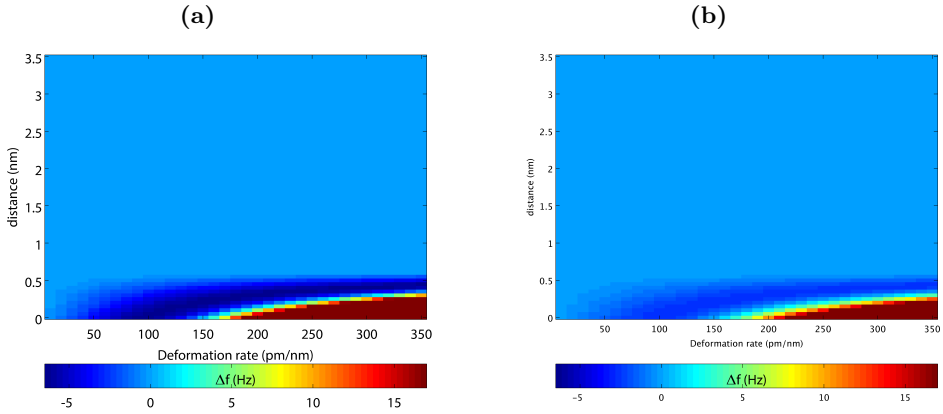

Figure 6.3: Modeled frequency shift response deformation rate for Young modulus of 1 TPa and pretension of 0.4 N/m, left first mode, right second mode.

Presented in figure 6.3 a) is the influence of the rate of deformation on the frequency shift response. At deformation rates lower then 50 pm/nm no minima became visible. It was probably shifted towards the surface and not reasonable to explain the behavior of the frequency shift. Below 150 pm/nm a broad minimum became visible. For increasing rates the minimum stabilized around 0.45 nm and became sharper. The magnitude of the minimum was independent of the rate. The response of the second mode, shown in 6.3 b, was weaker compared to the first mode, but showed a comparable response.
In conclusion, the frequency shift expected for a deformation according to the model was in the range of the frequency shift by the time-averaged deflection. The pretension scaled opposite to the Young modulus. In addition, the response of the frequency shift was stronger for changes in the pretension, compared to the Young's modulus.

In the following sections the model will by applied by fitting the time-averaged frequency shift for graphene on copper.

6.2 Elasticity measurements on Cu/Gr

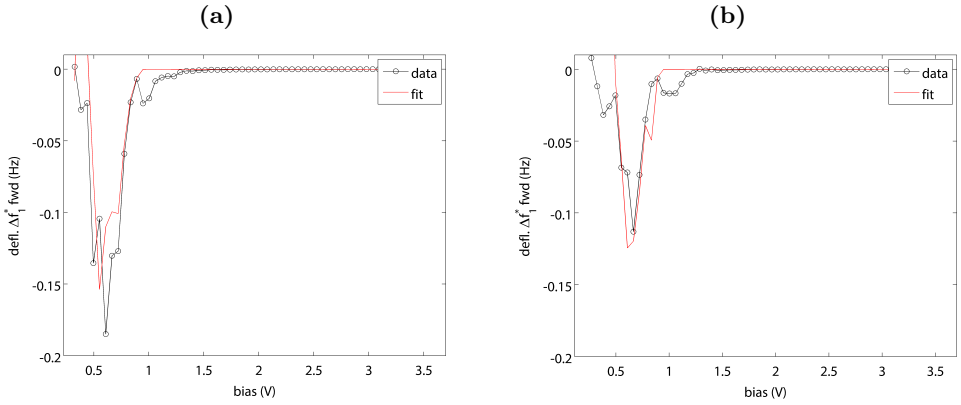

Figure 6.4: Frequency shift by time averaged deflection Gr/Cu. Hill a), valley b). A: 8 nm, k $30N/m$, Q 31k?

In figure 6.4 the deflected frequency shift for a hill and a valley of graphene on Cu(111) were presented. A stronger and broader deflection was found on the hill. The minimum was underestimated by the fit for the hill. However, this should not have influenced the estimation of the deformation rate. A higher pretension was found for the hill with 0.22 N/m compared to pretension on the valley with 0.25 N/m. The difference was 37.3 mN/m. For the Young's modulus a value of 0.82 TPa was found for the hill and 0.84 TPa for the valley. This yielded a difference of 16.6 GPa. The deformation rate from the onset of deformation at 0.92 nm to the minimum at 0.6 nm was 16.2 pm/nm and below the minimum 49 pm/nm on the hill. For the valley these were 19.5 and 50.9 pm/nm, with the onset shifted by 30 pm towards the surface. A radius of deformation of 2.44 nm was found for the hill and 1.78 nm for the valley respectively.

6.3 Outcomes

A new model was developed to measure elastic deformations at the tip sample junction by means of the time-averaged deflection in nc-AFM. were of reasonable magnitude.
The deformation was found to be localized, as assumed in the discussion in 6.1.
Larger values for the Young's modulus, pretension were found in the valley on graphene. This was in agreement with the stronger dissipation by adhesion for the valley, as discussed in chapter 4. Compared to literature values for free-standing graphene, [71] a lower Young's modulus and higher pretension were found. The higher pretension was reasonable, as the deformation radius was larger for the hill. While the valley was constraint to deform by its stronger binding to the substrate, the hill This first result showed that reason-

able However, further verification by reference experiments is necessary, where the model could be compared to the outcome of indentation experiments or by measurement contact resonance on the same sample.
An improvement for the measurement would by a bimodal setup, with a large first mode to establish stable measurement conditions. The second flexural mode then can be employed to measure the time-averaged defection with high sensitivity. In addition the torsional mode may can be employed to measure the shear modulus.

Bibliography

[1] Li Gao, Jeffrey R Guest, and Nathan P Guisinger. Epitaxial graphene on Cu(111). *Nano letters*, 10(9):3512–6, sep 2010.

[2] Sergey M. Kozlov, Francesc Viñes, and Andreas Görling. Bonding Mechanisms of Graphene on Metal Surfaces. *The Journal of Physical Chemistry C*, (111):7360–7366, 2012.

[3] Matthias Batzill. The surface science of graphene: Metal interfaces, CVD synthesis, nanoribbons, chemical modifications, and defects. *Surface Science Reports*, 67(3-4):83–115, mar 2012.

[4] TH Bointon, Ivan Khrapach, and Rositza Yakimova. Approaching magnetic ordering in graphene materials by FeCl3 intercalation. *Nano Lett.*, 14:1751–1755, mar 2014.

[5] R. C. Cammarata, T. M. Trimble, and D. J. Srolovitz. Surface stress model for intrinsic stresses in thin films. *Journal of Materials Research*, 15(11):2468–2474, jan 2000.

[6] V. B. Shenoy, C. D. Reddy, a. Ramasubramaniam, and Y. W. Zhang. Edge-stress-induced warping of graphene sheets and nanoribbons. *Physical Review Letters*, 101(December):2–5, 2008.

[7] PA Khomyakov, G. Giovannetti, and PC Rusu. First-principles study of the interaction and charge transfer between graphene and metals. *Physical Review B*, 79(19):195425, may 2009.

[8] K. Wandelt. The local work function: Concept and implications. *Applied Surface Science*, 111:1 – 10, 1997. Proceedings of the International Vacuum Electron Sources Conference 1996.

[9] Bert Bert Voigtlaender. *Scanning Probe Microscopy*. NanoScience and Technology. Springer, Berlin, Heidelberg, 2015.

[10] PC Rusu, Gianluca Giovannetti, and Christ Weijtens. First-principles study of the dipole layer formation at metal-organic interfaces. *Physical Review B*, 81(12):125403, mar 2010.

[11] Kenji Natori, Daijiro Otani, and Nobuyuki Sano. Thickness dependence of the effective dielectric constant in a thin film capacitor. *Applied Physics Letters*, 73(5):632–634, 1998.

[12] A. I. Volokitin and B. N J Persson. Near-field radiative heat transfer and noncontact friction. *Rev. Mod. Phys.*, 79(4):1291–1329, 2007.

[13] A.H. Castro Neto, F. Guinea, N. M. R. Peres, and K. S. Novoselov. Electronic properties of graphene. *Reviews of Modern Physics*, 1(81):109 – 162, 2009.

[14] W Haiss. Surface stress of clean and adsorbate-covered solids. *Reports on Progress in Physics*, 64:591–648, 2001.

[15] H. Ibach. Adsorbate-induced surface stress. *Journal of Vacuum Science & Technology A: Vacuum, Surfaces, and Films*, 12(October 1993):2240, 1994.

[16] Z. Crljen, P. Lazic, D. Sokcevic, and R. Brako. Relaxation and reconstruction on (111) surfaces of Au, Pt, and Cu. *Physical Review B*, 68:8, 2003.

[17] M Mansfield and R J Needs. Application of the Frenkel-Kontorova model to surface reconstructions. *Journal of Physics: Condensed Matter*, 2:2361–2374, 1999.

[18] Xiuyun Zhang, Ziwei Xu, Li Hui, John Xin, and Feng Ding. How the Orientation of Graphene Is Determined during Chemical Vapor Deposition Growth. *The Journal of Physical Chemistry Letters*, 3(19):2822–2827, oct 2012.

[19] Kemal Celebi, MT Cole, and JW Choi. Evolutionary Kinetics of Graphene Formation on Copper - Supplemental. *Nano letters*, 13(3):967–74, mar 2013.

[20] Eros Mariani and Felix Von Oppen. Flexural phonons in free-standing graphene. *Physical Review Letters*, 100(7), 2008.

[21] G. Giovannetti, P. Khomyakov, G. Brocks, V. Karpan, J. van den Brink, and P. Kelly. Doping Graphene with Metal Contacts. *Physical Review Letters*, 101(2):026803, jul 2008.

[22] José I. Martínez, Pablo Merino, Anna L. Pinardi, Otero Irurueta Gonzalo, Mariá F. López, Javier Méndez, and José A. Martín-Gago. Role of the Pinning Points in epitaxial Graphene Moiré Superstructures on the Pt(111) Surface. *Scientific Reports*, 6(February):2–11, 2016.

[23] Zachary H. Aitken and Rui Huang. Effects of mismatch strain and substrate surface corrugation on morphology of supported monolayer graphene. *J. Appl. Phys.*, 107(12):1–10, 2010.

[24] Rui He, Liuyan Zhao, Nicholas Petrone, Keun Soo Kim, Michael Roth, James Hone, Philip Kim, Abhay Pasupathy, and Aron Pinczuk. Large physisorption strain in chemical vapor deposition of graphene on copper substrates. *Nano letters*, 12(5):2408–13, may 2012.

[25] Pablo Merino, M Švec, and AL Pinardi. Strain-driven moire superstructures of epitaxial graphene on transition metal surfaces. *ACS nano*, pages 5627–5634, 2011.

[26] B. De La Torre, M. Ellner, P. Pou, N. Nicoara, Rub??n P??rez, and J. M. G??mez-Rodr??guez. Atomic-Scale Variations of the Mechanical Response of 2D Materials Detected by Noncontact Atomic Force Microscopy. *Phys. Rev. Lett.*, 116(24):1–6, 2016.

[27] P. Süle, M. Szendró, C. Hwang, and L. Tapasztó. Rotation misorientated graphene moire superlattices on Cu(111): classical molecular dynamics simulations and scanning tunneling microscopy studies. *Carbon*, (77):1082–1089, 2014.

[28] Eun Ah Kim and A. H. Castro Neto. Graphene as an electronic membrane. *Europhysics Letters*, 84(5):2–7, 2008.

[29] M. I. Katsnelson, K. S. Novoselov, and A. K. Geim. Chiral tunnelling and the Klein paradox in graphene. *Nature Physics*, 2(9):620–625, 2006.

[30] Bing Huang, Miao Liu, Ninghai Su, Jian Wu, Wenhui Duan, Bing Lin Gu, and Feng Liu. Quantum manifestations of graphene edge stress and edge instability: A first-principles study. *Physical Review Letters*, 102(April):1–4, 2009.

[31] a. H. Castro Neto. Electron-phonon coupling and Raman spectroscopy in graphene. *Physical Review B*, 75(4):045404, jan 2007.

[32] Y. Murata, E. Starodub, B. B. Kappes, C. V. Ciobanu, N. C. Bartelt, K. F. McCarty, and S. Kodambaka. Orientation-dependent work function of graphene on Pd(111). *Applied Physics Letters*, 97(14):143114, 2010.

[33] Manabu Kiguchi, Ryotaro Arita, Genki Yoshikawa, Yoshiaki Tanida, Masao Katayama, Koichiro Saiki, Atsushi Koma, and Hideo Aoki. Metal-induced gap states at well defined alkali-halide/metal interfaces. *Physical review letters*, 90(May):196803, 2003.

[34] C. Riedl, C. Coletti, T. Iwasaki, a. a. Zakharov, and U. Starke. Quasi-Free-Standing Epitaxial Graphene on SiC Obtained by Hydrogen Intercalation. *Physical Review Letters*, 103(24):246804, dec 2009.

[35] P Sutter, JT Sadowski, and EA Sutter. Chemistry under Cover: Tuning Metal-Graphene Interaction by Reactive Intercalation. *Journal of the American ...*, 11973(18):8175–8179, 2010.

[36] Konstantin V. Emtsev, Alexei a. Zakharov, Camilla Coletti, Stiven Forti, and Ulrich Starke. Ambipolar doping in quasifree epitaxial graphene on SiC(0001) controlled by Ge intercalation. *Physical Review B*, 84(12):125423, sep 2011.

[37] a. Varykhalov, J. Sánchez-Barriga, a. Shikin, C. Biswas, E. Vescovo, a. Rybkin, D. Marchenko, and O. Rader. Electronic and Magnetic Properties of Quasifreestanding Graphene on Ni. *Physical Review Letters*, 101(15):157601, oct 2008.

[38] Hui Zhang, Qiang Fu, Yi Cui, Dali Tan, and Xinhe Bao. Growth mechanism of graphene on Ru (0001) and O2 adsorption on the graphene/Ru (0001) surface. *The Journal of Physical ...*, 4(0001):8296–8301, 2009.

[39] U. Starke, S. Forti, K.V. Emtsev, and C. Coletti. Engineering the electronic structure of epitaxial graphene by transfer doping and atomic intercalation. *MRS Bulletin*, 37(12):1177–1186, nov 2012.

[40] M Petrović, I Šrut Rakić, S Runte, C Busse, J T Sadowski, P Lazić, I Pletikosić, Z-H Pan, M Milun, P Pervan, N Atodiresei, R Brako, D Šokčević, T Valla, T Michely, and M Kralj. The mechanism of caesium intercalation of graphene. *Nature Communications*, 4:2772, nov 2013.

[41] Franz J. Giessibl. Advances in atomic force microscopy. *Reviews of modern physics*, 75(July), 2003.

[42] Ernst Meyer. Atomic Force Microscopy. *Progress in Surface Science*, 41:3–49, 1992.

[43] Franz J. Giessibl. Atomic resolution of the silicon (111)-(7x7) surface by atomic force microscopy. *Science*, (13):1–4, 1995.

[44] T. R. Albrecht, P. Gruetter, D. Horne, and D. Rugar. Frequency modulation detection using high-Q cantilevers for enhanced force microscope sensitivity. *J. Appl. Phys.*, 69(2):668, 1991.

[45] Franz J. Giessibl. Forces and frequency shifts in atomic-resolution dynamic-force microscopy. *Phys. Rev. B*, 56(24):16010–16015, 1997.

[46] Franz J. Giessibl. A direct method to calculate tip-sample forces from frequency shifts in frequency-modulation atomic force microscopy. *Appl. Phys. Lett.*, 78(1):123–125, 2001.

[47] Shigeki Kawai, Shin Ichi Kitamura, Dai Kobayashi, Sakae Meguro, and Hideki Kawakatsu. An ultrasmall amplitude operation of dynamic force microscopy with second flexural mode. *Appl. Phys. Lett.*, 86(19):1–3, 2005.

[48] Shigeki Kawai, Shin Ichi Kitamura, Dai Kobayashi, and Hideki Kawakatsu. Dynamic lateral force microscopy with true atomic resolution. *Appl. Phys. Lett.*, 87(17):1–3, 2005.

[49] Shigeki Kawai, Thilo Glatzel, Sascha Koch, Bartosz Such, Alexis Baratoff, and Ernst Meyer. Systematic Achievement of Improved Atomic-Scale Contrast via Bimodal Dynamic Force Microscopy. *Phys. Rev. Lett.*, 103(22):1–4, nov 2009.

[50] Shigeki Kawai, Thilo Glatzel, Sascha Koch, Bartosz Such, Alexis Baratoff, and Ernst Meyer. Ultrasensitive detection of lateral atomic-scale interactions on graphite (0001) via bimodal dynamic force measurements. *Phys. Rev. B*, 81(8):1–7, feb 2010.

[51] Shigeki Kawai, Sadik Hafizovic, Thilo Glatzel, Alexis Baratoff, and Ernst Meyer. Rapid reconstruction of a strong nonlinear property by a multiple lock-in technique. *Phys. Rev. B*, 85(16):1–7, apr 2012.

[52] Shigeki Kawai, Thilo Glatzel, Hans-Josef Hug, and Ernst Meyer. Atomic contact potential variations of Si(111)-7 x 7 analyzed by Kelvin probe force microscopy. *Nanotechnology*, 21(24):245704, 2010.

[53] Sascha Sadewasser and Thilo Glatzel. *Kelvin Probe Force Microscopy*, volume 48 of *Springer Series in Surface Sciences*. Springer-Verlag Berlin Heidelberg, 1 edition, 2012.

[54] Sascha Sadewasser, Pavel Jelinek, and CK Fang. New insights on atomic-resolution frequency-modulation Kelvin-probe force-microscopy imaging of semiconductors. *Phys. Rev. Lett.*, 103(26):266103, dec 2009.

[55] Laurent Nony, Adam Foster, Franck Bocquet, and Christian Loppacher. Understanding the Atomic-Scale Contrast in Kelvin Probe Force Microscopy. *Phys. Rev. Lett.*, 103(3):036802, jul 2009.

[56] Shigeki Kawai, Thilo Glatzel, Sascha Koch, Bartosz Such, Alexis Baratoff, and Ernst Meyer. Time-averaged cantilever deflection in dynamic force spectroscopy. *Phys. Rev. B*, 80(8):1–7, aug 2009.

[57] M. Guggisberg, M. Bammerlin, Ch. Loppacher, O. Pfeiffer, a. Abdurixit, V. Barwich, R. Bennewitz, a. Baratoff, E. Meyer, and H.-J. Güntherodt. Separation of interactions by noncontact force microscopy. *Physical Review B*, 61(16):11151–11155, apr 2000.

[58] Elena T Herruzo and Ricardo Garcia. Theoretical study of the frequency shift in bimodal FM-AFM by fractional calculus. *Beilstein J. Nanotechnol.*, 3:198–206, jan 2012.

[59] John E. Sader and Suzanne P. Jarvis. Interpretation of frequency modulation atomic force microscopy in terms of fractional calculus. *Phys. Rev. B - Condens. Matter Mater. Phys.*, 70(1):8–10, 2004.

[60] John E Sader, Takayuki Uchihashi, Michael J Higgins, Alan Farrell, Yoshikazu Nakayama, and Suzanne P Jarvis. Quantitative force measurements using frequency modulation atomic force microscopy: theoretical foundations. *Nanotechnology*, 16(3):S94–S101, 2005.

[61] Kazuhiro Suzuki, Noriaki Oyabu, Kei Kobayashi, Kazumi Matsushige, and Hirofumi Yamada. Atomic-resolution imaging of graphite-water interface by frequency modulation atomic force microscopy. *Applied Physics Express*, 4(12), 2011.

[62] Liangti Qu, Liming Dai, Morley Stone, Zhenhai Xia, and Zhong Lin Wang. Carbon nanotube arrays with strong shear binding-on and easy normal lifting-off. *Science*, 322(5899):238–242, 2008.

[63] Shigeki Kawai, Thilo Glatzel, Bartosz Such, Sascha Koch, Alexis Baratoff, and Ernst Meyer. Energy dissipation in dynamic force microscopy on KBr (001) correlated with atomic-scale adhesion phenomena. *Phys. Rev. B*, 245419:1–10, 2012.

[64] Shigeki Kawai, Filippo Federici Canova, Thilo Glatzel, Adam S. Foster, and Ernst Meyer. Atomic-scale dissipation processes in dynamic force spectroscopy. *Phys. Rev. B*, 84(11):1–9, sep 2011.

[65] R. Boisgard, J. P. Aim??, and G. Couturier. Surface mechanical instabilities and dissipation under the action of an oscillating tip. *Surface Science*, 511(1-3):171–182, 2002.

[66] G. Couturier, J. P. Aim??, J. Salardenne, R. Boisgard, A. Gourdon, and S. Gauthier. A mechanical approach to the dissipation process in NC-AFM: Experiments, model and simulation. *Applied Physics A: Materials Science and Processing*, 72(7):47–50, 2001.

[67] Renju Zacharia, Hendrik Ulbricht, and Tobias Hertel. Interlayer cohesive energy of graphite from thermal desorption of polyaromatic hydrocarbons. *Physical Review B - Condensed Matter and Materials Physics*, 69(15):1–7, 2004.

[68] Priya Vashishta, Rajiv K. Kalia, Aiichiro Nakano, and Jose Pedro Rino. Interaction potential for silicon carbide: A molecular dynamics study of elastic constants and vibrational density of states for crystalline and amorphous silicon carbide. *Journal of Applied Physics*, 101(10):103515, 2007.

[69] A. N. Raegen, K. Dalnoki-Veress, K. T. Wan, and R. A L Jones. Measurement of adhesion energies and Young's modulus in thin polymer films using a novel axi-symmetric peel test geometry. *European Physical Journal E*, 19(4):453–459, 2006.

[70] Franz J. Giessibl and H Bielefeldt. Physical interpretation of frequency-modulation atomic force microscopy. *Physical Review B*, 2000.

[71] Changgu Lee, Xiaoding Wei, Jeffrey W Kysar, James Hone, and =. Measurement of the Elastic Properties and Intrinsic Strength of Monolayer Graphene. *Science (80-.).*, 321(18 July 2008):385–388, 2008.

List of Figures

Chapter 7

Appendix

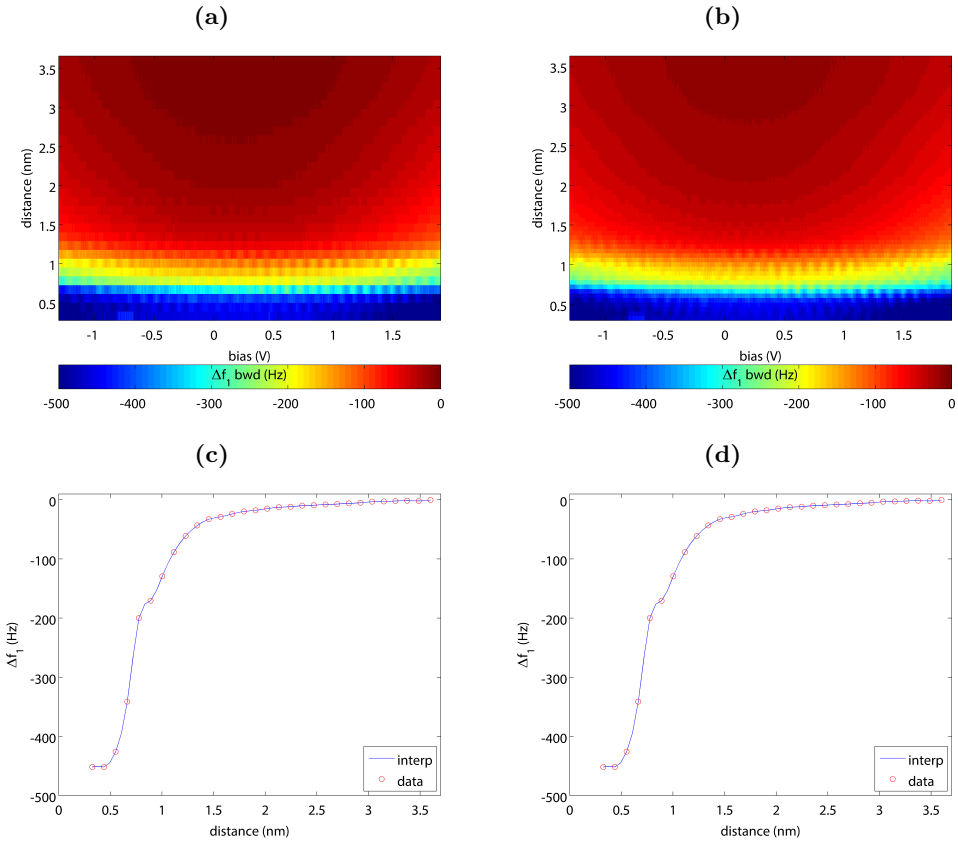

Figure 7.1: Interpolation for a hill site on $Gr/Cu(111)$. Raw data of forward swept curves (from positive to negative voltages) in a). Time averaged deflection along the CPD b). Data shifted by time averaged deflection. Points taken from interpolation with one addtional point inbetween the data points. Comparison of interpolation (blue line) at 0.197 V and raw data (red dots) close to the CPD d). A: 400 pm, k $6.941 kN/m$, Q 12982., add line for clarity of star curves

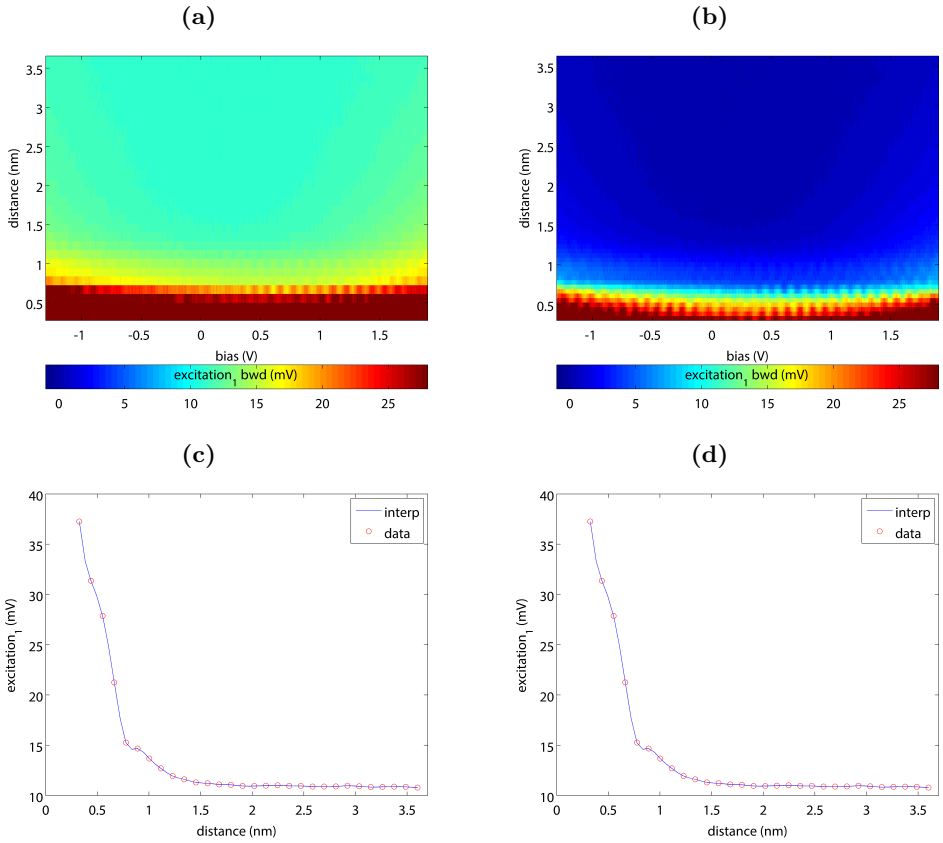

Figure 7.2: Interpolation for a hill site on $Gr/Cu(111)$. Raw data of forward swept curves (from positive to negative voltages) in a). Time averaged deflection along the CPD b). Data shifted by time averaged deflection. Points taken from interpolation with one addtional point inbetween the data points. Comparison of interpolation (blue line) at 0.197 V and raw data (red dots) close to the CPD d). A: 400 pm, k 6.941kN/m, Q 12982., add line for clarity of star curves

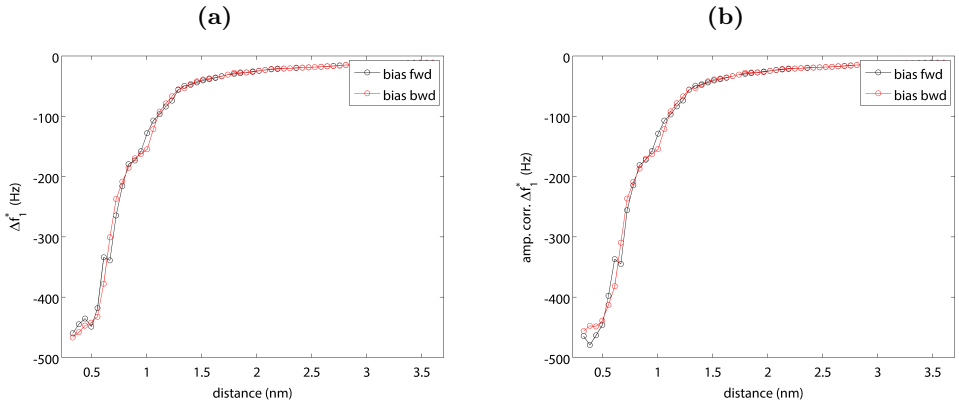

Figure 7.3: Change in frequency shift by amplitude estimation on $Gr/Cu(111)$. A: 400 pm, k , Q 14k?, add line for clarity of star curves

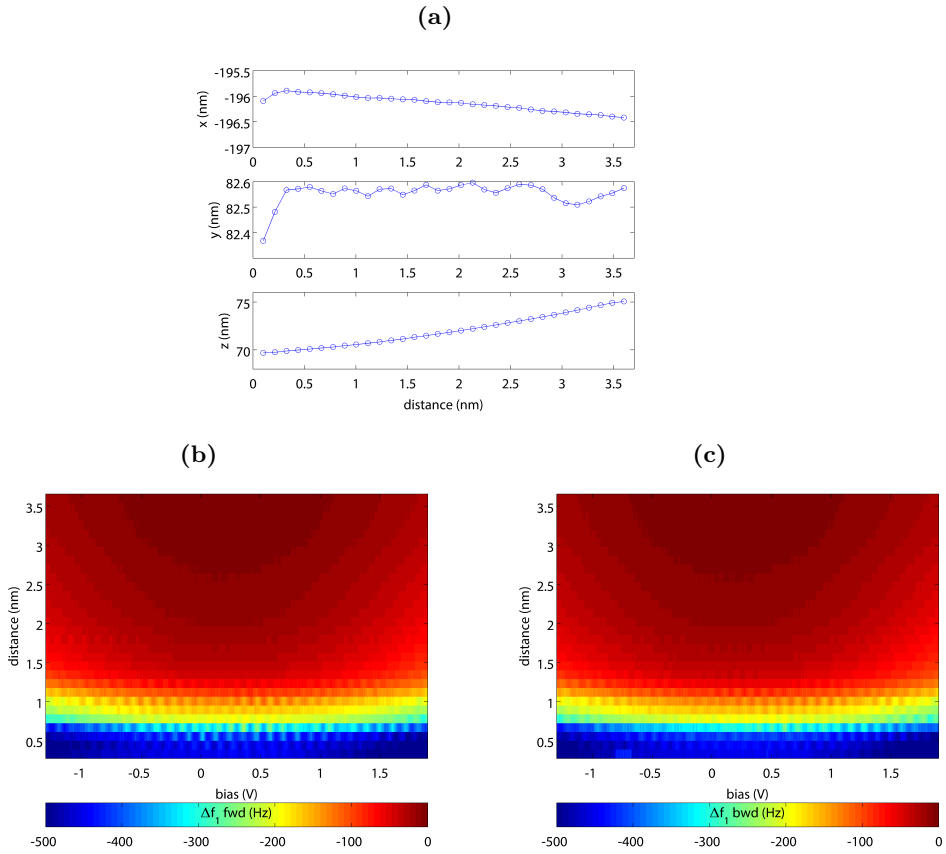

Figure 7.4: Position of the tip for the selected experiment on a hill site on $Gr/Cu(111)$ shown in a). Maps for the frequency shift presented as raw data for forward b) and backward c) bias sweep. Spectroscopy parameter: $\Delta x = -4.1nm, \Delta y = -1.5nm, \Delta z = 2nm, off - set = 1nm, distance = 3.5nm, f_{AT} = 10Hz, r_{AT} = 300pm$.

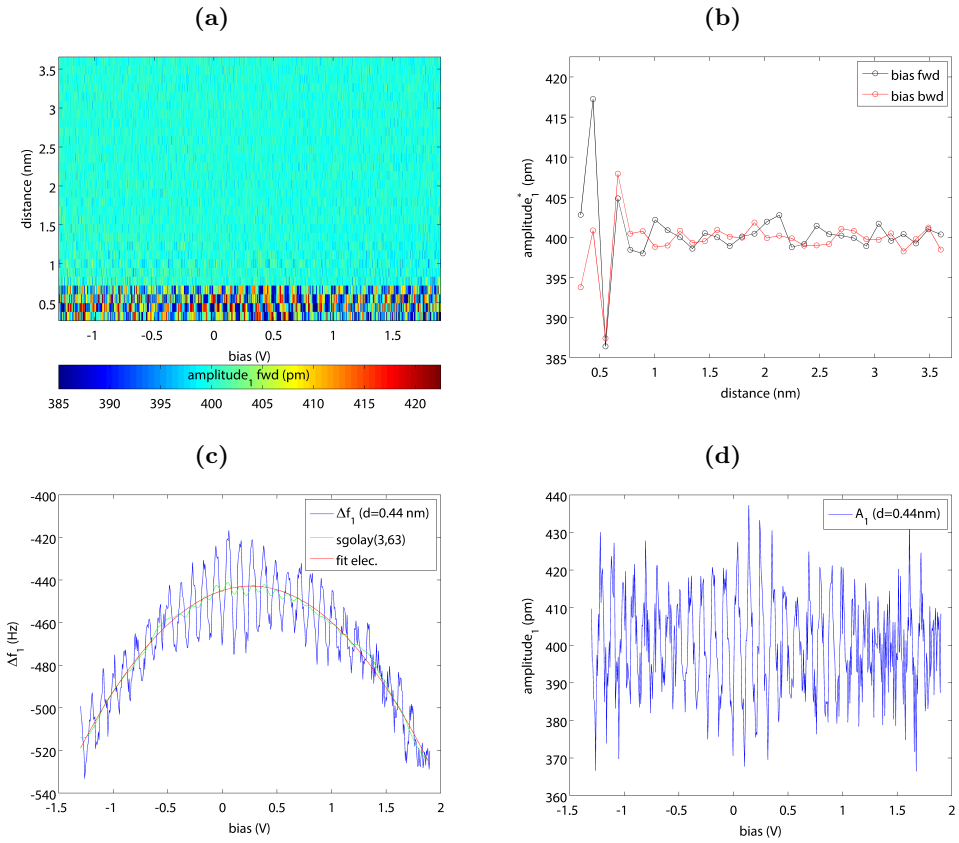

Figure 7.5: Response of the amplitude for a hill on $Gr/Cu(111)$.

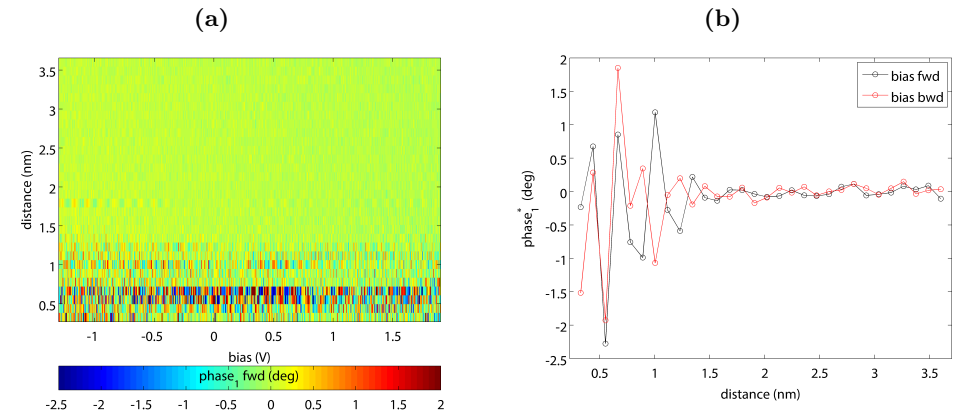

Figure 7.6: Response of phase on a hill on $Gr/Cu(111)$.

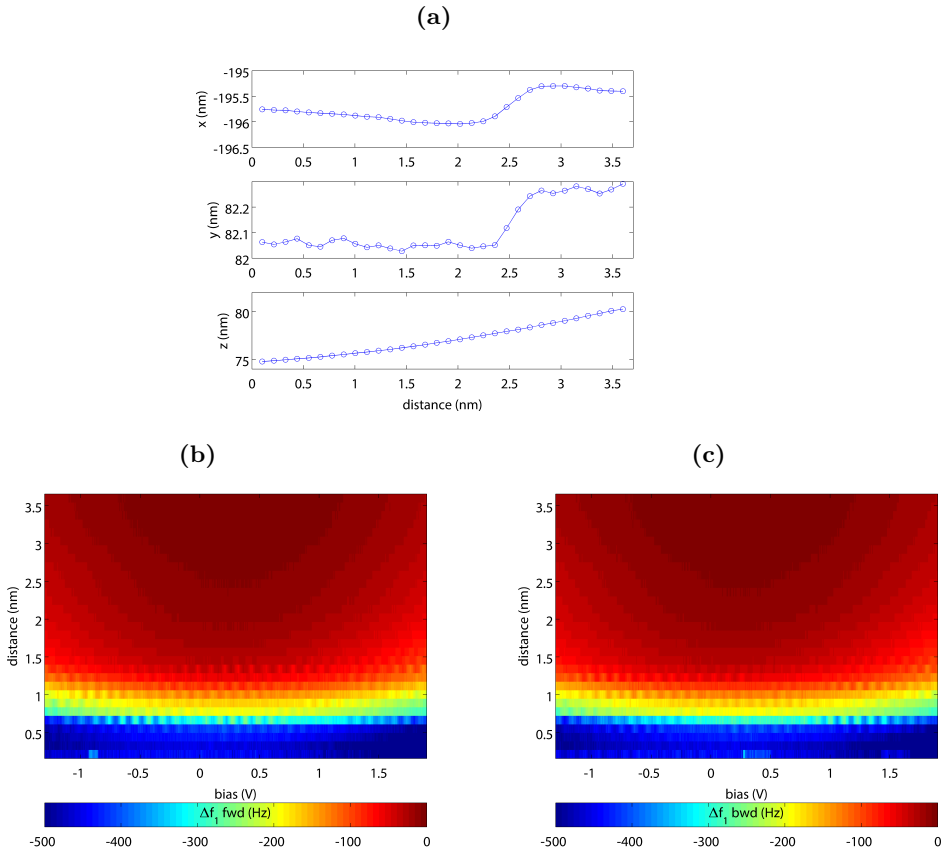

Figure 7.7: Frequency shift response for a valley site on $Gr/Cu(111)$. Raw data of forward swept curves (from positive to negative voltages) in b). Spectroscopy parameter: $\Delta x = -2.7nm, \Delta y = -1.5nm, \Delta z = 2nm, off - set = 1nm, distance = 3.5nm, f_{AT} = 10Hz, r_{AT} = 300pm$.

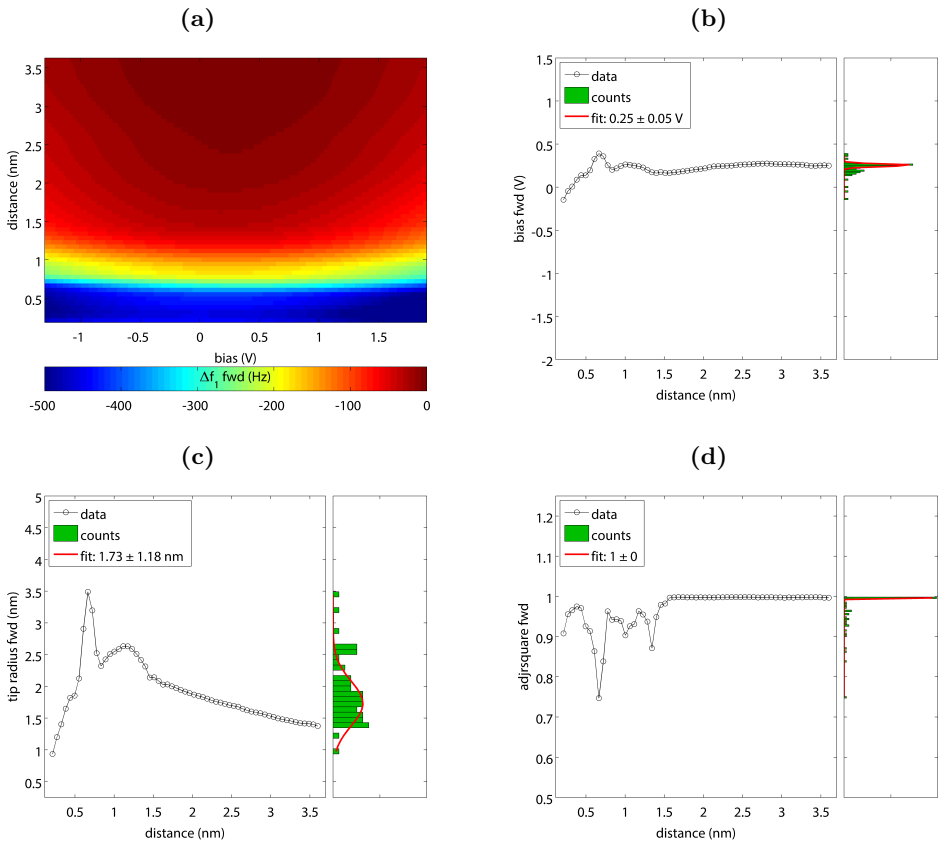

Figure 7.8: Frequency shift response for a valley site on $Gr/Cu(111)$ fitted line wise for the electrostatic interaction along the bias axis . Map reconstructed from the fit results in a). Change in bias along the compensated electrostatic force b). Tip radius obtained by the fit model c). Goodness of fit represented by the adjusted root square d).

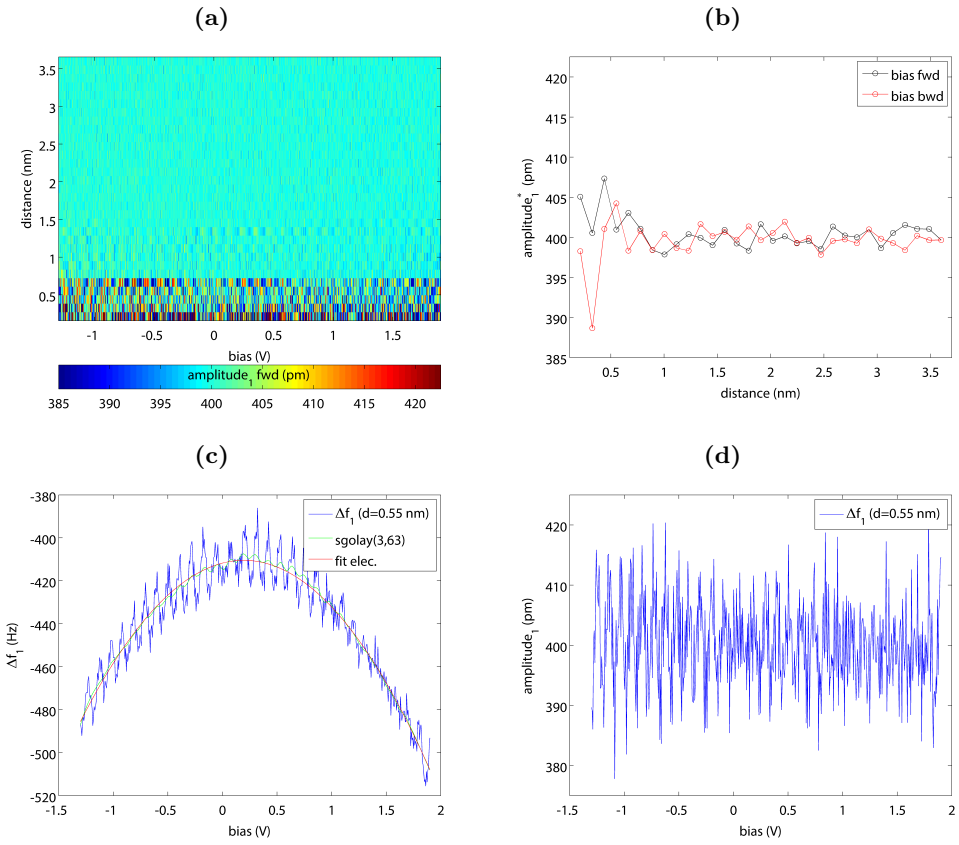

Figure 7.9: Response of amplitude for a valley site on $Gr/Cu(111)$.

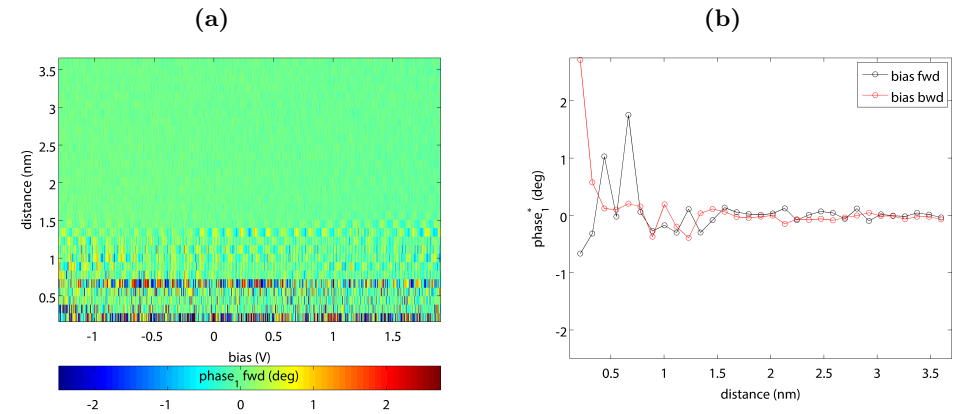

Figure 7.10: Response of phase for a valley site on $Gr/Cu(111)$.

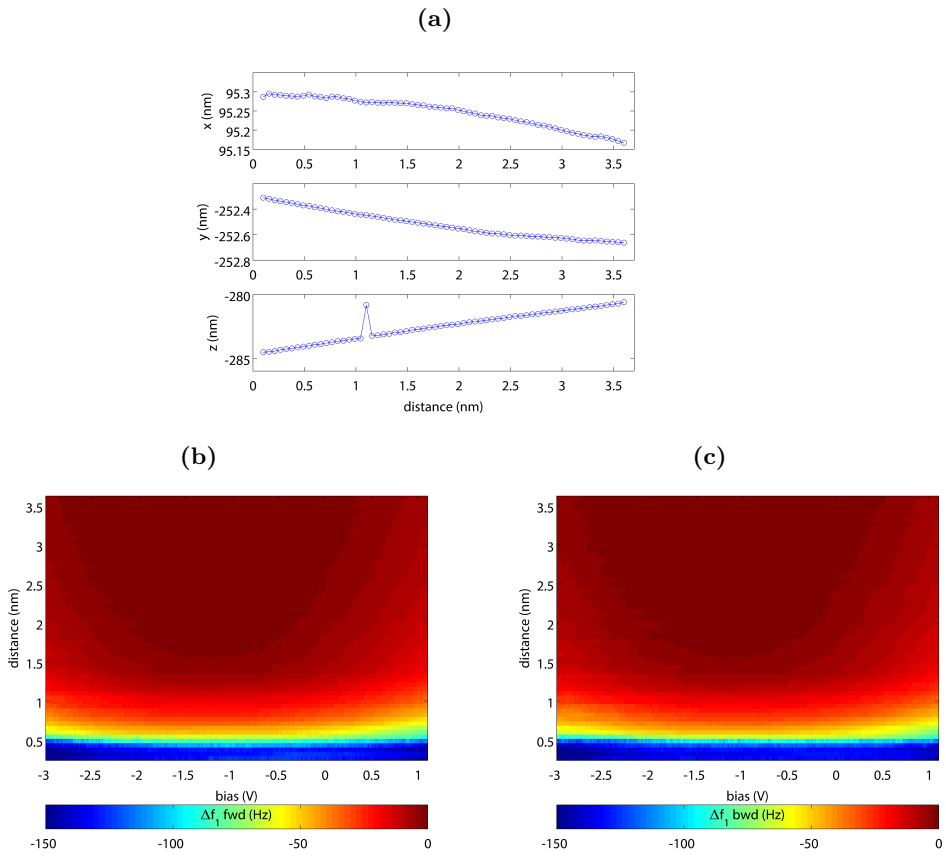

Figure 7.11: Frequency shift response for a hill site on $Gr/Cu(111)$. Raw data of forward swept curves (from positive to negative voltages) in a). Time averaged deflection along the CPD b). Data shifted by time averaged deflection. Points taken from interpolation with one addtional point inbetween the data points. Comparison of raw data (red dots) and data connected to a long range curve calculated from the fitting results along both directions d) .Imaging parameter: $\Delta f_{1st} = -50Hz, A_{1st} = 8nm, k_{1st} = 30.13N/m, Q_{1st} = 30'854, A_{tr} = 150pm, k_{tr} =, Q_{tr} = 139'488$.

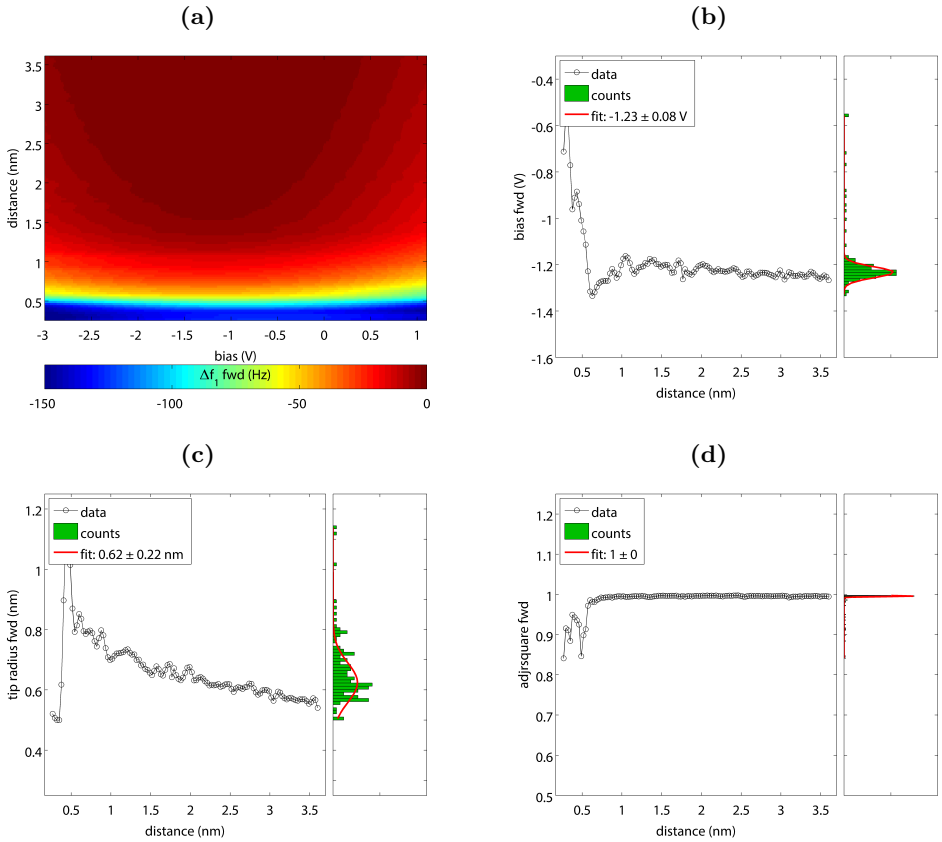

Figure 7.12: Frequency shift response for a hill site on $Gr/Cu(111)$ fitted line wise for the electrostatic interaction along the bias axis . Map reconstructed from the fit results in a). Change in bias along the compensated electrostatic force b). Tip radius obtained by the fit model c). Goodness of fit represented by the adjusted root square d). A: 400 pm, k 6.941kN/m, Q 12982., add line for clarity of star curves

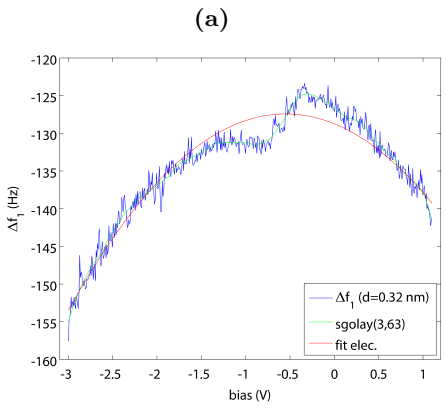

Figure 7.13: Response of amplitude on $Gr/Cu(111)$. A: 400 pm, k , Q 14k?, add line for clarity of star curves

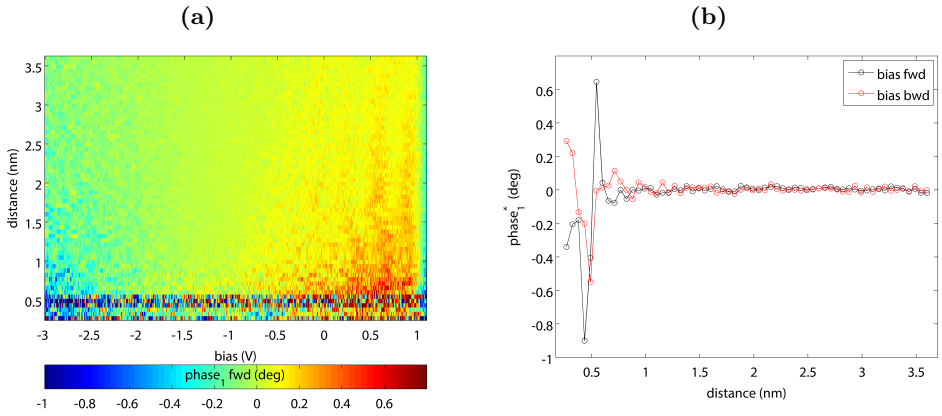

Figure 7.14: Response of phase on $Gr/Cu(111)$.

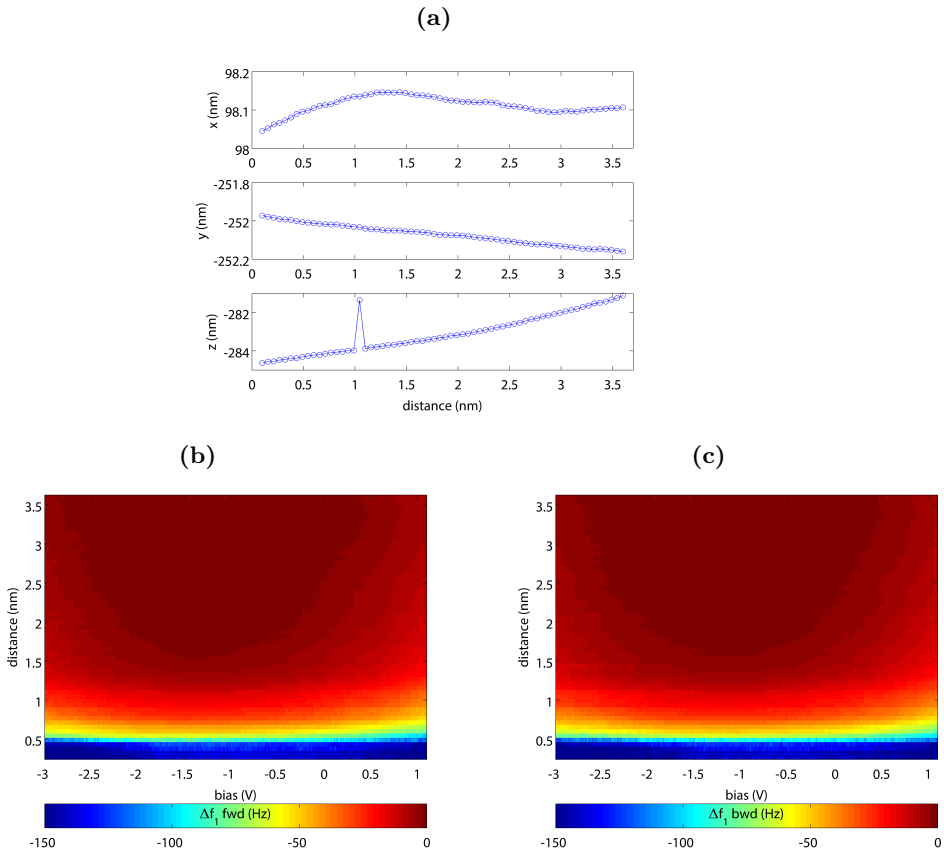

Figure 7.15: Frequency shift response for a hill site on $Gr/Cu(111)$. Raw data of forward swept curves (from positive to negative voltages) in a). Time averaged deflection along the CPD b). Data shifted by time averaged deflection. Points taken from interpolation with one addtional point inbetween the data points. Comparison of raw data (red dots) and data connected to a long range curve calculated from the fitting results along both directions d). setpoit -50 Hz f0: 170.775 kHz, A: 8 nm, k 30.13N/m, Q 30855, A2: 150 pm, Q2: 139488, add line for clarity of star curves

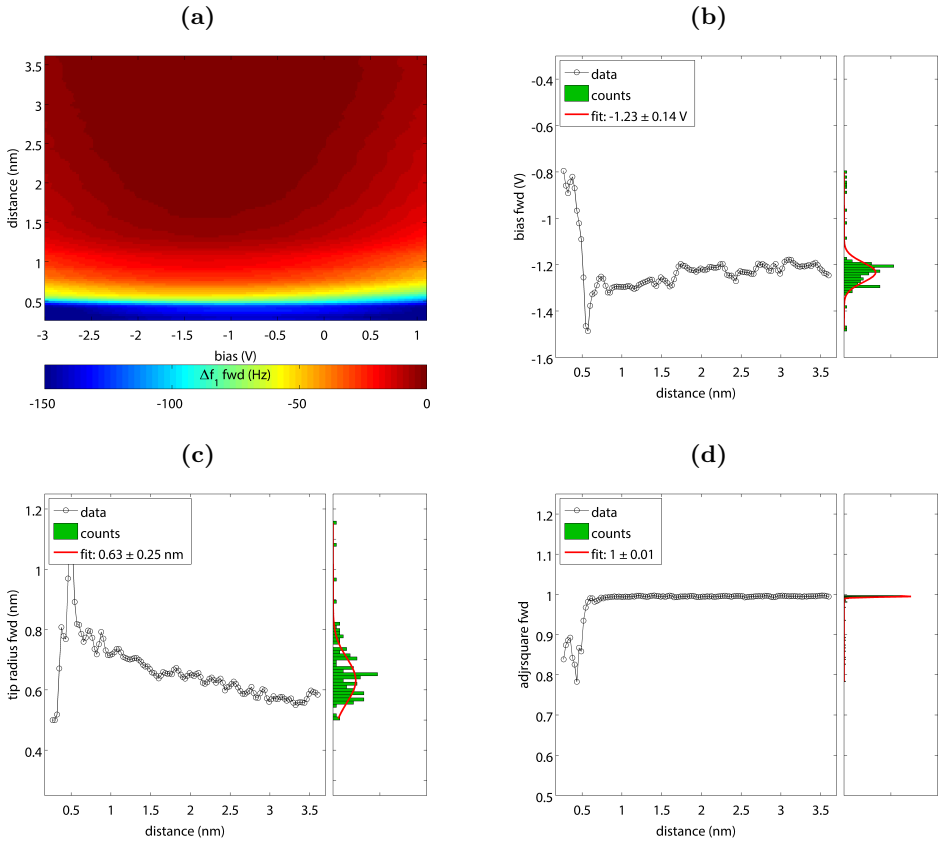

Figure 7.16: Frequency shift response for a hill site on $Gr/Cu(111)$ fitted line wise for the electrostatic interaction along the bias axis . Map reconstructed from the fit results in a). Change in bias along the compensated electrostatic force b). Tip radius obtained by the fit model c). Goodness of fit represented by the adjusted root square d).

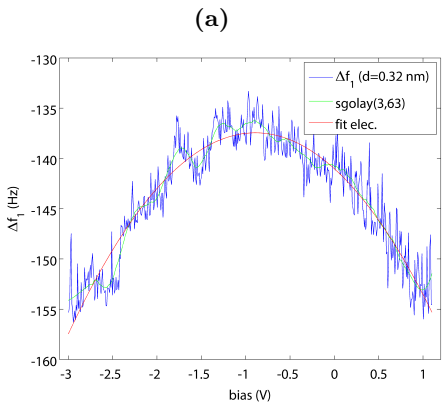

Figure 7.17: Response of amplitude on $Gr/Cu(111)$.

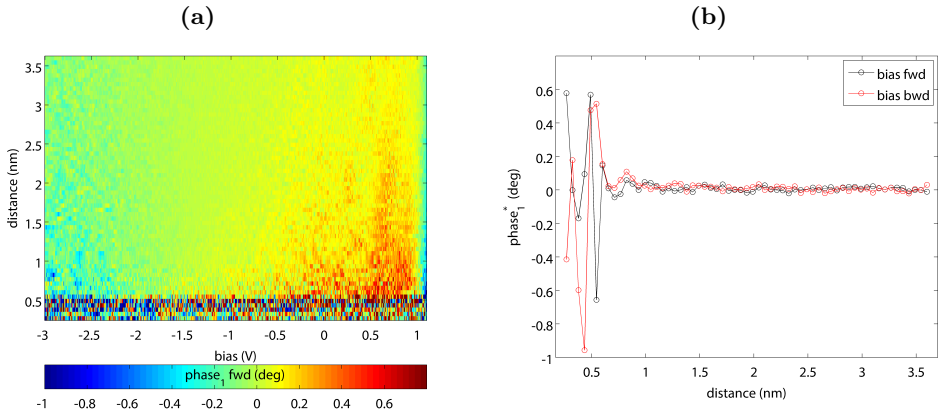

Figure 7.18: Response of phase on $Gr/Cu(111)$.

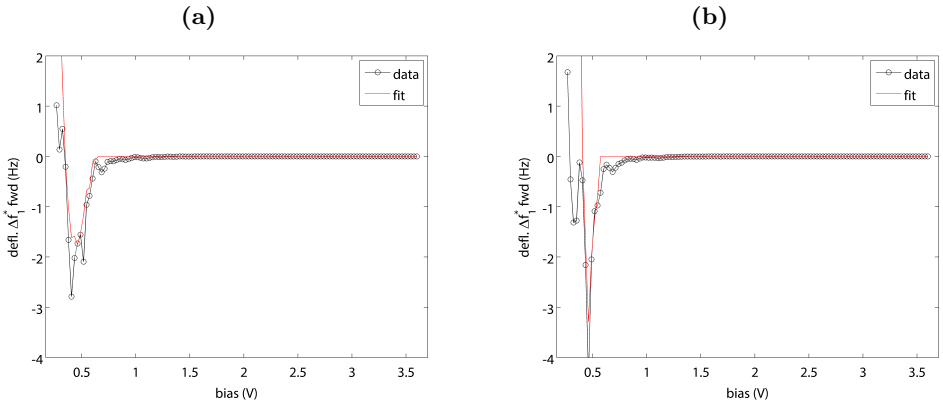

Figure 7.19: Frequency shift by time averaged deflection Gr/KBr/Cu. Hill a), valley b)